ABSTRACT

Title of dissertation: CHARACTERIZING UNUSUAL BEHAVIOR IN PRISTINE TOPOLOGICAL INSULATOR Bi_2Se_3

Paul Syers, Doctor of Philosophy, 2015

Dissertation directed by: Professor Johnpierre Paglione
Department of Physics

Bismuth Selenide is a material of great interest to physicists as it is one of the first materials proven to be a strong topological insulator (TI). Despite its promise as an ideal TI, defects in the material that have proven difficult to elminate, keep the material's conductive states at its surface hidden by metallic behavior in the bulk. The work discussed in this thesis focuses primarily on techniques aimed at improving the material quality of pure Bi_2Se_3 and better understanding the effects of air exposure on both the surface and bulk of the material. The goal is to reliably produce samples in which signatures of the surface states can be seen in simple, bulk measurements. Changes in sample quality were achieved through the manipulation parameters such as Se flux and environmental pressure during the growth process. Through these techniques, the intrinsic carrier concentration of Bi_2Se_3 samples was lowered to the lowest levels ever reported. Samples showing nonmetallic behavior were also produced and investigated. Furthermore, it was discovered that samples of Bi_2Se_3 with low carrier concentrations showed strong linear magnetoresistance.

The nature of this linear magnetoresistance, its angular dependence, and its evolution over time were also investigated. This thesis will discuss the results of these experiments as examples of how growth techniques influence sample quality, which in turn affects the properties of Bi_2Se_3.

CHARACTERIZING UNUSUAL BEHAVIOR IN PRISTINE TOPOLOGICAL INSULATOR Bi_2Se_3

by

Paul James Howard Syers

Dissertation submitted to the Faculty of the Graduate School of the
University of Maryland, College Park in partial fulfillment
of the requirements for the degree of
Doctor of Philosophy
2015

Advisory Committee:
Professor Johnpierre Paglione, Chair
Professor Ichiro Takeuchi
Professor Nicholas P. Butch
Professor Richard Greene
Professor James Williams

Foreword

The results of my work have contributed to the following published works, with the publications that have portions represented in this thesis notified with an asterisk:

∗P. Syers and J. Paglione, "Investigation of Anisotropic Linear Magnetoresistance in pure Bi_2Se_3," *pre-print*.

∗P. Syers and J. Paglione, "Toward Insulating Behavior in Pure Bi_2Se_3," *pre-print*.

∗P. Syers, D. Kim, M.S. Fuhrer, and J. Paglione, "Tuning bulk and surface conduction in topological Kondo insulator SmB_6," *submitted to Phys. Rev. Lett.*.

N. P. Butch, K. Kirshenbaum, P. Syers, A. B. Sushkov, G. S. Jenkins, H. D. Drew, and J. Paglione, "Strong surface scattering in ultrahigh-mobility Bi_2Se_3 topological insulator crystal," *Physical Review B* **81**, 241301(R) (2010).

N. P. Butch, P. Syers, K. Kirshenbaum, A. P. Hope, and J. Paglione, "Superconductivity in the topological semimetal YPtBi," *Physical Review B* **84**, 220504(R) (2011).

S. Cho, D. Kim, P. Syers, N. P. Butch, J. Paglione, and M. S. Fuhrer, "Topological Insulator Quantum Dot with Tunable Barriers," *ACS Nano Letters* **12**, 469–472 (2012).

M. T. Edmonds, J. T. Hellerstedt, A. Tadich, A. Schenk, K. M. O'Donnell, J. Tosado, N. P. Butch, P. Syers, J. Paglione, and M. S. Fuhrer, "Air-Stable Electron Depletion of Bi_2Se_3 Using Molybdenum Trioxide into the Topological Regime," *ACS Nano* **8**, 6400–6406 (2014).

M. T. Edmonds, J. T. Hellerstedt, A. Tadich, A. Schenk, K. M. O'Donnell, J. Tosado, N. P. Butch, P. Syers, J. Paglione, and M. S. Fuhrer, "Stability and Surface Reconstruction of Topological Insulator Bi_2Se_3 on Exposure to Atmosphere," *Journal of Physical Chemistry C* **118**, 20413–20419 (2014).

B. Fauqué, N. P. Butch, P. Syers, J. Paglione, S. Wiedmann, A. Collaudin, B. Grena, U. Zeitler, and K. Behnia, "Magnetothermoelectric properties of Bi_2Se_3," *Physical Review B 87*, 035133 (2013).

J. J. Hamlin, J. R. Jeffries, N. P. Butch, P. Syers, D. A. Zocco, S. T. Weir, Y. K. Vohra, J. Paglione, and M. B. Maple, "High pressure transport properties of the topological insulator Bi_2Se_3 ," arXiv: 1111.0098.

G. S. Jenkins, A. B. Sushkov, D. C. Schmadel, N. P. Butch, P. Syers, J. Paglione, and H. D. Drew, "Terahertz Kerr and reflectivity measurements on the topological insulator Bi_2Se_3," *Physical Review B* **82**, 125120 (2010).

D. Kim, P. Syers, N. P. Butch, J. Paglione, and M. S. Fuhrer, "Coherent topological transport on the surface of Bi_2Se_3," *Nature Communications* **4**, 2040 (2013).

D. Kim, S. Cho, N. P. Butch, P. Syers, K. Kirshenbaum, S. Adam, J. Paglione, and M. S. Fuhrer, "Surface conduction of topological Dirac electrons in bulk insulating Bi_2Se_3," *Nature Physics* **8**, 459–463 (2012).

D. Kim, Q. Li, P. Syers, N. P. Butch, J. Paglione, S. Das Sarma, and M. Fuhrer, "Intrinsic Electron-Phonon Resistivity of Bi_2Se_3 in the Topological Regime," *Physical Review Letters* **109**, 166801 (2012).

K. Kirshenbaum, P. Syers, A. P. Hope, N. P. Butch, J. R. Jeffries, S. T. Weir, J. J. Hamlin, M. B. Maple, Y. K. Vohra, and J. Paglione, "Pressure-Induced Unconventional Superconducting Phase in the Topological Insulator Bi_2Se_3," *Physical Review Letters* **111**, 087001 (2013).

N. Kumar, B. A. Ruzicka, N. P. Butch, P. Syers, K. Kirshenbaum, J. Paglione, and H. Zhao, "Spatially resolved femtosecond pump-probe study of topological insulator Bi_2Se_3," *Physical Review B* **83**, 235306 (2011).

X. Zhang, N. P. Butch, P. Syers, S. Ziemak, R. L. Greene, and J. Paglione, "Hybridization, Inter-Ion Correlation, and Surface States in the Kondo Insulator SmB_6," *Physical Review X* **3**, 011011 (2013).

Z.-H. Zhu, G. Levy, B. Ludbrook, C. N. Veenstra, J. A. Rosen, R. Comin, D. Wong, P. Dosanjh, A. Ubaldini, P. Syers, N. P. Butch, J. Paglione, I. S. Elfimov, and A. Damascelli, "Rashba Spin-Splitting Control at the Surface of the Topological Insulator Bi_2Se_3," *Physical Review Letters* **107**, 186405 (2011).

Z.-H. Zhu, C. N. Veenstra, G. Levy, A. Ubaldini, P. Syers, N. P. Butch, J. Paglione, M. W. Haverkort, I. S. Elfimov, and A. Damascelli, "Layer-By-Layer Entangled Spin-Orbital Texture of the Topological Surface State in Bi_2Se_3," *Physical Review Letters* **110**, 216401 (2013).

Z.-H. Zhu, A. Nicolaou, G. Levy, N. P. Butch, P. Syers, X. F. Wang, J. Paglione, G. A. Sawatzky, I. S. Elfimov, and A. Damascelli, "Polarity-Driven Surface Metallicity in SmB_6," *Physical Review Letters* **111**, 216402 (2013).

Dedication

To my father: you may not be here at the finish line, but I couldn't have gotten here without the greatest dad a kid could want to have.

Acknowledgments

Science is inherently a collaborative process, with every advancement owing its success at least in part to the collective progress that has proceeded it. In addition, over the past 100 years and more, scientists have increasingly worked together, leaving behind the days of the privileged few working for years in solitude. This trend is for the benefit of both science as a field and those working in it. To that end, the work in this thesis, as well as other work I have accomplished over the past five years, would not have been possible without the help of many others. I would like to take this opportunity to acknowledge those who have helped me, for which I am extremely grateful.

First and foremost I'd like to thank my advisor, Professor Johnpierre Paglione for introducing me to the interesting field of Topological Insulators, for being a supportive, responsive, and all around excellent advisor. There has never been an occasion when I've knocked on his door and he hasn't given me time. I would also like to thank him for taking me on as a researcher, helping me during my transition from my masters to my doctoral studies, and for his recent career advice and support. He has always been a wealth of information and has encouraged me to follow my research interests, which led to many fruitful and enjoyable travel research projects.

Speaking of travel research projects, I would like to acknowledge the help of my collaborators on those projects: Cyril Proust, Baptiste Vignolle, and Wojciech Tabis at LNCMI-Toulouse, as well as Michael Sutherland, Swee Goh, and Sven Friedemann of the Quantum Matter group at the University of Cambridge. They

all not only were great to work with, but also went above and beyond, helping me with travel and accommodation arrangements for my trips. I am grateful to other collaborators for their work; in particular I would like to acknowledge Dohun Kim, Michael Fuhrer, Dennis Drew, Greg Jenkins, and Jason Jeffries for their excellent work and helpful discussions.

I would also like to thank all of the members of my group, along side whom I worked over these years, including: Kevin Kirshenbaum, Rongwei Hu, Rich Suchoski, Tyler Drye, Steve Ziemak, Connor Roncaioli, Chris Eckberg, Renxiong Wang, Xiaohang Zhang, Shanta Saha, Yasuyuki Nakajima, Xiangfeng Wang, Kefeng Wang, and Jie Yong.

I would especially like to thank Nicholas Butch for teaching so much during my first year of research here, as well as his continued guidance, collaboration, and most recently, service on my thesis committee. Without his help, most of this work would not have been possible. Thanks are also due to Rick Greene, James Williams, and Ichiro Takeuchi for serving on my thesis committee.

I would also like to acknowledge help and support from the staff members in the department as well as at the Maryland Nanocenter Fablab, who have kept things running smoothly and helped me troubleshoot things when they weren't.

Finally I would like to thank my friends and family, who have helped me through the difficult times and shared with me the good times, especially John Thornton — for his mathematical contributions on top of his dear friendship – my mother, and my sister. It is too easy to forget that without enjoying life as a whole, we cannot enjoy our work and everything suffers as a consequence. The support

and guidance of friends and family in one's overall health and their affect on the person's identity is so often under-acknowledged or overlooked.

It is impossible to remember all to whom I owe my gratitude, and I apologize to those I've inadvertently left out.

Table of Contents

List of Tables

List of Figures

List of Abbreviations

CNAM	Center for Nanophysics and Advanced Materials
EDS	Energy dispersive x-ray spectroscopy (also called EDX)
LL	Landau Level
QO	Quantum Oscillations
SdH	Shubnikov de Haas
SOC	Spin Orbit Coupling
SS	Surface States
QWS	Quantum Well States
TI	Topological Insulator

Chapter 1: Introduction

In recent years, the field of Topological Insulator research has exploded on the condensed matter community. In 2011 alone, over 450 articles were published with "Topological Insulator" as a keyword. The topic is a rare combination of theoretical puzzle, and experimental playground. Bismuth Selenide is one of the first materials proven to be a strong topological insulator (TI). Despite the wealth of knowledge about it that already exists, it has continued to offer new experimental results that have greatly advanced our understanding of TIs. Despite what has been learned from working with Bi_2Se_3, it has proven to be far from the ideal TI for technological application. Current standard methods of producing the material do not eliminate the formation of defects in Bi_2Se_3, which cause the bulk of the material to become conductive and dwarf the behavior of the topologically nontrivial surface states. This chapter will provide necessary background information on both the field of TIs in general — its conceptual origins as well as recent notable recent experimental results — and the material Bi_2Se_3 specifically.

1.1 Topological Insulators

Despite being a relatively young field, research on TIs, both theoretical and experimental, has uncovered so much that it would be impossible to give an overview of the entire field at this point. This section will give a basic introduction to the conceptual basis of the class of materials, as well as some background details that are relevant to the measurements discussed in this work. References are provided, where possible, to give the reader the ability to find more information on details not covered at length here.

1.1.1 Theoretical Details

A common guiding perspective in the field of Condensed Matter is the concept of symmetry. Many seemingly disparate phenomena have been shown to follow universal behavior, which, it turns out, is guided by the preservation or breaking of a symmetry of some kind. The concept of unit cells within crystal structures comes from the sectioning of translational symmetry [1]. The various types of crystal structures are further distinguished, among other ways, by how they break rotational symmetry [2]. The phenomenon of superconductivity is now seen to break a gauge symmetry [3]. Furthermore, the breaking of inversion, and other symmetries also cause other unusual phenomenae [4]. In addition to physical processes arising from the breaking of symmetries, other properties of materials can be better characterized

by how they change when various symmetries are broken[1] [2].

Then an effect was discovered in high quality materials at high magnetic fields that caused the transverse magnetoresistance (ρ_{xy}) to take on precise values over large ranges of magnetic fields, with these precise values being independent of the specific material details[5]. Investigations into the Quantum Hall Effect revealed that the phenomenon was guided not only by symmetries, but also by a different quality of the electromagnetic environment within the material [6, 7]. This other defining characteristic of the system is defined as a type of topology. Topology is a fundamental characteristic of objects and spaces[3] resulting from global characteristics. This means that the topology of an object or space is robust against local perturbations that change the environment in a continuous manner.

The most basic (and commonly used) example of topologically different objects is the comparison of a sphere and a torus (see Fig. 1.1). The topological characteristic of these two objects is the number of holes each has: the sphere having no holes and the torus one. These characteristics are quantized in nature, as in neither object can have half, or one quarter of a hole. Continuous transformations of the sphere can flatten it to a pancake, or stretch it into a filament, but it does not change the topology of the object and so it still remains different from the torus. The only way to make the sphere into a torus, would be to either puncture a hole in it, or join two

[1]

[2]For example, a nonzero external magnetic field breaks multiple symmetries along its axis, which can lift degeneracies in energy levels/bands. The same can happen with an electric or thermal current. Any anisotropies or hysteresis measured with regards to these variables indicates a nontrivial relationship to the symmetries broken.

[3]Here objects and spaces are treated in a broader, more abstract sense. The concept of topology is not limited to physical space, but also applies to momentum space, Hilbert spaces, etc.

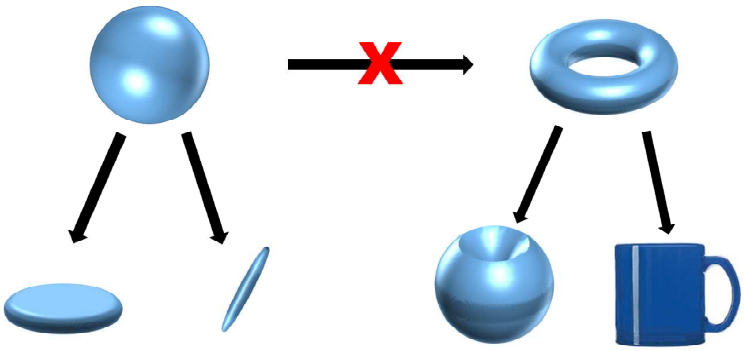

Figure 1.1: A sphere and torus illustrating topological classification. One way to differentiate the two objects is by the number of holes, which is a topological classification. No matter how you continuously deform either object, one will still have a single hole, and the other no holes.

ends of the transformed sphere together, thus creating a hole through "wrapping around". This puncturing or melding is a discontinuous transformation, and one can identify a boundary between when the object had no holes and one hole. Such a discontinuous changing of topology and the boundary between them that is the origin of the physical phenomae that are of such great interest in the field.

In condensed matter physics, Haldane first came up with a model combining the preservation of certain symmetries with topology to predict a system which produced the before seen quantized Hall values without the presence of a strong external magnetic field [8]. This technique was later used to explain the Quantum Spin Hall effect [6, 7, 9] and investigated further by Kane, Fu, Mele, and others [10–13] to predict a range of distinct topologica classes arising from different combinations of topologies and preserved symmetries.

For the topological class of 3D materials that initially caught the interest

of the field, Kane and Mele determined a topological order parameter of the Z_2 classification, calculated in the following way.

$$I = \frac{1}{2\pi i} \oint_C d\mathbf{k} \cdot \nabla_{\mathbf{k}} log[P(\mathbf{k}) + i\delta] \tag{1.1}$$

This closed path integral occurs over half the Brillouin zone of the material and sums up the winding of the phase of the Pfaffian[4] along the path. In this formulation, the Pfaffian depends on the Berry's phase space curvature. Since the integral essentially tracks the overall curvature of the Berry's phase space, it is inherently tracks its topology, which changes discontinuously, thus allowing it to be used as a measure of topological characterization. The result of the integral reflects the material's Chern class and so I is called the Chern number.

What determines the evolution of $P(\mathbf{k})$ within the brillouin zone is related to the material's band structure and a change in Chern number occurs with a phenomenon called band inversion [14] brought on by the effects of Spin Orbit Coupling (SOC).

In typical band structures, an example of which is shown in Fig. 1.2, the bonds formed by higher electron orbitals produce higher energy bands. However, as the field of semiconductor research has made abundently clear, the energy gaps between the lower energy bands and higher energy bands can be quite small, or even zero. More simplistic band structure calculations usually only deal with the most basic interactions resulting from the nature of chemical bonds and specific crystal structure

[4]Defined as $P(\mathbf{k})$ =Pf$[\langle u_i(\mathbf{k})|\Theta|u_j(\mathbf{k})\rangle]$ where Θ is a time reversal symmetry preserving matrix that links opposite momentum pairs in the following way $|u_i(-\mathbf{k})\rangle = \Theta|u_i(\mathbf{k})\rangle$ [10]

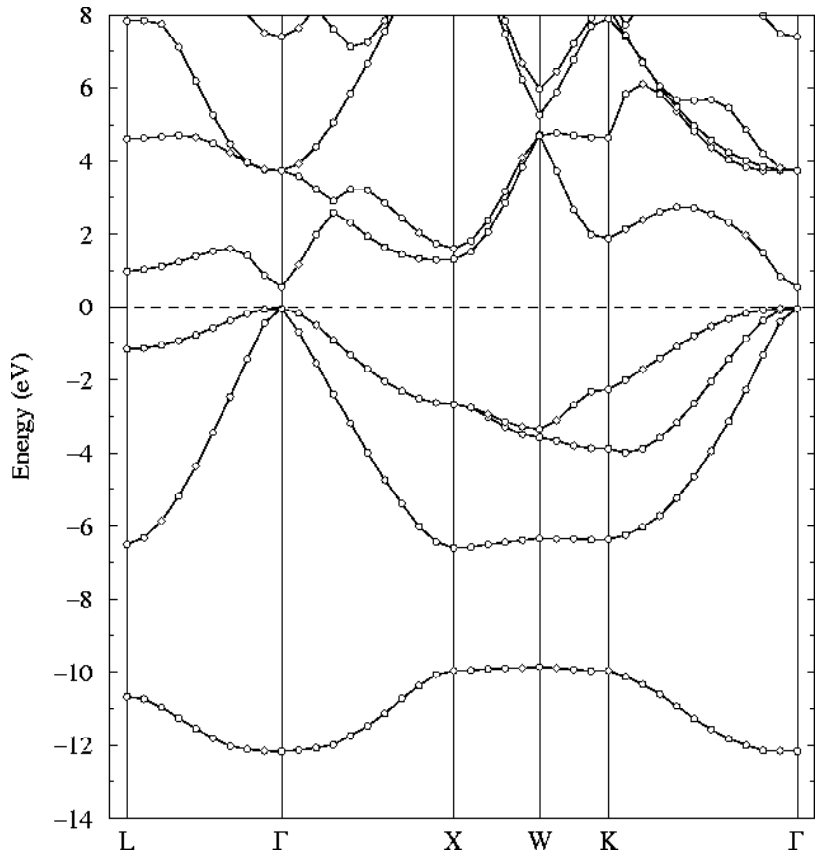

Figure 1.2: An example band structure calculated using a form of density functional theory and example parameters. In the center of the band structure, a region of energy can be seen where there is no available energy state. This is the energy band gap. The band at energies above this gap is known as the conduction band, and the band below this gap is the valence band. [15]

of the material. The higher order interaction of spin-orbit coupling is usually small enough to be insignificant, and often specific orbitals that preserve or break various symmetries (parity, time-reversal, etc.) are degenerate with others that don't. In the heavier elements, however, higher values of orbital angular momentum (l) can greatly increase the spin orbit coupling to where it significantly shifts the energy bands of some orbitals, but not others. Therefore, if a material exists with little to

no energy gap between two bands before spin orbit coupling taken into account, the addition of the spin orbit coupling interaction can pull one or more the higher energy band down in energy at certain points, while pushing the lower energy band(s) upwards at those points, causing a crossing of the two bands. A band crossing of specific natures defined by Fu, Kane, Mele, and others also results in a change in topology.

Band crossings in the bulk of materials are, however, nothing new in condensed matter physics. At the specific energy-momentum point where the bands would cross in the bulk, a wavefunction degeneracy would exist that is forbidden by the Pauli exclusion principle. Therefore the energy bands are restructured so that they do not actually cross, thus earning the name 'avoided crossing'[5]. This avoided crossing happens within all materials, regardless of their topological order, and the strength of the gap opened by the avoided crossing is influenced by such properties as crystal field strength and effective mass. However, when one crosses[6] from inside a material with inverted bands that have changed the topology of the material to an outside environment of trivial topology[7] the energy bands must revert back to their uninverted state. In these special symmetry preserving/breaking cases, such a boundary also involves two materials with different Chern numbers, and thus crossing from material to the other involves a change in topology. It is at this boundary, where the bands must cross and the topology must change, to switch between their inverted and uninverted states, and in crossing there must exist some

[5]The mathematics of how avoided crossings form is a part of perturbation theory.
[6]No pun intended.
[7]for example another material without inverted bands, or simply empty space

point where there is no energy gap between the two energy bands.

Part of the theory explaining the 2D TI case helps explain why the band inversion causes the creation of the boundary states. The theory of the 3D TI case is similar, so the general concepts carry over. The Hamiltonian, developed by Bernevig, Hughes and Zhang [16], is described by the following equations

$$\mathcal{H} = \begin{pmatrix} h(\mathbf{k}) & 0 \\ 0 & h*(-\mathbf{k}) \end{pmatrix} \tag{1.2}$$

$$h(\mathbf{k}) = \epsilon(\mathbf{k})\mathbb{I}_{2\times 2} + d_a(\mathbf{k})\sigma^a \tag{1.3}$$

with $\mathbb{I}_{2\times 2}$ being the 2×2 identity matrix, σ^a being a pauli spin matrix, and

$$\epsilon(\mathbf{k}) = C - D(k_x^2 + k_y^2), \quad d_a(\mathbf{k}) = [Ak_{x'} - Ak_{y'}M(\mathbf{k})], \quad M(\mathbf{k}) = M - B(k_x^2 + k_y^2) \tag{1.4}$$

where d_a is the thickness and A, B, C, D, and M are material parameters that depend on the overall geomtry of the 2D TI

With no external field, the bulk energy spectrum is given by the following equations

$$E_\pm = \epsilon(k) \pm \sqrt{d_a d_a} \tag{1.5}$$

$$= \epsilon(k) \pm \sqrt{A^2(k_x^2 + k_y^2) + M^2} \tag{1.6}$$

and the model reduces to two copies of the well known 2D[8] massive Dirac Hamil-

[8]Technically it's (2+1) dimensions

tonian, one for each spin state. For this equation, M corresponds to the energy difference between the electron and hole bands closest to E_F at the Γ point in the Brillouin zone. With an inverted band structure, M becomes negative. This might immediately seem impossible, but since the system is not relativistic none of the related effects apply, and furthermore the massive Dirac model does not distinguish between positive and negative mass, except in one crucial sense. In order for M to go from negative to positive, it must cross zero, or in other words, it must cross through an environment where the two solutions to Eq. 1.5 have zero mass. Remembering that the size and sign of M is determined by the size of the energy gap between E_1 and H_1, which is in turn determined by the material parameters, which in the 3D TI case includes SOC strength. Thus at some point, moving along a path from inside a TI, where the energy gap $E_1 - H_1$ is negative, to outside the TI, where the energy gap is positive, the energy gap must be zero, and therefore Eq. 1.5 must have two massless solutions.

To preserve the required symmetries, this change to/from band inversion occurs at a high symmetry point within the Brilloun zone. The result, shown in Fig. 1.3, describes a double cone in k-space. Similarly, the enforced chirality of the edge states resulting from the theory in the 2D case becomes a spin-locking effect on the states that make up what is named the Dirac cone. Normally, the Pauli-Exclusion principle would force an avoided crossing at the point where the two cones meet, however, Kramer's theorem[9] allows the crossing to exist in the absence

[9]Kramer's theorem posits that all eigenvalues of a Hamiltonian that protects time reversal symmetry must be doubly degenerate

of a magnetic field[10].

Another simple expression of the theory can also show that the states originating from the topological boundaries are also confined to those boundaries. Examining a 1D boundary between at TI (effective mass < 0) and a normal material (effective mass > 0) the eigenvalues of the 1D Dirac equation must satisfy the relationship

$$\begin{bmatrix} m(x)v^2 & -iv\hbar\partial x & \\ -iv\hbar & \partial x & -m(x)v^2 \end{bmatrix} \begin{pmatrix} \phi_1(x) \\ \phi_2(x) \end{pmatrix} = E \begin{pmatrix} \phi_1(x) \\ \phi_2(x) \end{pmatrix} \tag{1.7}$$

The eigenvalues must be solved for each side (m$<$ 0 and m$>$ 0) separately and in a way that the full solution is continuous at the boundary ($x = 0$). The wave function must vanish at $\pm\infty$ and so an exponential function would suit that requirement. The resulting secular equation to be solved for the exponent λ is then

$$\det \begin{bmatrix} m_{+,-}v^2 - E & iv\hbar\lambda_{+,-} \\ iv\hbar\lambda_{+,-}m_{+,-}v^2 - E & \end{bmatrix} = 0 \tag{1.8}$$

which gives the solution

$$\lambda = \pm\frac{\sqrt{m_{+,-}^2 v^4 - E^2}}{v\hbar} \tag{1.9}$$

assuming λ is real and therefore decaying away from the boundary. The resulting wavefuctions then have the relationships

$$\phi_1^{+,-} = -\frac{iv\hbar\lambda_{+,-}}{m_{+,-}v^2 - E}\phi_2^{+,-} \tag{1.10}$$

[10]A significant magnetic field would break time reversal symmetry of the surface environment, and therefore cause the opening of a gap.

and in order to enforce continuity

$$\frac{-\sqrt{M_+^2 v^4 - E^2}}{m_+ v^2 - E} = \frac{\sqrt{M_-^2 v^4 - E^2}}{-m_- v^2 - E} \tag{1.11}$$

which only has a valid solution if $E = 0$. Therefore the theory not only shows that the states at the surface of a TI are localized to the boundary, decaying exponentially away from it, but also that there must be a zero energy state exactly at the surface, i.e. the Dirac point previously mentioned.

Since these two gapless states arise from the change in topology, no local, nonmagnetic perturbations, like impurities and other typical structural defects, can destroy it. If the density of surface defects in a region becomes high enough to locally undo the band inversion, then that region will then behave as if it is "outside" the material, and so the surface that is the topological boundary will curve around that locally disturbed region. It is this quality of the surface states that gives them the common description of being topologically protected [5].

The spin-locking of the surface states means that the spin-state of an electron occupying a state is tied to the momentum direction of that state, therefore in order to change its momentum the electron must correspondingly change its spin state. This has a very useful effect when considering scattering of conducting states off of nonmagnetic impurities[11]. Normally when an electron encounters an impurity in its path, it scatters, changing its momentum in the process. With the spin-locked surface states, however, the electron requires more energy for the electron

[11] As mentioned before, magnetism destroys the time reversal symmetry, and thus a magnetic impurity can locally gap the surface states.

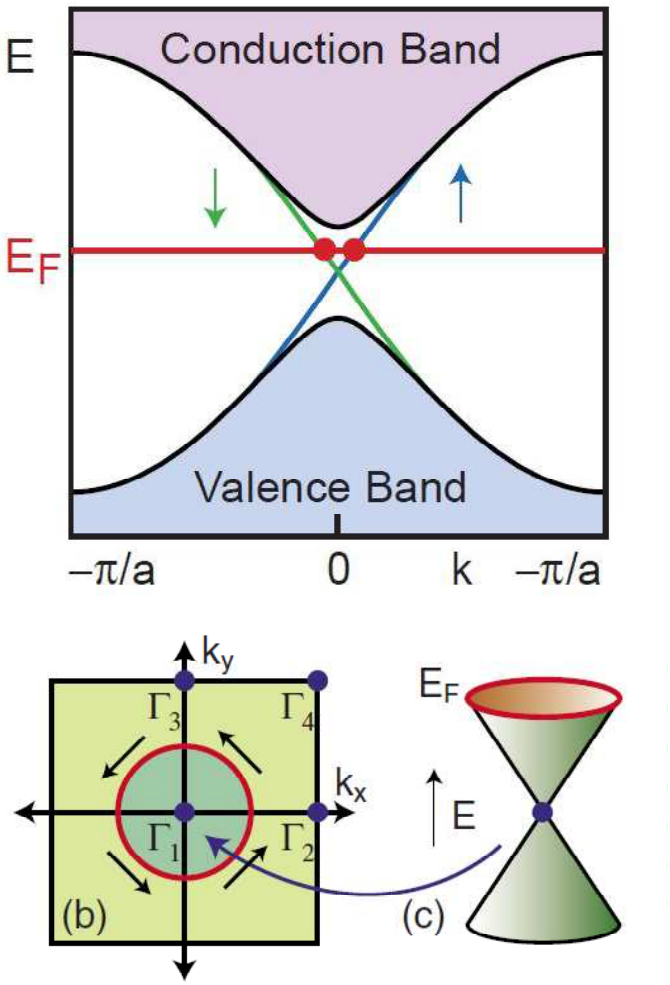

Figure 1.3: A diagram showing the expected form of a Dirac cone. The top diagram shows the basic band gap (illustrated in detail in the previous figure) with the two red lines illustrating the energy states crossing the gap at the surface. The lower two figures show how the Dirac cone takes a conical shape in momentum space, with the spin state changing (in this illustration counterclockwise) as the momentum state traverses the brillouin zone. [14]

to scatter, because in changing its momentum, the electron must also change its spin state, and the larger the momentum change, the larger the spin change. In the example of complete backscattering, a full momentum reversal for the electron would require a spin flip. This not only requires the most energy of the possible momentum changes, but given the absence of magnetism in the interaction, it makes a spin flip even less likely. This essentially means that backscattering is forbidden in the surface states. The net effect is that the momentum states are "protected" against nonmagnetic impurities, due to the spin-locking.

As seen in Fig. 1.3 the Dirac cone takes the form of two cones, connected at their vertices. Since the effective mass of the conductive states in a material is related to the curvature of the energy bands of which the states are a part, the linear nature of the conductive states at the surface means that they have no curvature and therefore behave as massless particles. In addition to reflecting the effective mass, the dispersion relation of an energy band also shows the sign of charge carrier through the sign of its first derivative. Upward sloping energy bands behave like negative charge carriers, and downward sloping bands like positive ones. Therefore the top half of the Dirac cone is electron-like and the bottom half hole-like. However, the doubly degenerate energy state that exists at the vertex of the two cones, known as the Dirac point can be neither fully electron-like, nor fully hole-like. Additionally, the Dirac point also exists at a point with zero momentum. With a zero effective mass, zero momentum, and no concrete charge sign, the two energy states at the Dirac point behave as Majorana fermions[12].

[12]The body of literature describing Majorana fermions is extensive, and more about them will

So far, the theory has dealt with describing the origin and properties of the topologically protected surface states. While all of this is true for all boundaries between materials of different topologies, it would be difficult to see and of little use in the case of surfaces between two metals of different topology, because any electrical conduction along the topological boundary surface could easily scatter into the bulk states and would furthermore be dwarfed by the electrical conduction through the bulk of the material(s) on either side. Therefore, an insulator with nontrivial topology is needed, in order to detect the surface states. A TI is a material that has not only a nontrivial topological order, but also a Fermi energy that falls within an energy gap, making it insulating in the bulk. This way, the topologically protected Dirac cone of spin-locked energy states that exists at the boundary of the material cannot be avoided or by conduction elsewhere in the material.

Furthermore, the spin-locking of the Dirac cone states only provides topological protection if the number of those cones that cross the Fermi energy in the Brillouin zone is odd. Band inversion is not an effect that occupies the entire Brillouin zone, and therefore it is possible that it can occur at multiple locations in the Brillouin zone. If an even number of Dirac cones exist in the Brillouin zone, then it becomes possible for an electron occupying an energy state on one Dirac cone to change its momentum to the other Dirac cone without flipping its spin. The result is that the two Dirac cones each end up cancelling each other out and producing a conductive environment with the typical spin degeneracy in all directions. Only a material with an odd number of band inversion points will preserve all the unique conductive

be discussed later in this work.

properties produced by the topological boundary.

This section has discussed defining a topological characteristic of materials and the direct consequences of moving across a boundary between materials with different topologies. When these boundary states are combined with other nonlocal quantum mechanical phenomena, the interactions can destroy the states, such as with magnetism, or they can lead to further unusual behavior. The next section will discuss one such interaction that is of great interest to researchers.

1.1.2 Majorana States

The type of energy gap considered in the previous sections has been an intrinsic gap, arising out of the lower order interactions between lattice atoms within the material. Strong correlations within materials can, in certain environments cause the opening of an energy gap at lower temperatures. The onset of superconductivity in a material, for example creates a relatively small energy gap around E_f[13]. If superconductivity were to occur in a TI, the question arises as to whether or not this gap would also open up in the topologically protected surface states, and if so, how that would occur. Liang Fu and others [5, 14, 17] investigated this and determined that the onset of s-wave superconductivity would indeed open up an energy gap at the surface of a TI. However, the chiral nature of the Dirac states would cause the superconductivity to be of $p_x + ip_y$ type at the surface [17].

Furthermore, the attractive potential that causes superconductivity occurs be-

[13]This energy gap is due to the paired electrons condensing down to a collective lowest energy state, and therefore leaving their energy states at E_f.

tween pairs of electrons with opposite momenta [3]. The geometry of the Dirac cones at the surface of a TI fit this requirement everywhere except for at the Dirac point. This so-called zero energy state cannot be moved away from its zero momentum position, and therefore remains at the center of the superconducting energy gap [17]. Therefore, just as how the topologically protected surface states would be nigh impossible to detect if there weren't an energy gap in the bulk of the material, the Majorana modes at the Dirac are equally undetectable unless the Dirac cone is similarly split by an energy-gap, and superconductivity provides a mechanism for doing that.

Majorana Fermions exhibit exotic properties, and therefore the Majorana quasiparticles at the Dirac point are expected to mimic these properties. Having an effective mass of zero, and no concrete charge value, the Majorana modes are part-electron, part-hole, entangled states called anyons with zero momentum. Due to the nature of their entanglement, the Majorana quasiparticles obey non-abelian statistics [18], meaning that their wave-functions are determined not only by their current interactions with each other, but also by their past interactions, a mathematical phenomenon called braiding.

The theory of TIs, their origin as well as their defining characteristics is rich and connected to many ideas in physics, both old and new. They provide a new area for theorists to explore, adding a new guiding principle of topology to the picture. What has caused research in topological insulators to grow so rapidly in recent years, becoming a subfield in its own right, has not been solely because of advancements in theory. Recent successes in experimental efforts have confirmed

the existence of these surface states in multiple materials, and rapid progress is being made in characterizing the surface states. With the theoretical concepts and predictions explained, the next section focuses on experimental progress in the field of topological insulators.

1.1.3 Experimental Progress

The experimental progress in the field of TIs has been rapid and varied. Since the first observation of spin-locked states at the surface of a bulk material, many other materials have been experimentally proven to be TIs. In addition to progress in the search for new TIs, the surface states of known TIs have been investigated in a number of different ways. This section is meant to provide a brief overview of the highlights of research in the field so far, as well as touch on specific experimental results relevant to this work.

The first experimental confirmation of the existence of SS in a TI was ARPES on Bi_xSb_{1-x}, where five topologically protected dirac cones were measured at the Fermi surface of the material [19]. This quickly led theorists to predict two similar systems (Bi_2Se_3 and Bi_2Te_3) as TIs [20, 21] and the same group that made the first groundbreaking TI discovery followed that with the confirmation of those predicted TI materials [22, 23]. While ARPES and other surface measurements could measure the topologically protected surface states, bulk measurements[14] were unsuccessful in resolving signatures of the surface states. This was because the two materials proved to be not truly insulating, with naturally occuring defects shifting the bulk

[14] Electrical and thermal transport, magnetoresistance, etc.

E_F out of the insulating gap — Bi_2Se_3 upwards into the conduction band and Bi_2Te_3 downwards into the valence band [24, 25].

To solve the problem of bulk conduction overwhelming the surface conduction in the two bismuth based TI crystals[15] two basic routes were followed: increase the fraction of surface conduction by decreasing sample thickness; or decrease the conduction in the bulk by making it actually insulating.

The first route to surface dominated transport, producing thinner samples, made rapid advancements. Due to the flake-like nature of Bi_2Se_3 and Bi_2Te_3, the famous scotch tape technique could be used to extract samples that were only a few nanometers thick. Gating studies showed the ability to tune E_f down into the bulk gap and all the way below the Dirac point, producing weak antilocalization [26, 27], quantum oscillations in gating [28, 29], and ambipolar transport [30]; examples of the latter two are shown in Fig. 1.5. Examples of the gating experiment results are shown in Fit. 1.5. Other traditional thin film growth techniques, such as reaction through chemical vapor deposition (CVD) [31], pulsed laser deposition (PLD) [32], and molecular beam epitaxy (MBE) [26, 33], were able produce high quality thin films of Bi_2Se_3 and Bi_2Te_3 over a range of nanoscale thicknesses. With these production techniques, precise thickness dependence measurements were also done, tracking the behavior of the surface states into a regime where coupling between two opposite surfaces of the film grew strong enough to destroy their spin-locking properties and restore normal insulating behavior in the film [26].

Successful attempts to achieve insulating behavior involved combating the

[15] In contrast to Bi_xSb_{1-x}, which is an alloy.

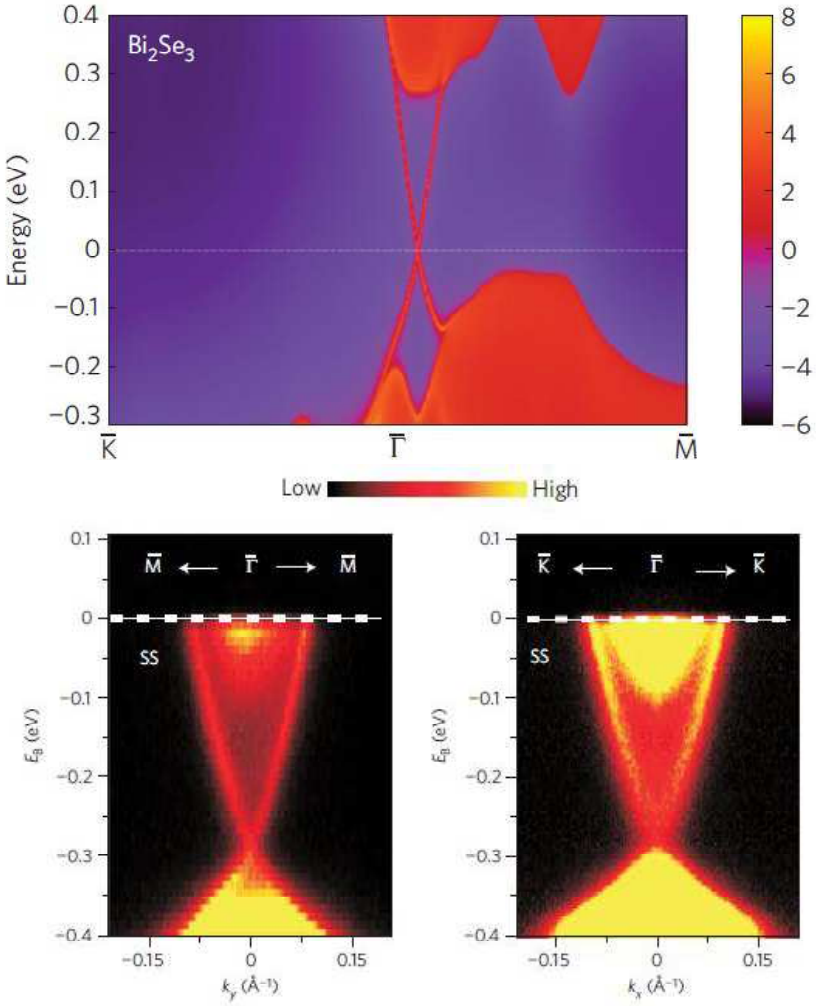

Figure 1.4: Graphs of both theoretical predictions [21] and experimental confirmation [22] of gapless conducting states at the surface of Bi_2Se_3, guaranteed by the material's topology.

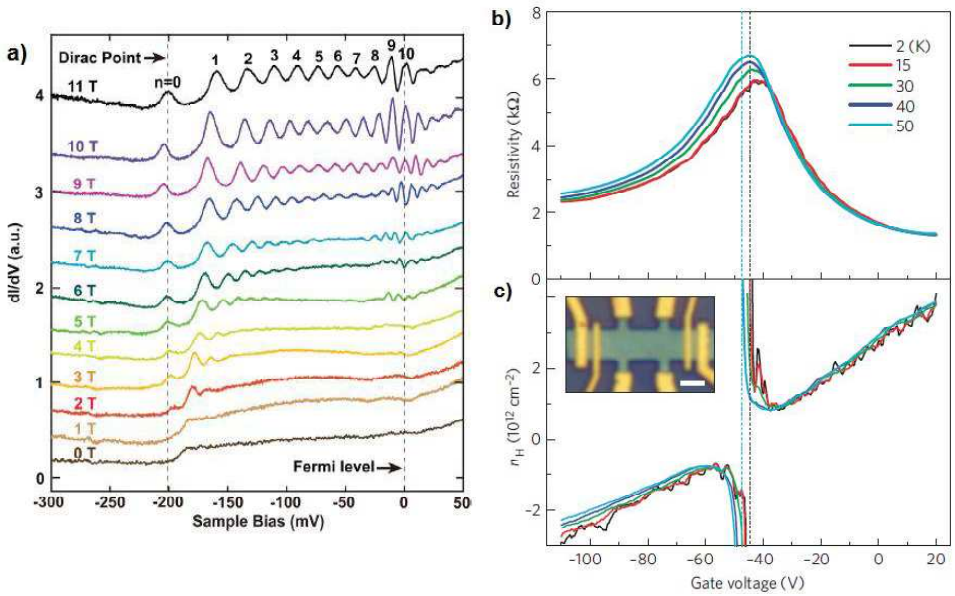

Figure 1.5: Data from gating experiments done on thin films of Bi_2Se_3. The left graph [28] shows quantum oscillations that emerge as gating voltage is increased in strength. The voltage brings E_F all the way through the lowest Landau level and past the Dirac point. The multiple curves show the oscillations increasing in amplitude, with increased magnetic field. The right graph [30] also shows gating effects that pull E_F through the Dirac point, as evidenced by the asymptote and sign change of n_H and the longitudinal resistance maximum.

naturally occuring doping by lowering the carrier concentration and mobility of the bulk through counterdoping and site substitution [23, 34–38]. These doped samples showed non-metallic temperature behavior. In some cases (one of which can be seen in Fig. 1.6) other effects such as weak-antilocalization [34, 39] and SdH oscillations of a 2D nature [40] were also measured. While these studies successfully achieved a reduction in the bulk concentration and mobility, they also had the unintended consequence of greatly reducing the mobility of the surface states, leaving the remaining conduction still dominated by the bulk.

Attempts were also made to achieve nonmetallic behavior without doping, for which there is precident in the literature. Those studies, while able to significantly lower the bulk carrier concentration without correspondingly lowering mobility, were unsuccessful in producing samples with non-metallic behavior [41]. This work is a continuation of those studies and will be discussed at length in a later section.

It was later discovered that surface dominated transport could be achieved in a ternary compound $Bi_2Te_{2-x}Se_x$ [42]. The secret to $Bi_2Te_{2-x}Se_x$'s success seems to be that the opposite doping effects of Te and Se in the compound mostly cancel each other out. Further tuning of E_f was shown to be possible in the material through Sb substitution for Bi [39]. However, even in this material, low surface state mobility continued to be an issue.

The efforts of researchers in Princeton of introducing Cu into Bi_2Se_3 in a certain manner different from doping unexpectedly produced samples with higher, not lower carrier concentrations — more surprisingly it produced superconductivity at 3.8K [43]. With the Princeton group's unconventional preparation technique, the Cu was not acting as a lower valency dopant, site substituting for Bi, but rather acting as an intercalant, occupying space between the material's quintuple layers, injecting extra electrons into the layers. The evidence in the first report of superconductivity in $Cu_xBi_2Se_3$ was very weak and the samples admittedly changed behavior over time, but a Japanese group followed up the work done in Princeton and found a more successful way to intercalate the Cu and produce more robust superconductivity [44, 45].

Superconductivity was also induced in the known topological insulators through

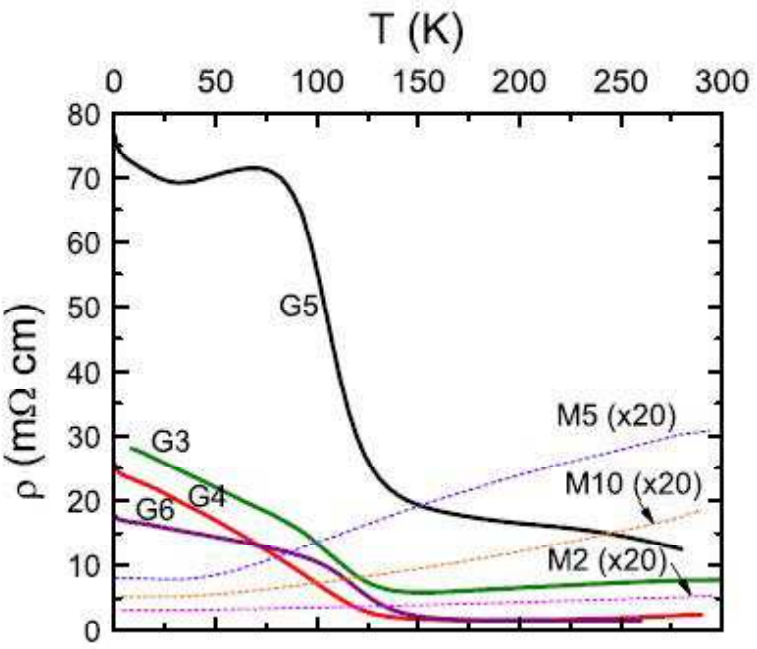

Figure 1.6: A plot of the temperature dependence of resistivity of $Ca_xBi_{2-x}Se_3$. Certain doping levels produce progressively less metallic samples, achieving up to a nearly 8-fold increase in resistivity [34].

increased pressure [46, 47]. Bi_2Se_3 undergoes a structural phase transition to a non-trivial material, however, at a pressure lower than the critical pressure for superconductivity, thus negating the chance topological superconductivity.

The studies of superconductivity naturally occuring in bulk samples, while very illuminating, did not lead directly to experiments searching for the predicted Majorana states, as one might expect. Work layering TI thin films with other superconducting materials proved to be the more successful route, in part because of the higher level of control over the thin film properties that had been shown [26]. The basic technique involves placing a TI thin film next to a superconductor and

using the proximity effect[16] to induce superconductivity in one surface of the TI. The presence of the locked in Majorana states in the center of the superconducting energy gap means that they are available states for outside electrons to tunnel into. Where a tunneling experiment in a normal superconductor would give no voltage response at zero bias voltage, a superconducting topological insulator should give a non-zero response at zero biase voltage. This so-called zero bias peak is considered a key signature of the majorana state and the zero bias peak was indeed measured by a group in the Netherlands [48] and is shown in Fig. 1.7.

Throughout the evolution of the field of TI research, ARPES experiments have proven the most useful in characterizing the topologically protected surface states. Spin resolved ARPES measurements that show the Dirac-like dispersion as well as chiral spin texture of surface states is considered to be ultimate proof that a material is topologically nontrivial. Because it is a surface based technique, ARPES does not require the E_F to sit in the bulk insulating gap to clearly measure the surface states.

For example, ARPES studies of the surface over time have also revealed that it is very sensitive to external gases [49, 50], making E_F extremely mobile, even on very short range scales [51], which almost always results in strong band bending at the surface. The band bending is usually downward, keeping the surface E_F squarely in the conduction band [52–56] and producing a topologically trivial "well-state"[17] at the surface. These trivial surface states are susceptible to Rashba

[16]The proximity effect is the occurence of superconductivity on the surface of a material due to its close proximity to another superconducting material, not because the material itself is inherently a superconductor in those conditions.

[17]A quantum well state is a region in space where there exists a large potential drop, which can trap particles in that region, and greatly limits the available energy states within that region to equally spaced discrete levels.

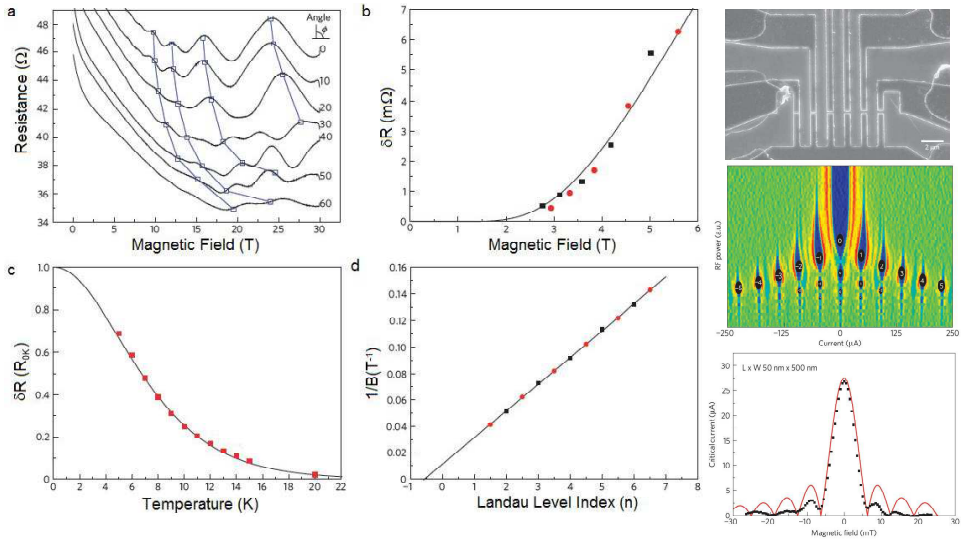

Figure 1.7: Figures of data confirming surface dominated transport and indicating the creation of Majorana modes in a josephson junction device involving Bi_2Te_3 [48]. The left graph shows analysis of SdH oscillations in the Bi_2Te_3 thin films, the nature of which indicate that the transport comes from the topologically nontrivial SS. The top right graph is an SEM image showing the Josephson junctions of the device and the quality of the surfaces. The middle and bottom left graphs show Frauenhofer patterns. The unusual shapes of the Frauenhofer pattern, which deviate from the standard model is taken as a sign that Majorana states are involved in the junction.

splitting in magnetic fields [49, 56, 57], causing the formation of concentric chiral Fermi surfaces (shown in Fig. 1.8) and there has also been conjecture that such an effect could occur in the bulk states, as has already been seen in a different Bi-based material [58]. This behavior of the trivial surface states makes the search for signatures from topologically protected surface states in magnetoresistance and Hall effect measurements even more complicated.

Even if the surface E_F is pulled to the Dirac point via gating, local variations in E_F persist, causing a charge puddling effect [30]. Despite the high sensitivity

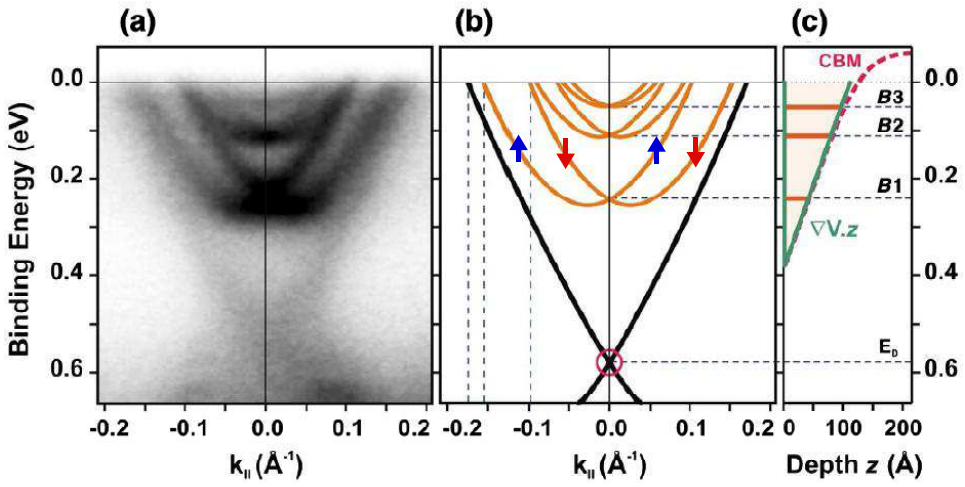

Figure 1.8: ARPES data (the left and center plots) clearly showing not only the topologically nontrivial SS crossing the bulk band gap, but also the topologically trivial 2D quantum well states (QWS) formed at the surface of Bi_2Se_3 from strong downward band bending in that region. The QWS, highlighted by the orange lines in the middle graph are split due to Rashba coupling, thus making the previously degenerate spin states (signified by the red and blue arrows) separate into an inner and outer surface, each having an opposite chirality. The right plot is a diagram illustrating the physical origin of the QWS at the surface.

of the chemical potential, controlled surface doping of magnetic materials shows - with ARPES - that the Dirac cone is not destroyed by local magnetism [59, 60]. Efforts to cap the surface of Bi_2Se_3 with another material that would preserve the topological states by preventing the uncontrolled reactions that cause the strong E_F bending and local variation have been mixed [61, 62].

Despite the progress made with materials like Bi_2Se_3 and Bi_2Te_3, the persistent chemical problems with the materials have led many groups to shift their efforts more towards finding other candidate TIs. In 2010, theorists predicted that a large number of materials within the same crystal structure family, known as Half Heuslers, had

the right band structures to be TIs [63–65]. Soon after, many of the predicted materials were shown to be topologically trivial [66], however, it was also discovered that some other Half Heuslers are superconductors [67]. A drawback of the Half Heuslers, however, is that they are zero gap semiconductors and therefore have no actual energy gap. An energy gap could be theoretically induced via uniaxial pressure along the [111] plane, but realizing this in experiment presents its own challenges. Since the initial reports on the Half Heuslers, not much more has been published on them within the field of TIs.

Another material that has garnered increased excitement recently is SmB_6. A well known Kondo insulator [68–70], SmB_6 was reported to theoretically have a topologically nontrivial band structure that would cause the familiar spin-locked states to form across the Kondo gap at low temperatures [71, 72]. The low temperature resistivity behavior of SmB_6 was already known to have anomalous behavior, deviating below 10 K from traditional exponentially growing resistivity, to flatten out to a resistive plateau, and conductive surface states seemed like a plausible explanation. The fact that this resistive plateau was not likely a bulk effect was shown with point contact spectroscopy [73], and bulk transport experiments utilizing unique geometries showed that the conduction path did indeed cross from bulk dominated to surface dominated over the same temperature range as the resistive behavior crossover [74–76]. ARPES experiments proved more difficult to resolve [77–82], however, due to the small size of the energy gap (20 meV). Most recently, however, experiments are showing more solid evidence that the conductive surface states in SmB_6 are topologically nontrivial [83–85].

This section has shown that the field of TI research is quite active and involves a wide range of experimental techniques. Controlling the bulk properties of TIs has also been shown to be a non-trivial matter[18], given that the phenomena of interest occur only on the surface of the materials. With the knowledge of the relevant concepts regarding TIs, the next section moves on to discuss the material properties of Bi_2Se_3, since it is the focus of this work.

1.2 Bismuth Selenide

Bismuth Selenide has been investigated by chemists, physicists, and engineers for decades before it was discovered to be a TI. Because of this, much is known about the material, like its basic physical properties, and the best growth methods.

Bi_2Se_3 was first investigated in the 1950's, along with other layered chalcogenides [86]. Soon after, it was discovered to be an excellent thermoelectric [87, 88], owing to its large Seebeck coefficient, and research on the material focused on controlling/improving this aspect of Bi_2Se_3 for many years. Its crystal structure and bonding type was investigated early on, one publication even mentioning the idea of band inversion [89]. Serious calculations of the electronic structure, however, weren't done until decades later [90]. With the advancement of thin film production techniques, many ways of growing thin films of Bi_2Se_3 were discovered in the late 90's and early 2000's [91–93].

[18] Pun intended.

1.2.1 Crystalline and Electronic Structure

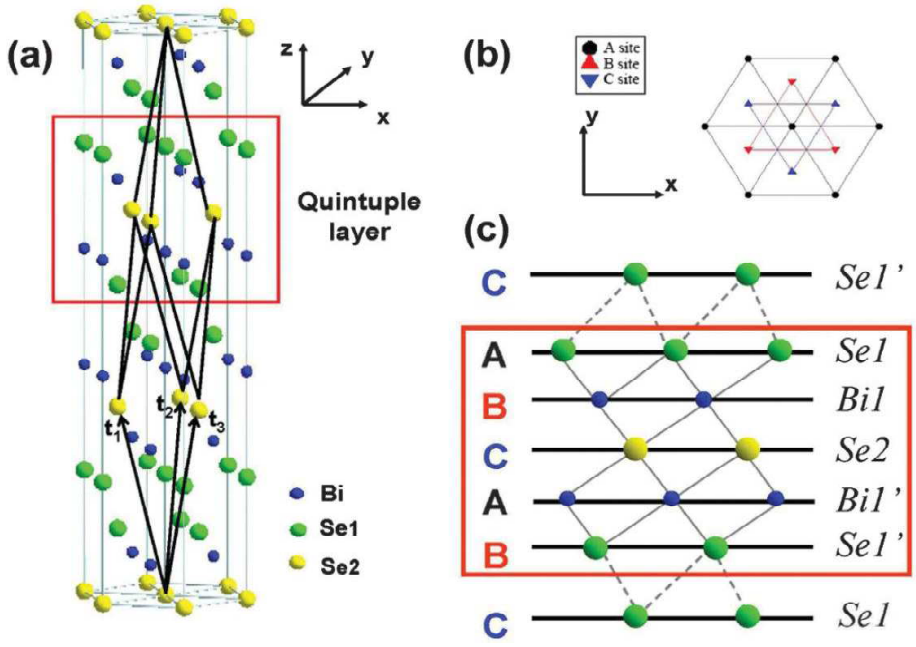

Figure 1.9: A Diagram showing the crystal structure (in real space) of Bi_2Se_3. [5]

Bi_2Se_3 is a loosely bonded material, made up of alternating sheets of hexagonally bonded Bi and Se, each one atom thick, as illustrated in Fig. 1.9. Like with Graphene, the stacking order plays an important role in the structure, and in the case of Bi_2Se_3, two alternating layers of Se and Bi (named Se1 and Bi1) are followed by a central Se layer (Se2), after which come two more Bi and Se layers (Bi1' and Se1') in stacking positions that mirror the first two layers, making a rhombohedrally classified unit cell [19], aptly named a Quintuple Layer (QL). It is the mirroring of the two Se and Bi layers (Se1 with Se1' and Bi1 with Bi1') around Se2 in real space

[19] The crystal structure is of the D_{3d}^5 space group.

that helps create the symmetric band structure about Γ in the Brillouin zone, which is crucial for the topology of Bi_2Se_3 [5].

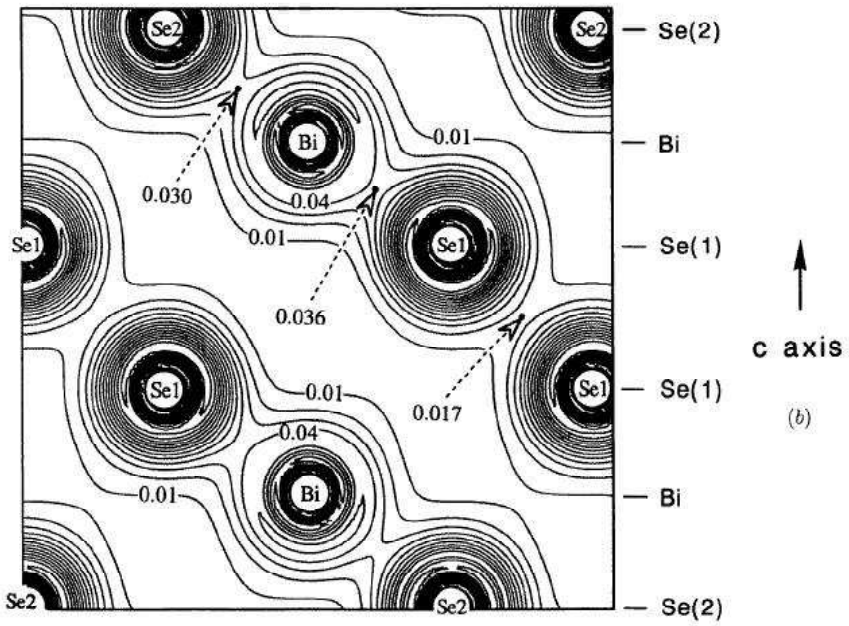

Figure 1.10: Diagram showing the bonding structure of Bi_2Se_3 in real space. Even though Bi_2Se_3 consists of alternating parallel single atom layers of Bi and Se, the bonding actually is strongest between those layers, in a diagonal manner. This bonding only occurs within the QLs, however, leaving only Van der Waals forces to keep the QLs together [90].

The bonds, surprisingly, are a covalent-ionic type ($pp\sigma$) diagonally across layers within the QL. The QLs are held together loosely by Van der Waals bonds. Fig. 1.10 illustrates the bonding geometry. From this chemical bond structure, the P orbitals from Bi and Se are responsible for the Energy states closest to the Fermi Energy, and therefore they play the crucial role in the band inversion that occurs in Bi_2Se_3. Fig. 1.11 illustrates how, taking into account increasingly higher order interactions leads from a situation where the Bi p orbitals are all degenerate and higher in energy

than the equally degenerate Se orbitals to the situation where the Se $|P2_z^-\rangle$ state is at higher energy than the Bi $|P1_z^+\rangle$ state. It is this inversion of bands of opposite parity, due ultimately to the SOC, that drives the change in Topology to the TI class. Diagram (b) in Fig. 1.11 shows the relative energies of the two orbitals as a function of SOC strength, showing that only 60% of the actual SOC strength is needed to make the two orbital energies equivalent, placing Bi_2Se_3 deep in the strong TI category.

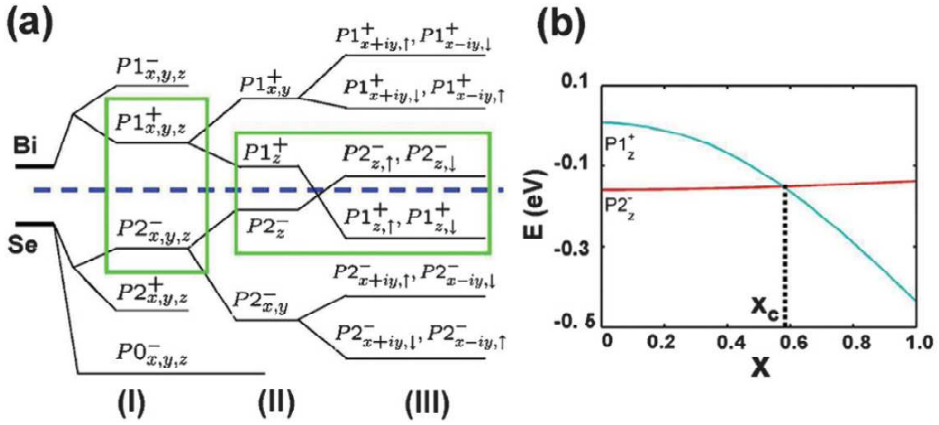

Figure 1.11: On the left is a diagram showing the origin of band inversion in Bi_2Se_3 . In step I, the energy levels for the P orbitals in Bi and Se are calculated from the basic chemical bonding of the material. Then step 2 takes into account the crystal field splitting, which lifts degeneracies in the orbitals, and finally III illustrates the change in energy levels when SOC is taken into account, pushing the $P1_z^+$ orbital of Bi below the $P2_z^-$ orbitals of Se, resulting in band inversion at the Γ point. The right figure shows how strong the SOC must be to cause this band inversion [5].

A more complete picture of the calculated band structure[20] of the bulk is shown in Fig. 1.12(a) showing the small energy gap at the Γ point. Part (c) of Fig. 1.12

[20]Calculations made using LMTO-LDA theory, not including calculations at the surface that take topology into account.

shows the Brillouin Zone (BZ) of Bi_2Se_3 along with the major symmetry points in the BZ. While the specifics of the band inversion are important for understanding the effects of topology on the physics at the surface of Bi_2Se_3, it is also important to understand the band structure in the bulk, as it dictates the effects of bulk defects in the material, which is a major focus of this work. As can be seen in the band structure diagram (Fig. 1.12), the dispersion relation of the conduction band around the Γ point along the *ab*-plane (F–Γ–L) than along the c-axis (a–Γ–Z) indicating that the Fermi surface made by E_f crossing the bottom of that band would have an ellipsoidal shape. The band structure calculations were checked with results from various experiments in the literature and Fig. 1.12(b) shows how well the theoretical calculations match. The energy gap in the $\hat{z}$ direction, and its similarities to the gap in directions along the *ab*-plane raises the possibility that Dirac cones would exist on surfaces normal to that plane and that the properties of the states on those surfaces may differ from the ones on other surfaces.

1.2.2 Common Defects

According to theoretical calculations, the E_f of Bi_2Se_3 should fall within the energy gap plotted in Fig. 1.12, which should make Bi_2Se_3 a true insulator at low temperatures. Combine this property with how readily the material forms using so many different growth techniques and Bi_2Se_3 should be the ideal TI. Unfortunately, as mentioned in previous sections, that is not the case.

It was noted, even in the earliest experiments on Bi_2Se_3 [94], that the material

was much more metallic than expected, with carrier concentrations much higher than theoretically predicted. The higher carrier concentrations come from Se site-vacancies that occur in the material during the growth process irrespective of the purity of the growth environment [95]. In the discussion of bonding in the previous section, the Bi atom acts as the cation and the Se atom the anion. It is thought that the high vapor pressure of Se, combined with the low binding energy of the Van der Waal forces between the two Se layers at the edges of the QLs facilitates Se leaving the material during at higher temperatures. These vacancies then leave the electron at the corresponding Bi site that would have participated in the site bonding free to occupy a state in the conduction band. It has also been proposed [95] that higher Se vacancy density also leads to a higher Bi anti-site defect density as well, which further lowers the sample quality.

The low strength Van der Waals bonds between QLs, in addition to contributing to the extremely layered nature of Bi_2Se_3 also makes the material highly prone to mechanical deformations and the types of defects associated with them. While the samples are known to be easily cleavable, with sheets of nanometers thickness able to be isolated with tape, the cleaving and layer removal processes also pose the risk of bending and/or scratching the material. Bending samples can introduce line defects and stacking faults, and scratching can severely degrade the surface. Both situations lower the mobility of the conduction electrons in both the bulk and surface regions.

In summary, the material Bi_2Se_3 has been of interest to the scientific community for a long time, with most of that interest coming within the last five years.

The renewed interest has come from the development of a new classification for materials, topology, which gives rise to exotic physics that produces unique macroscopic behavior resulting from quantum mechanical interactions. Bi_2Se_3 would be the ideal material with which to study these unique behaviors, except for the extrinsic properties arising from unresolved sample growth problems. Despite these problems, much progress has still been made in studying these behaviors, yet, similar to the field of superconductivity, many more advancements can be made if the persistent problems with sample quality can be overcome. The work discussed in this thesis is motivated by the goal of overcoming the sample growth problems with Bi_2Se_3, to achieve nonmetallic behavior without lowering carrier mobility, so that the topological SS can move beyond being a scientific curiosity to a useful phenomenon that can drive new technological developments. The techniques used to achieve this ultimately focused on the growth process, finding ways to controllably lower the inherent carrier concentration of Bi_2Se_3 without introducing dopants or impurities.

The next section will review the experimental methods used to produce and measure samples of Bi_2Se_3. Most of the analysis techniques will be discussed in parallel with the results, but one particular technique is covered in Appendix A. Chapter 3 will discuss investigations into the phenomenon of linear magnetoresistance (LMR), which has been noticed in thin films of Bi_2Se_3, but also emerges in low-carrier bulk samples. This phenomenon is shown to be clearly two dimensional and may be a signature of the topologically guaranteed SS. Chapter 4 describes the non-metallic behavior found in a small number of samples, as well as the highly

unusual magnetoresistive behavior of those samples, finally discussing the possible origins of this behavior.

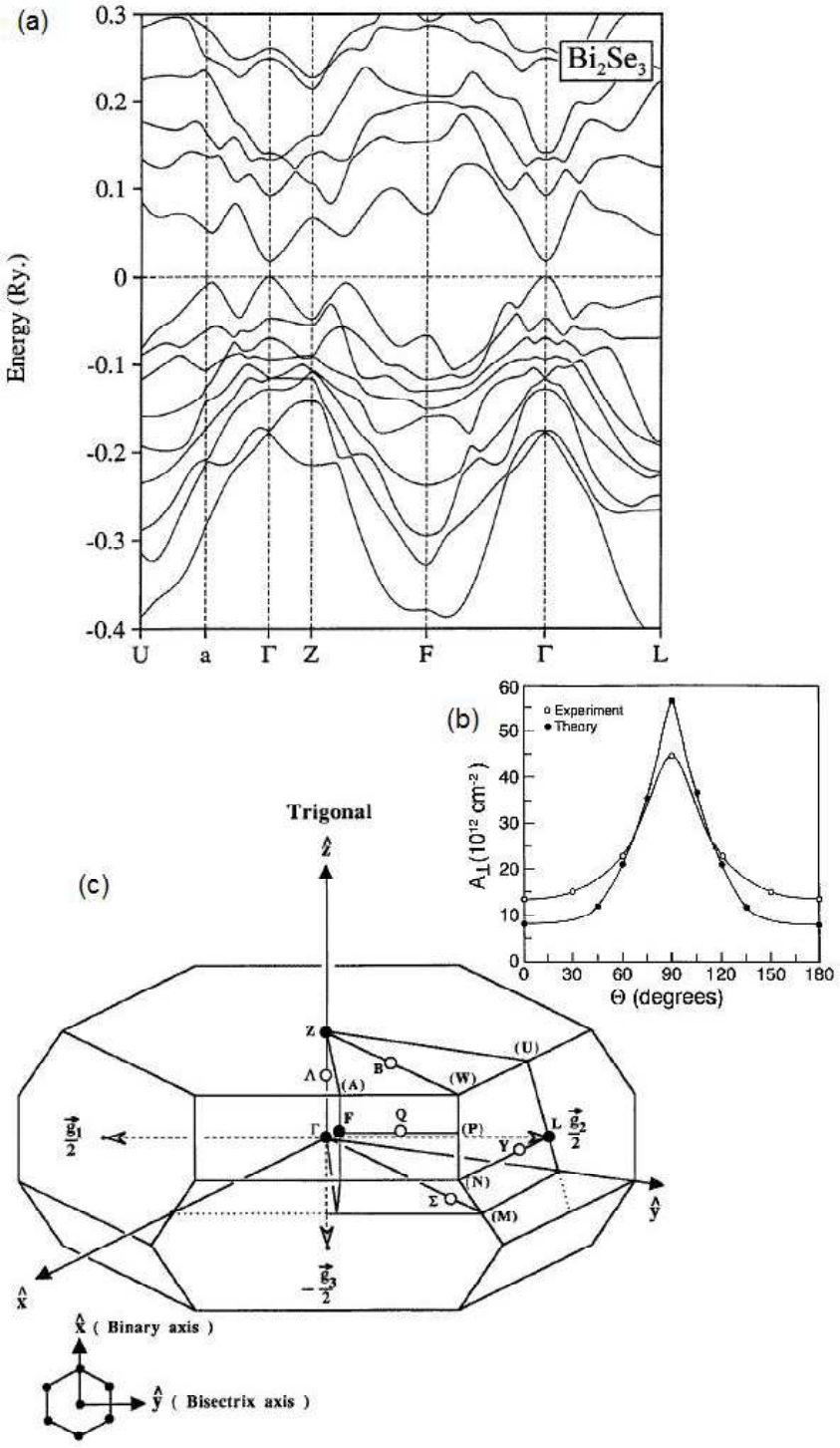

Figure 1.12: Diagram showing the calculated band structure of Bi_2Se_3. The calculations are of the bulk band structure, and therefore do not include the gap-crossing states at the surface. [90]

Chapter 2: Experimental Methods

2.1 Materials Synthesis Methods

The samples studied in this work were produced at the Center for Nanophysics and Advanced Materials (CNAM). That, combined with the fact that overall material quality as well as the specific properties studied in this work are directly coupled with the specific growth conditions of the samples, makes the materials synthesis techniques used significant in the discussion of the results. This section describes the various growth techniques used to produce the samples involved in this work.

2.1.1 Flux Growth

All samples of Bi_2Se_3 discussed in this work were prepared using the flux-growth technique, a common method used for bulk single crystal growth. The technique involves precipitating crystals of the desired material out of a solution of the required reactants[1].

A relatively cheap and simple technique, flux growth offers many practical advantages. All that is needed is a furnace, the raw materials for the growths, quartz tubing, a method to replace the air in the tubes with a nonreactive gas and

[1]This is the same process as sugar crystals forming in an over saturated mixture with water.

seal it off, and in some cases a crucible to hold the materials, so that they do not react with the quartz tubing. Another advantage that the flux growth method offers is that dissolving the reactants in a liquid flux allows the reaction of materials at temperatures well below the reactants' normal melting points, or the stoichiometric crystalization temperature of the growth material.

The basic procedure of the flux growth technique is that the required reactants are combined in a stoichiometric ratio with a material that has a melting point lower than the crystalization temperature of the material to be grown. The mixture is then heated in a furnace to above the melting temperature of the flux and held there long enough to allow the reactants to fully dissolve in the liquid. Then the mixture is slowly cooled, allowing the desired crystals to precipitate out of the solution. Given the high temperatures usually involved and the need to precisely control the environment of the reaction taking place, the measured reactants and flux are placed in a vessel, reffered to as an ampoule (usually a crucible and/or quartz tube) that can be completely sealed off from the outside environment. Before sealing the ampoule the air inside it is replaced with an inert gas, which is usually Argon.

The specific chemical processes involved in flux growth vary, depending on the material grown and the flux used. Sometimes the flux is an element or compound that is a component of the material being grown. For example FeAs is used as the flux in growing $SrFe_2As_2$.

Other times the flux is a different element or compound, like the case of growing SmB_6 where Al is used as the flux. In this case it is important that the flux material does not easily form compounds with any of the reactants over the growth

temperature range. This way the reactant amounts can be precisely controlled and the chance of precipitating out an undesired material can be minimized.

In the case of Bi_2Se_3 , excess Se was used as the flux, although Bi_2Se_3 is a "line compound" (as shown in Fig. 2.1) and can therefore be crystallized by simply melting stoichiometric amounts of Bi and Se. As mentioned in Chapter 1, the major type of defect that occurs in Bi_2Se_3 is Se vacancies. Therefore Se flux was used in an attempt to counteract the loss of Se during crystalization. Excess Se should push the chemical potential of the crystal formation reaction to hinder Se from leaving the crystal as it forms. The binary phase diagram of Bi and Se is shown in Fig. 2.1 and it shows that no compounds form, other than Bi_2Se_3 for mixtures with greater than 60% Se content. This provides advantageous conditions for growing Bi_2Se_3 in excess Se, because there is no worry of any unwanted crystal structures forming instead of or in addition to Bi_2Se_3.

Batches of Bi_2Se_3 were grown in varying amounts of excess Se flux to investigate whether or not the flux would shift the chemical potential during crystal growth, reducing Se vacancies, and to determine the ideal amount of excess flux for producing single crystals of good physical and electrical quality.

For standard growths[2] the preparation procedure was as follows. Amounts of high purity ($\geq$4N) Bi and Se shot were measured and combined in quartz tubes. For early growths, the materials were placed in Al_2O_3 crucibles but early on it was determined that the quartz itself was unreactive to the growth over the entire

[2]Standard being defined as flux growth batches not grown in either the pressure or modified bridgman furnace.

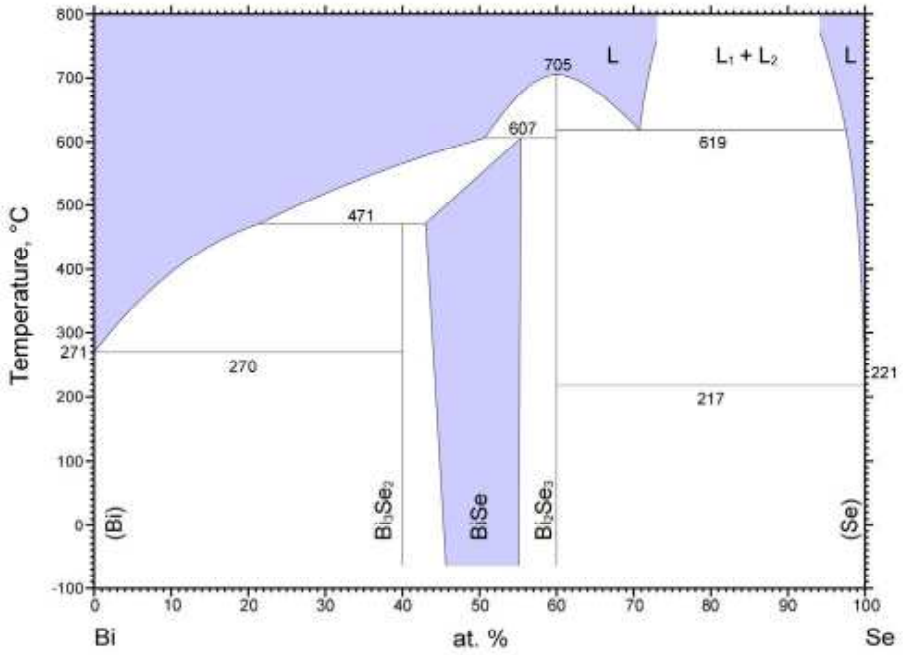

Figure 2.1: Binary Phase Diagram of Bi and Se, graphed as Se percentage. Figure obtained from ASM International alloy database [96].

temperature range used and later growths did not use the crucibles, instead placing the materials directly in the quartz tube. The reactants were then sealed in quartz ampoules under partial pressure ($\approx 1/3$ atm at room temperature) high purity Ar gas, to avoid any explosions at high temperatures, due to overpressure inside the ampoules. For this sealing process, the ampoules were hooked up to a closed system connected to a pump that could reach vacuum pressures of < 25 mTorr, evacuated[3], and refilled with high purity Ar gas a minimum of three times. The fourth time that Ar gas was introduced to the closed system, only enough was added to reach the desired partial pressure. After that, the quartz tube was melted shut using a small flame torch.

The general heating and cooling profile was relatively simple. Ampoules were placed vertically in the homogeneous temperature zone of a standard box furnace. They were heated at a fast[4] rate to 750 ^{o}C, held for a short period of time[5] before being cooled at -10 ^{o}C/hr to 650 ^{o}C. This temperature is close to, yet still above the crystalization temperature of Bi_2Se_3(see Fig. 2.1. At this point, the cooling rate was slowed down significantly[6] and the growths were cooled further to 450 ^{o}C, at which point the basic growth schedule was complete. Quenching in water, from 450 ^{o}C, was also tested, but that only proved to greatly increase the bulk carrier concentration of the samples. It is assumed this is because at higher temperatures, the Se is much more mobile within the formed crystals, resulting in more Se vacancies, and

[3]Pumped down to less than 40 mTorr pressure.

[4]Greater than 50 ^{o}C/hr

[5]between 4 and 12 hours.

[6]Slower cooling rates varied between -1 and -4 ^{o}C/hr, yet no systematic change in sample quality among these cooling rates was detected.

quenching to room temperature effectively freezes in the higher defect density.

Fig. 2.2 shows two pictures of typical flux growth batches. The top picture shows a batch with nearly stoichiometric amounts of Bi and Se, and the bottom picture shows a batch with a high amount of excess Se flux.

Including excess Se as a flux proved successful in reliably lowering the bulk n of Bi_2Se_3 samples over much of the range of the phase diagram. At a certain point, the excess Se began it impede the size and structural quality of the single crystals of Bi_2Se_3 that would grow, producing much smaller, more fragile crystals. Thus with this trade off between microscopic and macroscopic sample quality, an ideal Se growth concentration was found to be 78 – 82%[7]. After testing multiple excess Se amounts, the standard elemental ratio of growths became 3:8 of Bi:Se.

2.1.1.1 Effects of Pressure

Another variable that can be relatively accurately controlled with flux growth is pressure, given that the crystal growth takes place in a sealed ampoule. Usually the range of pressures reachable is only at or below atmospheric pressure at room temperature and the corresponding pressures for the same volume of gas at higher temperatures[8]. For some of the work discussed in this thesis, however, the flux growth method was used in a high pressure furnace, greatly extending the range of pressures under which Bi_2Se_3 could be grown.

The pressure furnace used was a Morris Research High Pressure Oxygen Sys-

[7]Given that the main goal of the research was not to systematically study the dependence of bulk n on excess Se, this should be taken as a rough estimate.

[8]If you remember the ideal gas law from introductory physics.

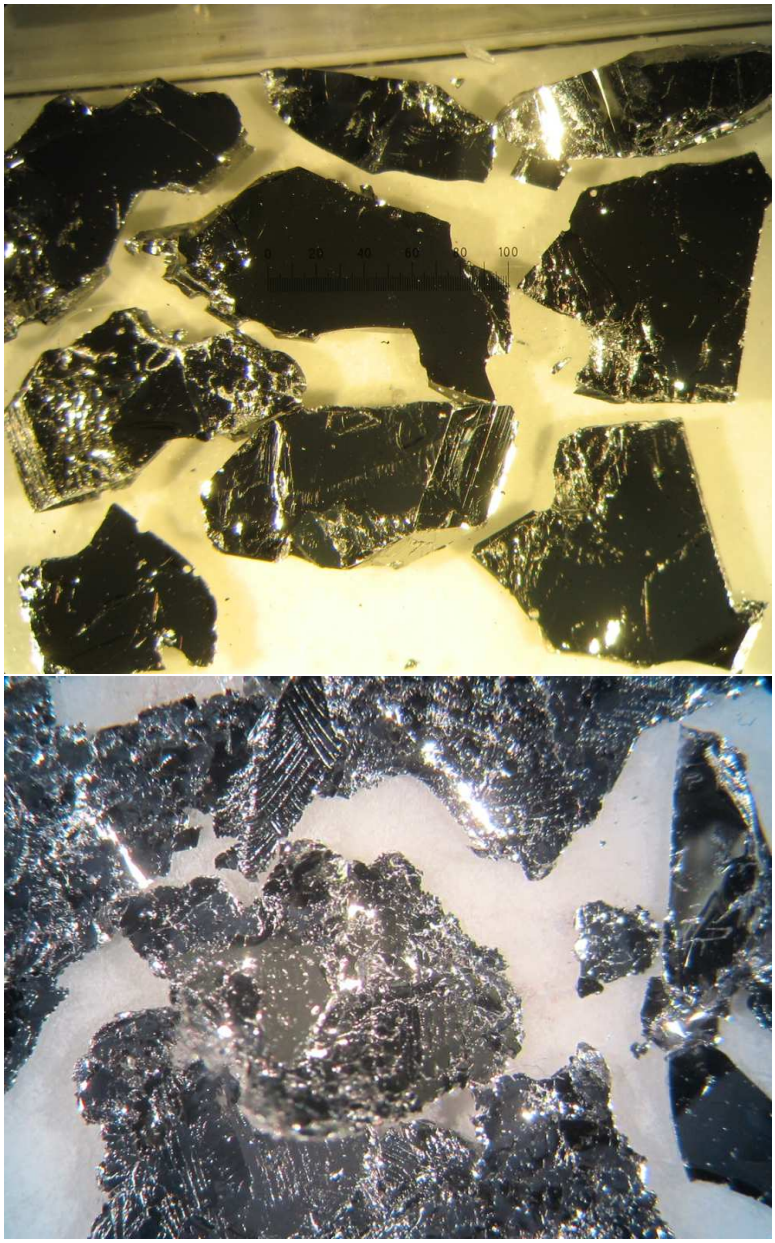

Figure 2.2: Two pictures of single crystals resulting from Bi_2Se_3 growths. The top picture shows crystals grown from a stoichiometric ratio of Bi:Se = 2:3. The bottom picture shows crystals grown in excess Se. The smaller thicknesses and jagged edges of the pieces in the bottom picture, as well as the many thin lines and dots that can be seen on them indicate that the crystal domains are noticeably smaller than in the top picture, and their surfaces appear rougher, due to amorphous Se remaining on the surface. Such differences, while apparently not significantly affecting the internal sample quality, has a negative effect on the physical properties that are important for electrical transport measurements.

tem (Model HPS 3210), which could safely handle pressures up to 200 bar. While 200 bar is nowhere near the high pressures reached by other pressure furnaces or in pressure cell measurements, it was sufficiently high to change the properties of Bi_2Se_3 samples, as will be discussed later. The original purpose of the pressure furnace had been for annealing cuprate superconductors in oxygen at high pressures, to accurately control the amount of oxygen doping in the materials. The furnace cavity was a long, thin tube of an industrial alloy, with an inner diameter 1 cm and hot zone length of 4 cm. The cavity was sealed shut by a steel cap that was screwed into place and fitted with a rubber ring to create an airtight seal. The furnace cavity was also connected to a pressurized gas cannister through a second opening, which was controlled by a series of valves. The furnace had been designed for the pressurized gas to be O_2, however, for the Bi_2Se_3 growths, Ar was used. The pressure inside the furnace was then controlled by the valves, which controlled the flow Ar into the furnace chamber and by a standard pressure regulator attached to the Ar bottle. The pressure in the furnace chamber could not be actively controlled throughout the growth process, and was instead set at room temperature before heating[9].

To fit the geometric and pressure requirements of the furnace very narrow quartz tubing (8mm ID, 6mm ID) was used and it was not sealed shut before placement in the furnace. The tube was also cut to be nearly as long as the furnace chamber itself, so that it could be both fully inserted and removed from the furnace. In order to prevent the growth from spreading out along the entire length of the

[9]After that, the pressure would change predictably, following the ideal gas law, in the absence of any leaks in the furnace.

chamber[10], the furnace was placed on a slight incline (approx. 5 ^{o}).

The room temperature pressure was tested with multiple growths, over a range of pressures from only a few extra bar to the maximum pressure for which the furnace was rated. Similar to the excess Se amount, more pressure was not always better, with the highest pressures producing growths with no single crystals of large or robust enough quality to be measured. The ideal room temperature pressure was determined to be roughly 40 – 60 bar. It was also discovered that a slightly faster cooling rate lowered n as well. The standard temperature profile for the pressure furnace became the following: the furnace was heated at as fast as possible to 750 ^{o}C and held there for 7 hours before being cooled at -300 ^{o}C/hr to 675 ^{o}C at which point the cooling rate was slowed to -9 ^{o}C/hr until 500 ^{o}C at which the cooling rate was sped back up to 15 ^{o}C/hr until it reached 350 ^{o}C/hr, after which it was cooled at 30 ^{o}C/hr down to room temperature.

The small inner diameter of the quartz tube used in the pressure furnace, combined with the high pressures and surface tension of the materials in their liquid form significantly hindered the mixing of elemental Se and Bi shot in the pressure furnace. Using powdered versions of the elements is also far from ideal, given their inherently lower purity level.

Two solutions to this problem were found. The first solution was to crush the Bi and Se shot before adding them in the quartz tube. The other solution tried, which became part of the standard method, was to pre-grow amounts of Bi_2Se_3 in a

[10]This was a real possibility, given that the quartz tube holding the growth could not be sealed off, and for retrieval purposes needed to be nearly as long as the entire length of the pressure furnace cavity.

box furnace (following the methods described in the previous section) and measure and crush an amount of pre-grown Bi_2Se_3 and use it as the growth material, to ensure an even mixture in the pressure growth.

In all batches of Bi_2Se_3 grown in the pressure furnace, droplets of amorphous, elemental Se was found in the quartz tube, a few millimeters away from the Bi_2Se_3 growth, indicating a significant amount of Se loss during the growth, most likely due to the vaporization and recondensation of elemental Se. It was determined from more than one batch early on, that, like the Bridgman growths discussed in the next section, carrier concentration varied systematically in the resultant growths. The lowest n samples came from the side of the growth closest to the recondensed Se and furnace exit, which, due to the incline was the higher side of the growth. The inclining of the furnace could have inadvertently caused a Bridgman-like effect in the growths, discussed in the next section. To combat both the Se loss and possible Bridgman effect, a small amount of extra elemental Se was placed at the bottom of the quartz tube[11], before the Bi_2Se_3 pregrowth was added. The reasoning behind the added Se is that once it becomes liquid, if the tendency is for the Se to drift towards the opposite end of the growth, then it must drift through the rest of the growth, resulting in a more even distribution of Se across the growth batch. Naturally, this increases the uncertainty in the overall Se percentage in the growth, but given the wide range of Se concentration that successfully produces low n Bi_2Se_3, this is not considered a significant concern.

Fig. 2.3 shows a picture of a typical pressure growth batch after it has finished

[11]The Se was added in the form of a crushed piece of shot.

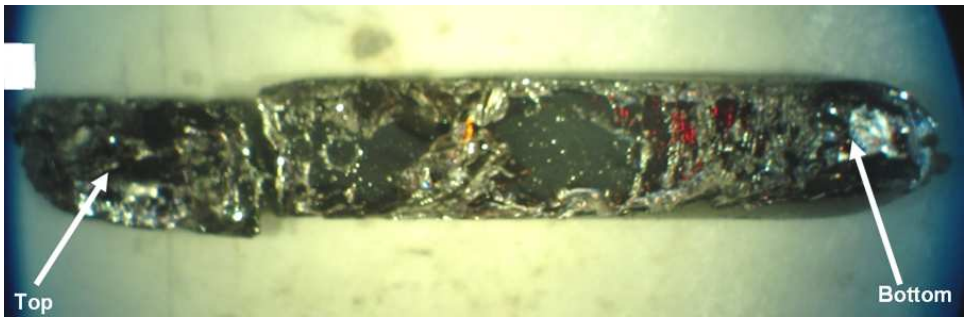

Figure 2.3: Picture of a typical pressure growth. The labels indicate which end of the growth was at the top of the incline and which end was at the bottom. The red shine is a thin film of elemental Se on the surface of the growth.

its growth cycle. The picture is marked, indicating which end of the growth was at the top of the incline and which end was at the bottom.

2.1.1.2 Removing Samples from Flux

In some cases, single crystals can be removed from a successful growth, without regard to the flux. In others, however, it is difficult to physically identify and/or fully separate single crystals from the amorphous flux. Once the growth has gone through its crystalization phase, the flux can be removed in two possible ways: it can be physically separated or chemically separated. For physical separation, at a high temperature — when the flux is still liquid — the growth can be inverted in the furnace, so that the flux will flow to the other end of the ampoule or the ampoule can be removed from the furnace and spun in a centrifuge. For some materials, the crystals are easily distinguishable from the solidified flux at room temperature

and the flux is soft enough to allow physical separation of the crystals.[12] When this is not possible[13] the flux can be removed by using an acid or other chemical that preferentially dissolves the flux material, but does not react with the desired crystals. Typical acids and solvents used for etching flux are HCl, H_2SO_4, HNO_3 and NaOH.

Even when it is possible to physically separate the crystals, there is still the possibility that small amounts of flux remain on the surface of the crystals, or that particularly large crystals have pockets of flux inside them, called inclusions. For the former problem, surface treatments, like sanding, polishing, or chemical etching are typically used. The latter problem is more difficult to identify and can usually only be solved by using a part of the crystal that is free of inclusions, either by breaking the crystal apart, or sanding it down to a region that is free of inclusions.

For the growths prepared in this work, the Se flux did not present any large problems for removing samples from the growths. Originally, growths were placed in a centrifuge to spin the liquid Se away from the crystals but it was later determined that such forces on the crystals at higher temperatures negatively affected the sample quality, so later growths were left to cool naturally in the furnace after reaching their final temperature in the heating profile. Given the closed nature of the pressure furnace, growths produced in it were always allowed to cool to room temperature before being removed. The amorphous Se was also neither the majority phase of the resultant growth, nor particularly hard, allowing removal of single crystals from

[12]Typical methods of separation include breaking the growth with pressure or percussive force, or prying the samples out using a blade or wedge shaped device.

[13]For example: the temperature at which the growth must be removed may be too high to safely spin it

the growth with a simple scalpel blade and tweazers.

For the higher n growths, the amount of Se flux was small enough, that nearly the entire growth became single phase Bi_2Se_3. For the lower n growths, there was enough Se flux to cause the Bi_2Se_3 to separate into multiple domains, with a thin layer of amorphous Se occupying the domain boundaries. This made separating samples a less arbitrary process, and it was determined that sample quality was best preserved in those growths, by causing the domains to naturally separate from each other, before individual samples were separated from the domains. Separating the domains was possible with slight external pressure[14].

Given the structure and properties of the bonds that form Bi_2Se_3 , discussed in Chapter 1, the thinnest platelets possible were sought. Thin samples would not only maximize the surface-to-bulk ratio, but also minimize the possibility of a sample containing a thin layer of amorphous Se between single crystal pieces. Once thin flakes were separated from the larger domains, the highest quality platelets[15] were chosen and their edges were sliced off with a scalpel, to create sample geometries more ideal for measurements. Utmost care was taken not to scratch or significantly bend samples, once they were removed from the growths.

2.1.2 Bridgman Growth

While environmental variables, such as temperature and pressure, can easily be controlled with a simple flux growth, sometimes a major problem becomes

[14]The pressure was usually provided by the flat part of a scalpel handle.

[15]Quality being determined visually by "shiny", unblemished surface and lack of platelet curvature.

crystals that form with multiple domains of different orientation. A crystal with multiple domains is of lower quality than a single domain crystal, due to the varying orientations of the domains, as well as the defects that occur at the domain boundaries. One underlying origin of these problems is that with basic flux growth techniques, one has no control over the location and number of crystal nucleation sites within the melt. If crystals begin forming at multiple locations in the ampoule, as the growth cools and the crystals grow large enough, the growing crystals will run into each other and the result will be a single crystal with multiple domains, originating from the multiple nucleation sites. One crystal growth technique developed by Percy Williams Bridgman and Donald C. Stockbarger is sometimes a useful solution to this problem with nucleation sites.

With the Bridgman[16] technique, the ampoule has a tapered or conical shaped bottom, that comes to a point. The ampoule then, instead of being placed in a furnace that provides a volume of uniform temperature, is pulled through a furnace with multiple temperature environments, or zones, as shown in Fig. 2.4. This effectively passes the ampoule through a temperature gradient, which passes down the length of the ampoule, melting and cooling the growth unevenly. The purpose of this is so that the bottom of the growth will begin crystal nucleation first, in the area where the growth doeas not have much room for multiple nucleation sites, making a single nucleation point most likely. Then as the temperature gradient moves down the ampoule, the crystal will grow from the single nucleation site at the end of the ampoule, rather than form a new nucleation site somewhere else. The result is then

[16]Also referred to, occasionally, as the Bridgman-Stockbarger technique

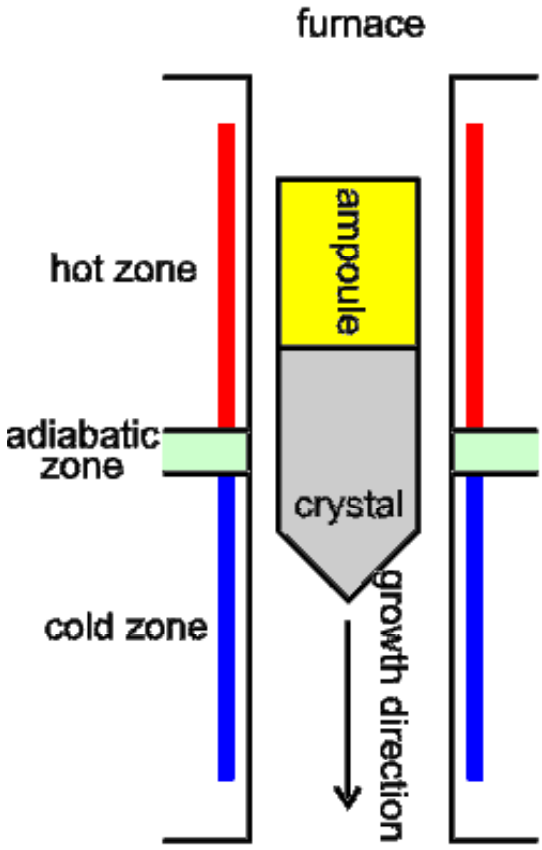

Figure 2.4: Diagram illustrating the Bridgman growth technique. In the conventional technique, the growth passes down the length of the furnace, from a hot zone, where the growth is liquid, to a cold zone, forming a moving adiabatic crystallization front. As shown in the diagram, the front of the growth ampoule in the Bridgman technique is pointed to maximize the probability of a single, or small number of crystallization points (kernels).

a large, single domain crystal beginning at the pointed end of the ampoule and, hopefully, extending down the entire length of the growth. Typically a Bridgman furnace is horizontal, or often set on a slight incline, and the temperature gradient in the furnace is static, while the ampoule is pulled through the furnace from one end to the other.

In producing some of the samples discussed here, we modified a three zone furnace to mimic a Bridgman furnace. A Lindberg/Blue furnace, model HTF5347C with three independently controlled heating zones, capable of reaching temperatures up to 1200 °C. We placed the furnace vertically, and hung the growths inside. Then, instead of pulling the growth through, we set the three zones to cool at coordinated rates, so that the temperature gradient would move through the furnace and the growths stay static. Given that the crystal formation temperature for Bi_2Se_3 is roughly 614 °C, the top two zones were set to higher temperatures. To begin, the top zone was heated to 1000 °C, the middle zone was heated to 790 °C, and the bottom zone was heated to 450 °C. After 12 hours, the middle zone was set to 715 °C, causing it to cool to that temperature by uncontrolled means. Six hours after that, both the top and middle zones were then cooled together at a rate of 1 °C/hr. With the center of the zones spaced roughly 20cm apart, the simplest model would estimate a temperature gradient of roughly 14.25 °C/cm.

In reality, the fact that the furnace was oriented vertically would certainly cause further inhomogeneity in the temperature environment, and a nonlinear temperature gradient. However, since the most important aspect of the Bridgman growth method is not the gradient itself, but the rate at which the material passes

through this gradient, these errors in temperature gradient homogeneity most likely do not significantly effect the growths in a negative way.

After 96 hours, the set temperature of the lowest zone was lowered to 400 °C to further facilitate an accurate cooling rate of 1 °C/hr for the higher zones. After a further 24 hours, heating of the bottom zone was cancelled and cooling of the top two zones at the same rate continued until the middle zone reached 330 °C and the top zone reached 615 °C. Once they reached their final temperatures, the furnace was turned off and the growth was allowed to cool at a natural rate. The total time for the growth was 16 days and 19 hours.

Fig. 2.5 shows a picture of one of the batches of Bi_2Se_3 grown in the modified Bridgman furnace. The clean, shiny faces with vertical cracks on the growth indicates single crystal domains stretching nearly the entire length of the growth, with the cracks being either grain boundaries, or faults introduced in the crystal in the opening and examination of the growth.

Two batches were grown with excess Se flux in the modified Bridgman furnace. It was noticed that samples taken from the top of the growths showed semimetallic behavior and some of the lowest n values obtained, whereas samples taken from the bottom of the growths had higher n values and showed metallic behavior. It is thought that this is due to a drifting of the Se flux to the top of the growth, as the temperature gradient passed up the ampoule, causing a much higher amount of excess Se at the top of the growth, than at the bottom[17].

[17]This effect is a possible cause of systematic batch inhomogeneity in growths produced in the pressure furnace.

Figure 2.5: Picture of a modified Bridgman growth. The labels indicate which end of the growth was at the top of the incline and which end was at the bottom.

2.2 Measurement Methods

The primary measurements taken for the studies discussed in this work are bulk transport measurements. They have the advantage of being simple, quick, and low cost. This chapter will describe the how the measurements are set up, what type of data is recorded, and in some cases, the basic phenomenon that is measured.

2.2.1 Electrical Transport

The entire realm of electronics is based on the principle of transporting electric charge from one location in a material to another, or across multiple materials. Different materials carry the electric charge differently, and these differences in properties are the result of different electromagnetic environments within those materials. These differences are generally considered as having two types of origins: intrinsic and extrinsic. Therefore the overall electrical resistivity is modelled in the following way

$$\rho(T) = \rho_0(T) + \rho_i(T) \tag{2.1}$$

with ρ_i being the intrinsic resistivity of the sample and ρ_0 being known as the residual resistivity. The residual resistivity arises from impurities and defects in the sample that cause the charge carriers that contribute the electric current to scatter, thus contributing to the "resistance" to the flow of electricity. In contrast, the intrinsic resistivity is material specific and usually changes significantly with temperature and originates from any of a number of different factors involved in interactions

among the atoms in the material. For example, Conductors are defined, not only as having low intrinsic electrical resistivity, but also as having a resistivity that is positively correlated with temperature.

Even the nature of the function that resistivity follows, vs temperature can give vital clues as to the types of interactions taking place in that material. For example, resistivity that follows a T^3 functional form at low temperatures indicates phonons are acting as the primary scatterers of electrons, and resistivity that is linear with Temperature — at low temperature — can be a sign of quantum criticality. For truly insulating behavior, if the resistivity is exponential in relation to $1/T$, then it is a sign that there is a gap in available conducting energy states, and can be modelled in the following way

$$\rho(T) = Ce^{\frac{-\Delta}{k_B T}} \tag{2.2}$$

where Δ is the size of the energy gap and C is a material specific coefficient. Materials that show a resistivity that increases with decreasing temperature without exponential behavior are generally referred to as being nonmetallic.

Phase changes in materials are often recognizable as jumps or kinks[18] in the function of electrical resistance vs temperature. One of the key properties of of a superconductor, for instance, is that at the temperature where it becomes superconducting, its electrical resistivity drops discontinuously to zero. Other externally tunable variables that are often used to track the behavior of electrical transport

[18]Jumps are points where the data curve is discontinuous and kinks are points where the first derivative of the curve is discontinuous.

properties include magnetic field, external pressure, and current density.

Electrical transport measurements are performed in the following way. Multiple electrical connections are made to a sample of the material being measured. Two connections, usually placed at either end of the sample, are used to pass an electrical current of a known strength through the material[19]. Then two more electrical contacts placed between the two current contacts are used to measure a voltage difference between them. Figure 2.6 illustrates the geometry of electrical contacts used for the measurements discussed. This is done in order to eliminate the possibility of voltages generated at the contact points of the wires to the sample. Using the values of the current and measured voltage ($V_+ - V_-$) along with Ohm's law, the resistance of the sample can be calculated. However, different samples have different geometries, which affects things like the current density and voltage difference during a measurement, so the more useful measurement is electrical resistivity (ρ), which accounts for such variations in geometry among different samples of the same material. Resistivity is calculated in the following way:

$$\rho = \frac{RA}{l} \tag{2.3}$$

where R is the measured resistance, A the crossectional area, and l the distance (along the direction of the current) between the two voltage contacts. While resistances of different samples may differ greatly, they should all have the same resistivity, if they are the same material[20].

[19]Thus earning them the name "current contacts".

[20]provided they are all samples of similar quality.

For all experiments in this study, Dupont air-drying silver paint (version 4929N) was used to make all electrical contacts with 2-Butyloxyethyl acetate used as a solvent, to help the paint achieve an ideal consistency for application. High temperature curing epoxies, soldering, and spot welding were not used due to the extreme sensitivity of the sample to heat. After the wires were first attached to the sample, they were then soldered to specific solder pads on the A/C transport PPMS measurement pucks or custom tails, in the cases of high field measurements. Preparation for these measurements usually took less than 30 minutes, and combined with the time required to choose and shape a sample, samples usually spent less than one hour in atmosphere before the first measurement. For all subsequent measurements (in studies looking at exposure effects), the amount of time spent air (in hours) was recorded.

2.2.1.1 Magnetoresistance

How a sample's electrical properties change as various other parameters of the material's surrounding environment are modulated can also reveal important information. Measuring the response to external magnetic field strength, a property called magnetoresistance, is commonly investigated. In order for the change in electrical resistivity due to a change in magnetic field to be brought into the context of the sample, magnetoresistance is defined as

$$MR = \frac{(\rho - \rho_0)}{\rho_0} \tag{2.4}$$

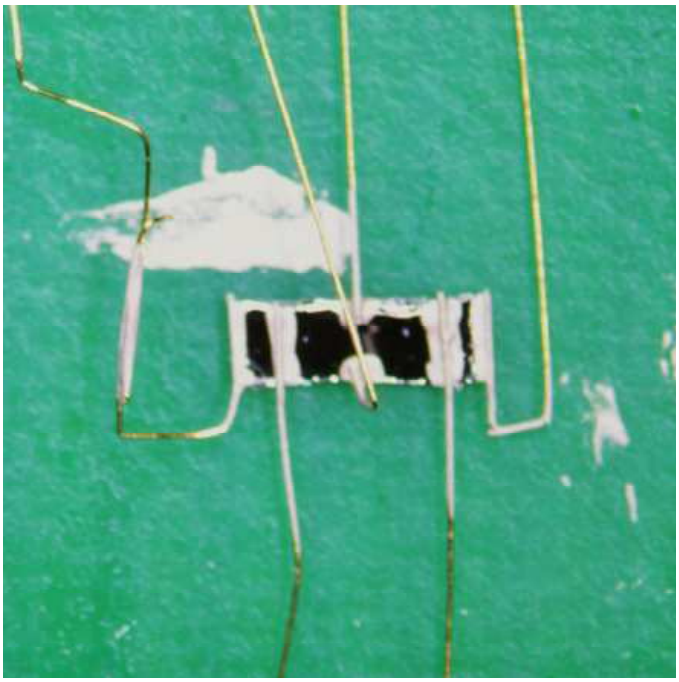

Figure 2.6: Photo illustrating the contact geometry for electrical transport measurement conducted. Contacts 1 and 2 are the current contacts, 3 and 4 are the longitudinal resistance contacts, and 5 and 6 are the Hall geometry contacts. The face shown is the ab-plane of a sample of Bi_2Se_3.

with ρ_0 being the resistivity value at zero magnetic field.

Observing large changes in resistivity with changes in field could have great importance, if the zero field resistivity is quite small by comparison, but they could be insignificant, if the zero field resistivity is even larger[21]. Classically, the magnetoresistance of materials is proportional to μB^2, at lower fields, where μ is the carrier mobility. Upon reaching significantly high fields, the magnetoresistance begins to saturate. The field at which this saturation begins varies from material to material.

Occasionally, however, materials show magnetoresistance behavior that is more strongly linear than quadratic, and shows no signs of saturation. This linear magnetoresistance (LMR) is almost exclusively a feature of thin film systems [97–99], however, it has been seen in a few bulk material systems [100–104], with multiple proposed explanations, usually involving inhomogeneity, of why the LMR occurs [100, 101, 105–107]. More recently Abrikosov [108] proposed an explanation for LMR that involves a gapless semiconductor in the quantum limit with conducting energy states that have a linear dispersion relation. As discussed in Chapter 1, the surface of a TI contains this exact zero-gap linear band situation. Since the experimental verification of the existence of TI's, other theorists have applied Abrikosov's theory to TIs with promising conclusions [109], which has added LMR to the list of possible signatures of the surface states in bulk samples, adding more importance to MR measurements.

[21] like in the case of SmB_6, for example

2.2.1.2 The Hall Effect

For most materials, the Hall effect is a simple result of the Lorentz force affecting an electrical current. The geometry of electrical contacts used to measure the Hall effect are shown in Fig. 2.6 It shows a linear response as a function of external magnetic field and the slope of this response (R_H) is related to the number of charge carriers in the following way

$$R_H = \frac{t}{ne} \tag{2.5}$$

where t is the thickness of the sample being meaured, n is the charge density[22], and e is the elementary unit of charge. Hall effect measurements are useful in such cases for directly determining the carrier concentration, using the above equation, and carrier mobility (μ) when combined with longitudinal resistivity values (ρ_0)in the following manner

$$\mu = \frac{R_H}{\rho} \tag{2.6}$$

However, some more complicated materials show Hall resistance vs field behavior that is very nonlinear. One origin of this nonlinear behavior arises from strong local magnetic interactions in the material and is known as the Anomalous Hall effect. However, since Bi_2Se_3 is nonmagnetic, the Anomalous Hall Effect is not applicable to measurements in this study.

Another origin of nonlinear Hall effect behavior is if the sample has two sepa-

[22]Number of charge carriers per unit volume

rate conduction bands that have different yet competing characteristics. This type of situation often arises in the case of doped semiconductors, where the electronic structure of the material contains both positive and negative type carriers. In the case of two opposite-carrier-type conduction bands within a single sample, their individual responses will be in opposition to each other. Normally one band would completely dominate the other in a field sweep at a single temperature, but if their properties [23] are comparable to each other, yet not similar enough to fully cancel out, then as the external field is changed, the overall Hall effect will change based on the interplay between the two bands. Drude developed a classical model to describe the resulting Hall effect in a two carrier system [1] with the equation

$$\rho_{xy} = \frac{{\sigma_1}^2 R_{H,1} - {\sigma_2}^2 R_{H,2} - {\sigma_1}^2{\sigma_2}^2 R_{H,1}R_{H,2}(R_{H,1} - R_{H,2})H^2}{(\sigma_1 + \sigma_2)^2 + {\sigma_1}^2{\sigma_2}^2(R_{H,1} - R_{H,2})^2H^2}H \tag{2.7}$$

with the σs being the conductivities of the two carrier types and Rs being their Hall coefficients.

This two carrier model also produces and equation predicting the behavior of the material's longitudinal magnetoresistance

$$\rho_{xx} = \frac{\rho_1\rho_2(\rho_1 + \rho_2) + (\rho_1{R_{H,2}}^2 + \rho_2{R_{H,1}}^2)H^2}{(\rho_1 + \rho_2)^2 + (R_{H,1} + R_{H,2})^2H^2} \tag{2.8}$$

however, this model does not predict the LMR discussed in the previous section. Hall measurements conducted in this work and their analysis using the Drude model

[23] carrier concentrations and mobilities

will be discussed in further detail in the Appendix A

2.2.1.3 Quantum Oscillations

In addition to the overall magnetoresistance, other phenomena can arise, which exhibit responses measurable in the magnetoresistance. The phenomenon discussed in this work in particular is Quantum Oscillations. QO are a quantum phenomenon, the origin of which can be explained in the following way.

In an electrically conductive crystal, the most loosely bound electrons are not actually localized to a specific lattice site. These electrons are referred to as conduction electrons[24] and their wavefunctions are instead modelled as nearly free electrons bound only by the dimensions of the crystal. In this new environment, the fermionic nature of the conduction electrons becomes nontrivial, since their wavefunctions now occupy essentially the same space. Fermions obey the following equation, relating to their wavefunctions

$$\Psi = \Psi_1(a)\Psi_2(b) - \Psi_1(b)\Psi_2(a) \tag{2.9}$$

Due to the fact that the two terms are subtracted, this means that no two fermions can be described by the same wave function.[25] This forces the electrons to differentiate their wave functions by energy. In other words, they must occupy different energy levels in the material, forcing them to "stack" and occupy higher and higher

[24]Given that one mole of material contains 10^23 atoms, even if one electron from a fraction of the atoms in a material becomes a conduction electron, that is still a large enough number for the principles of statistical mechanics to apply in macroscopic systems.

[25]This is famously known as Pauli's exclusion principle.

energy levels after the lower ones become occupied (as illustrated in the top part of Fig. 2.7).

In the absence of potential energy terms, all the energy that a conduction electron possesses, beyond its restmass energy, comes in the form of kinetic energy, also expressed as momentum. Thus the conduction electrons occupying the highest energy levels[26] in a material therefore have the highest momenta. Momentum is directionally dependent, and therefore, if one plots the momentae of all conduction electrons in the material in momentum space, they would occupy a three dimensional volume, as can be visualized as the dashed line in the bottom diagram in Fig. 2.7. The outer surface of this volume represents all the conduction electrons in the highest energy level — known as the Fermi energy, E_F — of the material, their wavefunctions differentiated by their momenta. This surface in momentum space is named the Fermi surface and the electrons that exist on this surface are responsible for the electromagnetic properties of the material.

When this material is placed in an external magnetic field, the available energy levels of the system change in momentum space, forming a set of cylinders, concentric along the direction of the magnetic field. These cylinders, or rather the energies corresponding to their absolute momentum values, are known as Landau Levels. The top diagram in Fig. 2.7 shows the normal energy level occupation (red line) being split into the evenly spaced Landau Levels (blue and green spikes). All the electrons in the system must still "stack up" and therefore they fill up these Landau Levels,

[26]In other words, the conduction electrons at the Fermi Energy, labeled in the top diagram in Fig. 2.7.

placing E_F either within a single level, or part way between two different levels. If E_F falls between two levels[27], then the nearest unoccupied energy states are in the next Landau level, which requires a significant amount of energy to reach, which makes electron transport slightly more resistive. Contrastingly, if E_F falls within a level, then the level is only partially filled and therefore unoccupied energy states are located in close proximity to occupied energy states, making electron transport less resistive. The Landau Levels are equally spaced in energy, and therefore momentum space, and their spacing is determined in the following way

$$a = \left(n + \frac{1}{2}\right) \frac{2\pi e H}{\hbar c} \tag{2.10}$$

Since the energy spacing of the Landau Levels depends on the strength of the magnetic field, the levels will become more spread out as the field increases. This leads the system to alternate between the two environments described (illustrated in Fig. 2.7. The sample moves smoothly from one environment to the other and back, with the energy gap between E_F and the nearest LL changing continously as the magnetic field is changed continuously and correspondingly the electrical conductivity (or magnetisation) of the material smoothly increases and decreases. This oscillatory behavior in the measured properties is named Quantum Oscillations (QO). More specifically, oscillations in magnetization are named de Haas van Alphen, after their discoverers and oscillations in resistivity are named Shubnikov de Haas oscillations. Shubnikov de Haas oscillations are the only type of QO mea-

[27] As is the case in the top diagram of Fig. 2.7

sured in the work discussed here, so the term QO refers only to Shubnikov de Haas oscillations, onless otherwise stated. Since the spacing between the LL continuously increases, the frequency of the QO decreases with increasing field. This is an inverse relationship, so when the oscillations are plotted vs inverse field, their frequency is constant. From the QO frequency, a useful relationship can be used to calculated the carrier concentration in the sample.

Since LLs are actually cylinders in momentum space that are isotropic along the field direction, they interact most with the parts of the Fermi surface where the curvature with respect to that direction is minimal. These are the extremal cross-sections[28] of the Fermi surface orthogonal to the field direction, given the variable $A_\perp$, and since the QO frequency of the material is related to the area of the LL cylinders as they cross the fermi surface the frequency is correspondingly related to $A_\perp$ with the following equation, known as the Onsager relation

$$f = \frac{c\hbar}{2\pi e} A_\perp \tag{2.11}$$

where e is the elementary charge. For a spherical Fermi surface, $A_\perp = \pi {k_f}^2$, where k_f is the magnitude of the radius of the Fermi surface (named the Fermi vector) and is related to the carrier concentration of the sample in the following way.

$$\textbf{3D:} k_f = (3\pi^2 n)^{1/3} \tag{2.12}$$

$$\textbf{2D:} k_f = \sqrt{2\pi n} \tag{2.13}$$

[28] cross-sections of minimal and maximal area

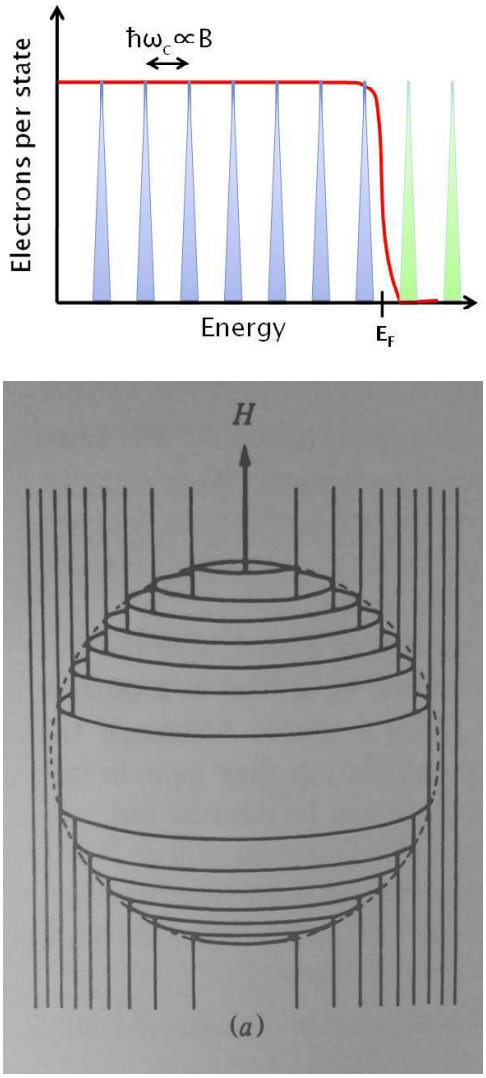

Figure 2.7: Illustration of the formation of Landau Levels (top diagram) and Landau Tubes (bottom diagram), with respect to the Fermi energy and surface of the material [1].

and because the anisotropy of the Fermi surface of Bi_2Se_3 is small enough, it can effectively be modelled as a sphere. Because of these relationships, QO can also serve as an independent measurement of the carrier concentration of a sample[29]. This effect can be used to map out not only the size, but also the shape of the Fermi surface of materials by tracking differences in the frequency of QO of a sample at different orientations. In the case of materials with multiple Fermi surfaces (multiband materials), the QO will exhibit multiple frequencies.

Frequency is not the only property of QO that can yield useful information about the sample. As the size of the external field increases, so too does the amplitude of the oscillations. This comes from the fact that the conduction electrons invariably scatter as they travel through the material, which dampens the QO. The level of scattering depends on multiple factors, including the carrier mobility, and is approximated by a relaxation time, τ. As the field is increased, the QO overcome this scattering more and more, and thus are dampened less and less. This field dependent damping behavior is modeled by the equation

$$R_D = \exp(-2\pi^2 k_B \tau m^*/\hbar e B). \tag{2.14}$$

Finite temperature also has a damping effect on the oscillations: as the temperature increases, the Fermionic occupation function broadens out, making the Fermi surface "fuzzier". Rather than damping the oscillations by spreading the

[29]For instance, multiple QO frequencies are a sign that a single carrier model for the Hall effect is probably not accurate. Another instance would be if there is a significant discrepancy between n calculated from Hall effect measurements and QO measurements.

conduction electrons out across multiple LLs, the thermal energy actually causes phase smearing of the carriers, which has a much larger effect. Using the expected behavior of the Fermi distribution, the damping due to phase smearing from thermal energy is described by

$$R_T = \frac{\alpha T B^{-1}}{\sinh \alpha T B^{-1}} \qquad \alpha = \frac{2\pi^2 k_B m^*}{\hbar e} \tag{2.15}$$

which is known as the Lifshitz-Kosevich formula.

Thus, in modelling the oscillations in inverse field, including the damping terms, the full equation to approximate the SdH oscillations is

$$\frac{\Delta\rho}{\rho_0} = \frac{\alpha T B^{-1}}{\sinh \alpha T B^{-1}} \exp(-2\pi^2 k_B \tau m^*/\hbar e B) \cos 2\pi(f + \gamma) \tag{2.16}$$

and γ being the intrinsic Berry's phase. As mentioned earlier, in section 1.1.1, the intrinsic Berry's phase is usually zero for materials, but for the topologically nontrivial SS, γ is intrinsically π [110, 111]. However, other factors like the phase slipping that contributes to the temperature dependent damping, can also affect γ.

Recently, a field dependent phase shifting effect due to a finite effective mass and spin orbit coupling was proposed for the SSs. The theory, outlined in the paper by Taskin et al. [111] models the effect with the following equations

$$E_N^+ = hbar\omega_c N + \sqrt{2\hbar v_F^2 eBN + \left(\frac{\hbar\omega_c}{2} - \frac{1}{2} g_s \mu_B B\right)^2} \tag{2.17}$$

$$\gamma = \frac{m_{eff} v_F^2}{\hbar \omega_c} + \left(1 + \frac{E_N}{m_{eff} v_F^2} - \sqrt{1 + \frac{2E_N}{m_{eff} v_F^2}} \right) - N \tag{2.18}$$

As can be discerned from the above equations, the four independent parameters in this model are the oscillation frequency (F), effective mass (m_{eff}), Zeeman coupling (g_s), and the Fermi velocity (v_F). It is important to note that current theories that describe the Hamiltonian for TI surface states consider the parameter v_F differently from its standard relation $v_F = \hbar k_F / m_{eff}$. Instead, in the Hamiltonian, v_F describes the strength of the linear dispersion behavior and therefore v_F must be considered an independent parameter. Previous studies, both theoretical and experimental predict values of v_F over the range 3 – 5 x10^5 for Bi_2Se_3.

Thus with these equations, QO can be modeled in great detail, after a proper background subtraction, details of which are given in Appendix A, and the resulting fits can give estimates for a number of different important physical parameters such as n, μ, and γ. Even if full, direct modelling of the oscillations is not possible, some details of the oscillations can usually be determined with some accuracy by taking a Fourier transform (in reality a simple FFT) of the oscillatory component of the MR over which the oscillations can be seen. The result of the transform provides a spectrogram of the MR, with resonance peaks at the frequency(ies) of the oscillation(s). FFT's of multiple curves at increasingly higher temperature will show the typical Lifshitz-Kosevich behavior. Therefore fitting equation 2.15 to the temperature dependence of the peak heights or areas[30] can give estimates of m_*.

[30]In almost all cases, the data must be normalized to the lowest temperature FFT, and the equation adjusted correspondingly, since FFT peak sizes do not correspond purely with physical parameters.

Performing FFTs on multiple small sections of a single background subtracted MR curve can similarly show the rough field dependence of the oscillation amplitude(s). Just as with the temperature dependence, using the equation for the damping factor R_D to fit the peak heights and/or areas vs average field of each FFT can give an estimate of the Dingle temperature.

Unfortunately, the FFT yields no information about γ. However, plotting the inverse field values of the extrema (minima and maxima) vs their correct index (minima in resistance having integer values and maxima integer plus half values) can provide this information. Such plots are known as LL-index plots. In materials with low spin orbit coupling, the slope n/B^{-1} provides an independent check of the QO frequency, and the x-intercept position gives γ. For a material like Bi_2Se_3, however, the spin orbit coupling adds a nonlinear component to the QO, manifesting as a coherent drift in phase with increasing field[31]. This phase drift, however, can be modelled by equations 2.17 and 2.18. Fits to the LL-index plots can reveal not only the intrinsic phase shift γ, but also in cases of significant phase drift, the fits can provide an adjustment factor to the actual oscillatory data itself. Taking this phase drift into account can add increased accuracy to FFT analyses.

This section has summarized the physical origin of Quantum Oscillations and the relevant equations that model their behavior. QO are clearly very useful for characterizing materials in general, and in the case of TIs they can provide uniquely crucial information. Just by measuring and analyzing oscillations in MR at different

[31]The use of the term coherent here is to distinguish from the "phase slipping" mentioned earlier as a damping factor. The type of phase drift discussed here does not result in significant damping of the oscillations.

orientations and temperatures, it is possible to determine if the Fermi surface that gives rise to them is a topological SS, by determining 2D or 3D, as well as its inherent Berry's phase shift. Furthermore, analyzing the QO can tell how mobile the carriers in the sample are.

As mentioned in section 1.1.3, QO measurements in thin films are already used as an important characterization technique for samples and devices. Unfortunately the same measurements in bulk samples have not yet proven very useful for characterizing SS properties, but with further advancements with bulk samples[32] they will provide one of the most useful tools for experimentalists.

2.2.1.4 Measurement Apparatuses

Cryogenic techniques are used to achieve temperature control over the temperature range from room temperature down to lowest temperatures reached in this work. In a nutshell, cryogenics are the cooling of things by transferring heat to very cold liquids. In the most common case, liquid helium is used, which has a boiling temperature of 4.2 K at atmospheric pressure, which can be lowered to 1.5 K in ultra high vacuum. There are other techniques available to achieve temperature below 1.5 K, but they were not needed for this study.

A Physical Properties Measurement System (PPMS), designed by Quantum Designs, was the primary cryogenic system used in this work. The PPMS is a self contained, user friendly system that allows for precise control of sample tempera-

[32]Improvements either in sample quality of known TIs or the discovery of new TIs with SSs that are more dominant in transport signals.

ture and orientation, as well as electric and magnetic fields (in the form of electric currents and external fields). In the ordinary set-up, temperature is controlled by pumping liquid ^{4}He into a chamber in good thermal contact with the sample. By precisely balancing the cooling power of the liquid helium with the heat being supplied through a resistor placed near the sample, the PPMS is able to stabilize temperatures from 1.8 K to 320 K with 0.01 K accuracy.

The user interface is the main advantage to the PPMS as it is a complete program designed for easy use, with set calibrations, safety features, and analysis algorithms. Samples are mounted on interchangeable PPMS pucks and then inserted into the bottom of the PPMS dewar. At the University of Maryland there are two PPMS set-ups capable of applying fields of up to 14 T or 9 T, respectively. The types of pucks used for this work used A/C current, with low current amplitudes ($\leq$ 2 mA) and frequency (17 Hz). Both PPMS systems allow the insertion of a special rotator probe, which allows single axis control of the sample position by rotating the puck on which it is attached around a horizontal axis.

For the measurements in Toulouse and Los Alamos, custom cryostats were used, however their general operational techniques were the same. Temperature control in those systems was not as accurate between 250 K and 50 K. Pulsed field techniques were used to reach the high fields at the two facilities. Instead of using superconducting magnets, as is done in the PPMS, the high fields are generated using normal electromagnetic coils and large capacitor banks. The capacitor banks build up extremely high charges and then release them through the coils in short pulses. The extreme change in current produces the extreme magnetic fields used in

measurements. Because the capacitor discharge is so quick, and because such a large input of energy into the coils heats them, the external field used in measurements goes from near zero to its peak and back down in one second or less. Due to this short time-span, the frequency of the AC current being passed through the samples was a few kHz, which is much higher than the frequency used in the PPMS. Checks were performed at both locations to make sure that the sample response was still ohmic in moving to a much higher measurement frequency.

2.2.2 Spectroscopy

Energy dispersive X-Ray Spectroscopy (commonly referred to as EDS or EDX) is a method of analyzing the chemical composition of materials. EDS is one method of type of analysis performed by a Scanning Electron Microscope (SEM). The SEM operates on the reverse of the photoelectric effect, by which it bombards a material with high energy electrons, which scatters core electrons from the atoms in the sample, releasing X-rays as they leave the atom.

For EDS, a detector is placed directly over the sample which measures the characteristic X-rays emitted by the sample in response to the impinging electron beam. For EDS, the full range of X-ray energies is measured at one time, allowing quick determination of which elements are present in the material.

The advantages of EDS are than it provides quick and detailed chemical analysis on single crystals, without destroying them. Secondly, SEM technology has become widespread enough that access to an SEM that can perform EDS is rela-

tively easy. The drawbacks of EDS are that, given its use of charged particles, it is only sensitive to the material at or near the surface that it measures. While EDS is ideal for thin films, it is not as effective when searching for inclusions or defects that may be hidden in the bulk of large samples. Secondly, EDS can only detect an element concentration to an accuracy of roughly 1-3% in a material. This is because many elements have overlapping spectroscopic peaks. The surface roughness of a material can also reduce the effective accuracy of EDS measurements, causing X-rays to scatter in directions outside the range of the detector. Wavelength Dispersive Spectroscopy uses a more targeted X-Ray detection process to provide estimates of elemental composition to within a fraction of a percent, however in being more advanced, WDS is usually performed by specialists with their own equipment, not in-house.

For the work discussed here, EDS was used to check the overall quality of samples. X-ray crystallography is not discussed in this work because it was conducted less often, due to the fact that it had been extensively checked in earlier studies of Bi_2Se_3 [41] and the general growth process was not changed for this work, giving no large concern that there would be such a drop in quality that would be detectable by X-Ray diffraction.

Chapter 3: Investigations of Linear Magnetoresistance

Over the course of characterizing many samples of undoped Bi_2Se_3 as part of the work to produce nonmetallic samples, other unusual properties were observed. As part of the early work led by Dr. Butch [41], it was noted that samples with lower n showed magnetoresistance behavior that deviated more strongly from the classical H^2 behavior. As carrier concentration was lowered, the overall MR of samples increased and showed an increasingly dominant linear behavior. Part of this work investigates the characteristics of this LMR: examining the effect across many samples and investigating its dependence on sample orientation and aging.

Early efforts were also successful in lowering n to the point where only moderate fields were necessary to push samples into the quantum limit[1]. With this ability to easily reach the quantum limit, studies were then conducted at extremely high magnetic fields, to probe the magnetoresistive behavior of samples with their bulk carriers completely in the first LL. The possible observation of QO at high fields will also be discussed in this chapter. While these oscillations are observed over field ranges where the bulk states are already in the quantum limit, other details about the QO differ from what would be expected from the topologically nontrivial SS.

[1]The quantum limit is the term given when all conduction electrons are in the lowest landau level, at which point QO are no longer possible.

From the many growths produced in this study, samples of a wide range of carrier concentrations were measured. As expected, as the carrier concentration was lowered, the resistance generally increased, with some of the lower carrier concentrations showing sample resistances above 10 Ω at room temperature. This increased in resistance was not, it turned out, due to a reduction in carrier mobility, with the majority of samples measured still showing bulk mobilities of at least a few thousand cm^2/Vs (as can be inferred from Fig. 3.1). Therefore when samples showed ρ_0 values of greater than one ohm, it was taken as a circumstantial sign of low n, rather than low quality. Across the many samples measured, the value of the linear component (in units of Ωcm/T) was noted and Fig. 3.1 shows those values plotted versus bulk carrier concentration (upper plot) and mobility (lower plot) for a representative selection of the samples meaured.

The top plot of Fig. 3.1 confirms the notion that there is an overall relationship between the strength of the LMR and carrier concentration. Power law fits to the data indicate an inverse square relationship. The solid line traces just such a function ($y = Ce^{-2x}$) which illustrates the correlation but is not an exact fit. The mobility, in contrast, does not seem to play a role in determining the strength of the LMR in samples.

3.1 Angular Dependence

Electrical transport measurements were carried out using the techniques described in section 2.2.1 on the rotator insert in the PPMS systems (see section 2.2.1.4

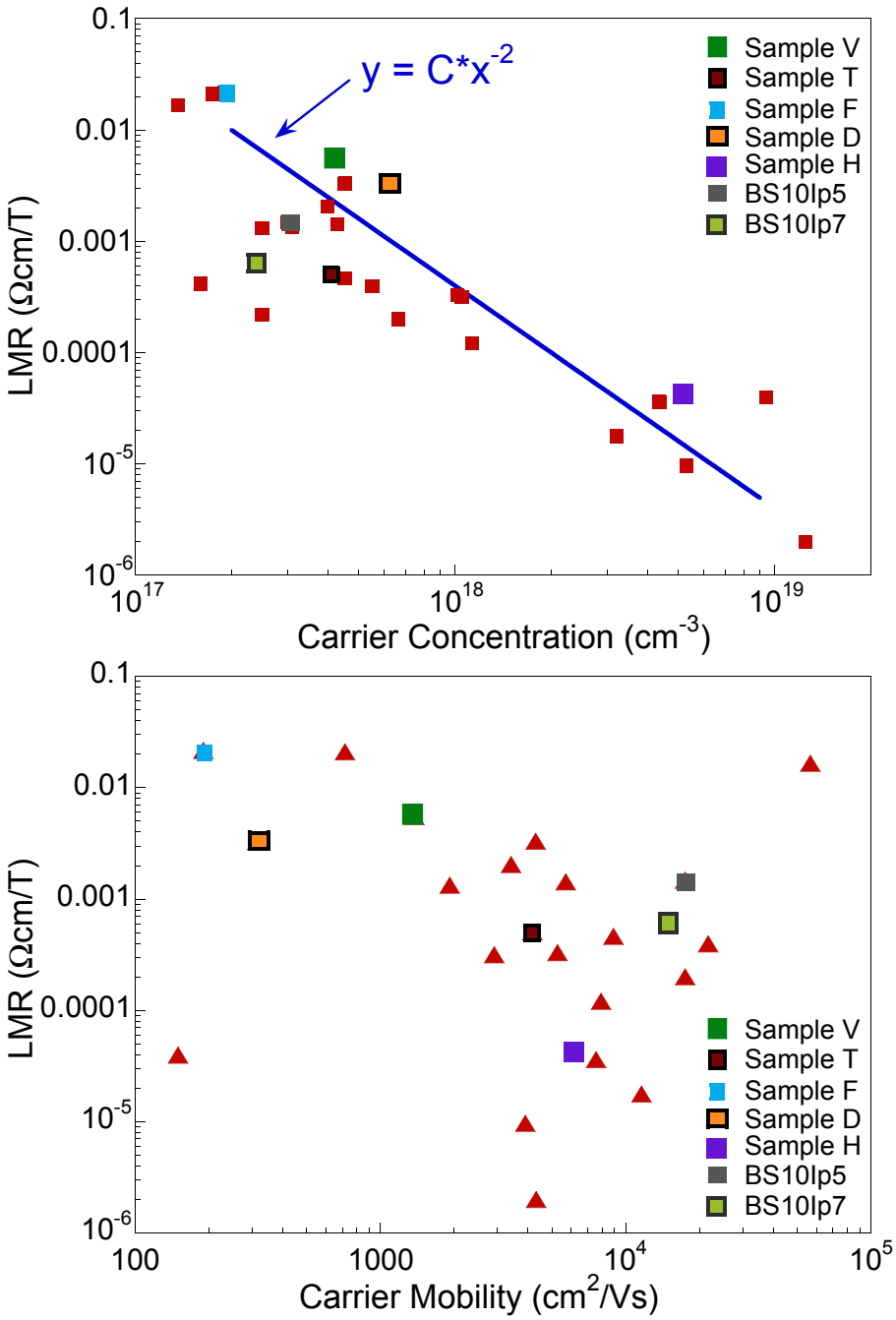

Figure 3.1: Logarithmic plots showing the size of the linear component of the MR above $\approx$ 4 T in samples of Bi_2Se_3 . The top plot shows the slope vs bulk carrier concentration and the bottom plot shows the slope vs bulk mobility. The top plot shows no strong dependence of the LMR on sample mobility. The bottom plot does show some dependence of LMR strength on carrier concentration, as previously noted [41]. The relationship seems to loosely follow a power law, as emphasized by the solid line, which is a x^{-2} function.

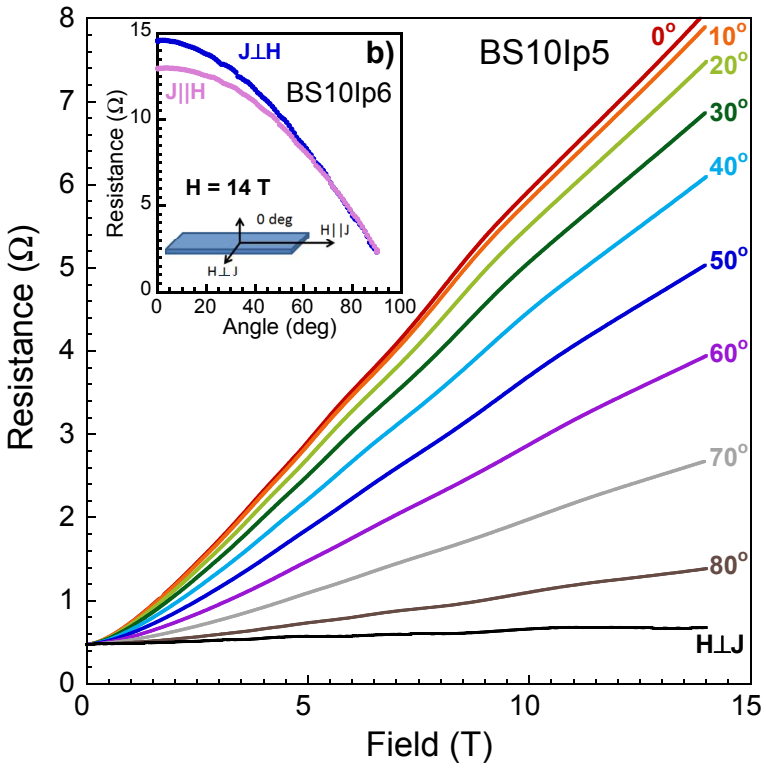

Figure 3.2: Plots showing the magnetoresistance behavior (at or below 2 K) versus Angle for high pressure grown samples of Bi_2Se_3 . The main figure shows the raw resistance vs Field at different angles, and the inset highlights the similar 2D behavior of the magnetoresistance when the field is both both orthogonal and coplanar with the current direction.

for details). Fig. 3.2 shows the magnetoresistance of a sample, grown in excess Se inside the pressure furnace, up to 14 T at various angles, which changes dramatically with changing angle. The angles given in the figure are between the magnetic field vector and the the c-axis vector, with the current direction always kept perpendicular to the field vector. The dominant linear component emerges above 3 T in the lower angle curves, and is less and less pronounced as the angle is increased, with the highest angle MR curves showing the typical H^2 behavior over nearly the entire field range, but overall almost no change in resistance.

The inset of Fig. 3.2 compares the resistance of another sample from the same batch when rotated with the field kept perpendicular with the direction of current (blue)[2] to the field being rotated into the direction of the current (pink). Both curves show the same cosine behavior with angle, meaning the anisotropy is only with respect to the c-axis. This is indicative of a two dimensional system and not the MR associated with an orbital effect, which would disappear only in the longitudinal ($H \| I$) orientation and not the transverse ($H \perp I$) orientation. The minor discrepancies in the resistances of the two orientations shown in th inset could possibly be due to reaction of the sample with air, given that it needed to be removed from the PPMS system completely to change the orientation between the two runs in which the data curves were taken. This, however, does not completely rule out the possibility of a small amount of anisotropy between the a and b axes, but such anisotropy is nowhere near the scale of the apparent anisotropy with respect to the c-axis. The clear two dimensional nature of this linear component is representative of behavior measured in nearly all low n bulk samples produced in this work, yet such behavior is not expected at all, given that studies of thin films show that thickness does not affect the bulk behavior of the material until only a few quintuple layers [112].

Quantum oscillations can also be seen in Fig. 3.2, emerging above 4 T, roughly the same field at which the linear component begins to dominate. Both the frequency of the QO and the slope of the background MR were analyzed, the results of which are shown together vs angle in Fig. 3.3. Details of the QO frequency analysis is

[2]This is the same configuration as the data shown in the main figure.

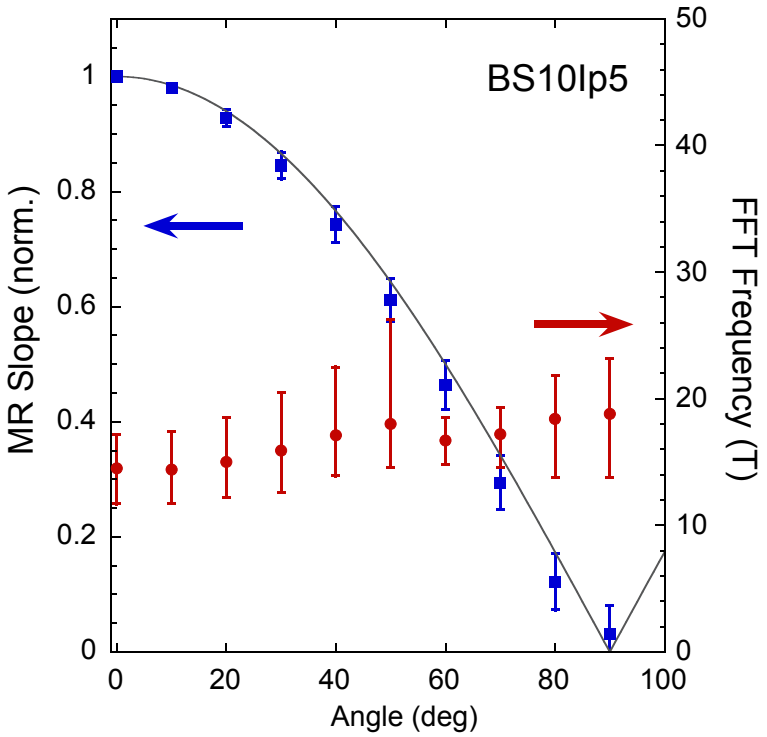

Figure 3.3: The size of the LMR, normalized to the 0^o value, and the SdH frequency measured in the curves shown in Fig. 3.2. The graph contrasts how the slope of those curves changes with angle — following a cosine behavior almost exactly — with how the SdH frequency of the curves changes by only a small amount with angle.

detailed in section 2.2.1.3 and the method used of obtaining the linear component was to do a linear fit, by eye, of the 1st derivative of the MR above 4 T and record the y-intercept value. Error values in the slope come from uncertainty in the accuracy of the linear fit. The frequency of the oscillations ranged from a minimum of 15 T with the field parallel to the c-axis to a 19 T maximum with the field in plane, generally following the slight anisotropy reported in the literature [90]. The 3D nature of the oscillations contrasts starkly with the fact that the linear component of the magnetoresistance seems only to scale with $B_{\perp}$. It therefore is likely that the linear background of the magnetoresistance comes from some effect related to the surface. Whether it is due at all to the topologically protected surface states is unclear. More studies of the contrasting behavior of the LMR to the QO would help better determine if the LMR is truly a surface effect.

3.2 Evolution of Properties in Air vs Vacuum

As mentioned in section 1.1.3, ARPES and thin film studies have shown that the surface of Bi_2Se_3 is extremely sensitive to outside environmental conditions (especially air), however, no experiments have been done to determine the size of this sensitivity on bulk samples. With this in mind, the magnetoresistance of samples was also measured periodically after exposing them to air and subsequently vacuum. If the LMR is linked to 2D states at the surface, then as the surface of a sample changes due to air exposure the LMR should show some kind of change as well. Furthermore, examining what changes may or may not occur in the Hall effect

and QO measured would indicate if the changes at the surface are large enough to affect the bulk of the samples.

Measurements were taken on samples after different total amounts of exposure to air, with all experimental details (contacts, sample geometry, etc.) left undisturbed. Figures 3.4 and 3.5 shows the behavior of the 0^o and 90^o magnetoresistance, respectively, in a representative sample — selected from the same batch as the samples discussed in the previous section — over time. The LMR is the strongest in the first measurement, when the sample has spent less than one hour exposed to air. The size of the LMR then monotonically decreases – roughly 50% after 4 days – with increased exposure to air. The 90^o MR (shown in Fig. 3.5) also shifts downward, beginning as positive MR and crossing over to fully negative MR after just two days. The downward shift, however, is not due solely to a change in the linear component, as it is with the 0^o MR.

Given the reports of such effects like surface reconstruction and reaction with air, some macroscopic change was expected. What was unexpected, however, was that this trend was completely reversed after storing the sample in vacuum for 5 days. The black curve in Fig. 3.4 shows an even stronger LMR than the curve of the first data taken (red), when the sample had been exposed to air for the least amount of time.

Just as with the data in Fig. 3.2, SdH oscillations were resolved in these measurements as well. Remarkably, the frequency of the 0 degree and 90 degree oscillations did not change at all with increase air exposure. After storage in vacuum, however, the MR is much noisier, to the point where QO cannot be resolved in the

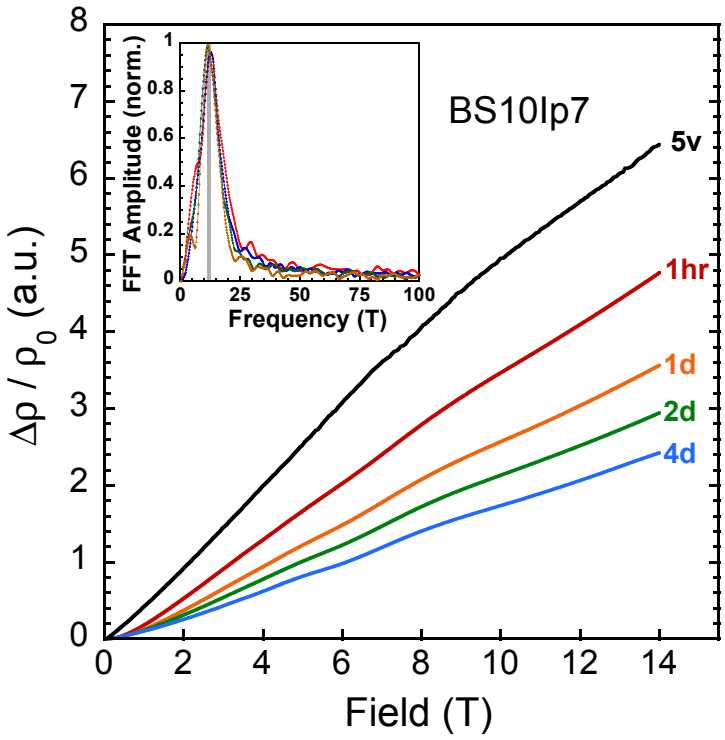

Figure 3.4: Magnetoresistance of a sample of undoped Bi_2Se_3 taken after various durations in air or vacuum. The inset shows the FFT of of the oscillations resolved from the main plot. While the slope of the MR is reduced significantly with added exposure to air, the frequency (peak) of the quantum oscillations does not change at all with time. After subsequent storage in vacuum, the slope of the MR returns to an even higher value.

0^o data. QO can be seen, however in the 90^o MR data (Fig. 3.5) taken after storage in vacuum, the Frequency of which is 24 T — an increase of roughly 24%[3].

Just as with the results of the angular study, there is a clear contrast between the behavior of the LMR and the SdH oscillations over time. Whatever change occurs on the surface due to interactions with air clearly affects the magnetoresistance, yet not the bulk of the sample at all, otherwise it should have been reflected in the

[3]Seriously. I can't believe the coincidence either!

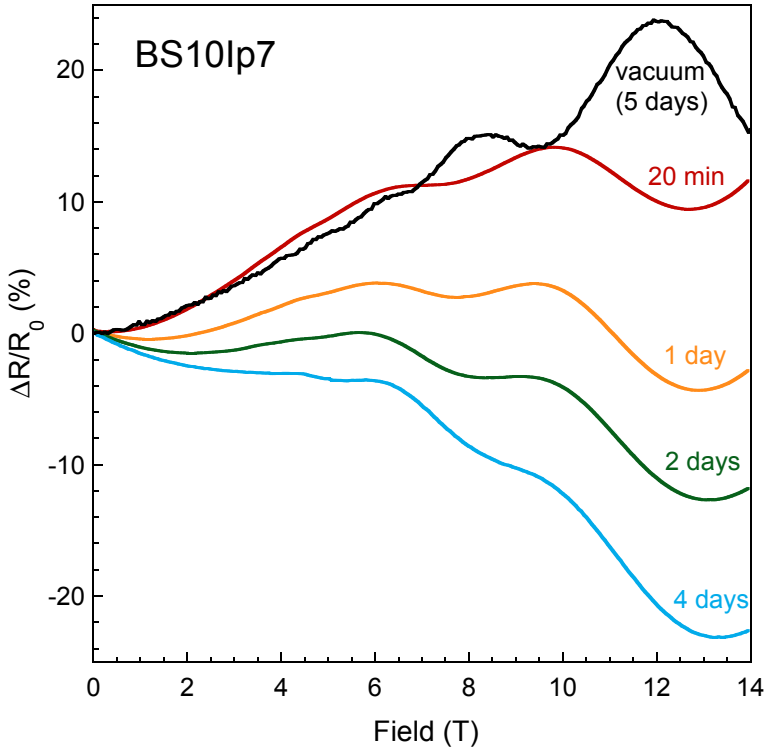

Figure 3.5: Magnetoresistance with H$\|ab$-plane of a sample of undoped Bi_2Se_3 taken after various durations in air or vacuum. It is apparent that the quantum oscillations do not change with time, however the background MR, which follows a classical H^2 behavior, becomes more and more negative over time.

characteristics of the oscillations.

Given its two dimensional nature as well as its sensitivity to air, it is likely that the linear part of the magnetoresistance measured in ultra pure Bi_2Se_3 arises from the surface of the material. The fact that the behavior of other bulk characteristics, such as SdH oscillations and the Hall Effect, contrastingly show typical 3-D behavior and no air sensitivity serve to support this conclusion, since any significant change in the bulk of the sample should be reflected in such characteristics.

Why some bulk phenomena are clearly visible, but the bulk does not also dominate the magnetoresistance behavior is puzzling. It would be expected that the bulk conduction would dwarf the surface conduction. Unless the bulk magnetoresistance were significantly more resistive than the surface, the conduction channels would have no impetus to prefer the surface to the bulk.

The cause of LMR that is strongly 2-D in nature in a bulk material with a 3-D electronic structure does not seem readily available in the literature. The samples clearly show a small closed Fermi surface, which does not fit Kapitza's explanation [100, 101]. Furthermore, the materials are highly pure single crystals, so homogeneity and polycrystalline effects are not likely [105, 106]. Abrikosov's theory of quantum LMR requires that the electrons be forced into the lowest Landau level, which could only be the case for the lowest doped samples of this study and while the theory proposed by Wang and Lei [109] attributes LMR to the surface states, it assumes that the role of bulk carriers is negligible, which again is clearly not the case.

3.3 High Field Measurements

Regardless of metallic vs nonmetallic behavior, the growth techniques developed in this work reliably produced samples with some of the lowest n ever reported in undoped Bi_2Se_3. These samples of such low n provided the ability to push their bulk Fermi surfaces deep into the quantum limit with easily achievable magnetic fields. Multiple samples were measured on different occasions at fields up to and above 50 T at pulsed field facilities in Toulouse and Los Alamos. The MR of samples was measured at various angles, just as in the previous section, as well as various temperatures. The short nature of the projects did not allow any exposure studies to be done. The LMR in all samples measured showed the same 2D behavior, as well as no clear signs of saturating, even up to the highest fields. QO were also measured at high fields in some samples, emerging after the bulk states had clearly been forced into the lowest LL. This section shows the results of these high field studies and discusses the behavior of both the LMR at high fields, as well as the high field QO, and their possible origin.

Figure 3.6 shows the angular behavior of ρ_{xx} and its first derivative in fields up to 55 T of a low n sample of Bi_2Se_3, grown in excess Se under high pressure. The angles given in the figure are between the directions of magnetic field and the c-axis of the crystal. Just as in the previous section, the strong anisotropy of the LMR can be readily seen over the extremely large field range of 4 – 55 T. The emergence of negative magnetoresistance can also be seen as H comes close to being parallel with the ab-plane (75^o, 81^o, and 90^o sweeps), indicating that the classical squared

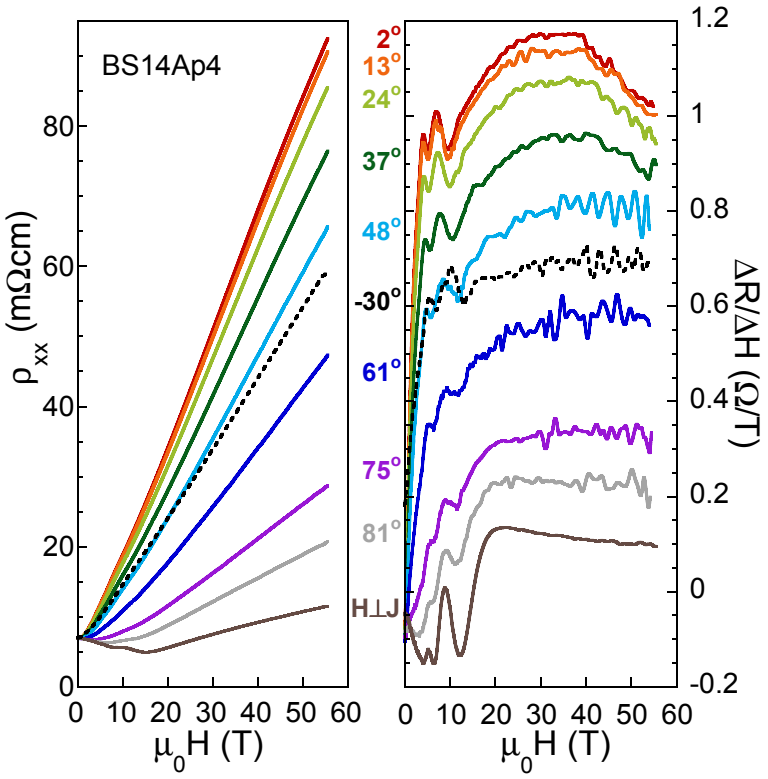

Figure 3.6: Plots of MR (left) and $\delta R/\delta H$ at various angles. The clear linear nature and anisotropy of the background MR is apparent in the left plot and the relative isotropy of the QO can be seen in the right plot. For fields above the QO, the background MR still shows strong anisotropy, but at orientations near $H \parallel c$-axis, a significant nonlinear component emerges.

magnetoresistance is also highly variable amongst samples.

Pulses were done in opposite field directions at multiple orientations, including 90^o, and asymmetry[4] was determined not to be the cause of the negative MR at low fields and high angles. Given the evolution of the 90^o MR data towards increasingly negative MR with increased air exposure, shown in the previous section, this could be an indication that the surface of the sample had already reacted significantly with the atmosphere during the preparation process. This is a likely possibility, as the preparation process in Toulouse took more than an hour and there was no humidity control in the preparation room.

SdH oscillations become apparent in the first derivative, as do even more details of the background LMR at higher fields, once the sample has been pushed into the quantum limit. The background MR over the field range in which the QO are strongest, is quite linear. Above 15 T the oscillations end, yet at low angles the background MR in the high field regime is not purely linear or quadratic. This shoulder could indicate a broad transition towards saturating behavior, yet it too disappears at lower angles, and the LMR remains as the dominant contribution at high fields, even when the field is parallel to the ab-plane. Large fluctuations in some curves at the highest fields, apparent in the right graph of Fig. 3.6, may initially seem like signatures of more QO, however they are not reproduced over multiple curves, nor are they periodic in inverse field.

Figure 3.7 shows the MR and first derivative up to 58 T of another sample of Bi_2Se_3, labelled VGPSAx1 but it shall be called sample L in this discussion, for

[4]Asymmetry in R_{xx} data is commonly due to a large Hall signal.

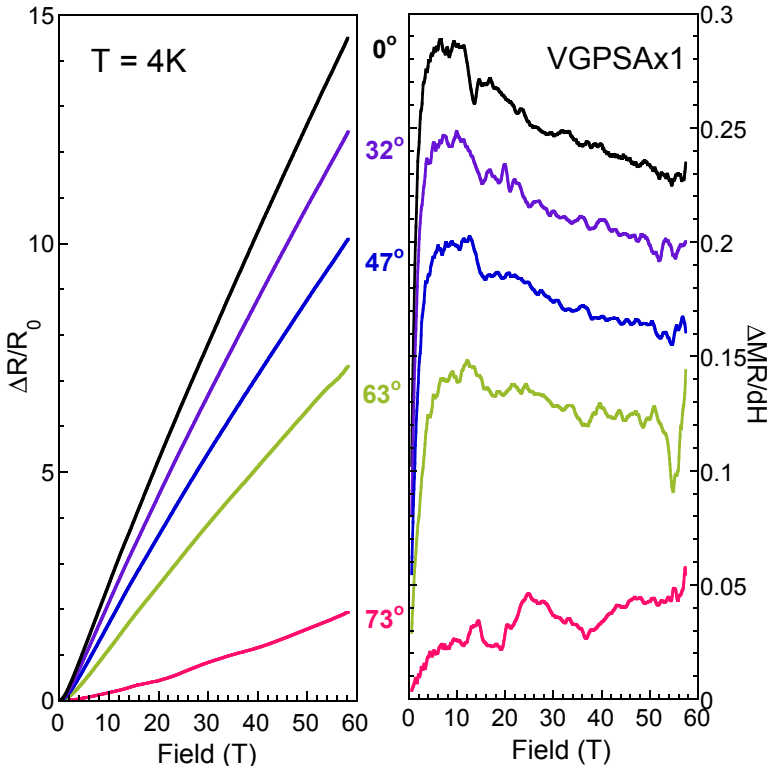

Figure 3.7: Plots of MR (left) and $\delta R/\delta H$ at various angles of another sample of Bi_2Se_3 . Like the previous figure, this sample shows a strong anisotropic linear MR. QO are more difficult in this sample, but the MR above 5 T is almost purely linear the background.

clarity purposes. Sample L was grown using the modified Bridgeman furnace (mentioned in section 2.1.2 in excess Se and measurements were taken at the National High Magnetic Field laboratory in Los Alamos, NM, by Dr. Nicholas Butch. Not only does sample L show no sign of oscillations until roughly 9 T, but its MR at high fields is much more linear than the first sample, as evidenced in the first derivative data (left plot in Fig. 3.7). It is possible to resolve QO in the curves of this sample, yet the frequencies are unexpectedly high, ranging from just over 24 T (at 0^o) to 32 T(at 17^o). The unusually high frequency and field at which the QO emerge in a sample from a low n batch, that otherwise shows the characteristics of having a low concentration, could be because the oscillations come from the surface states.

The fact that the oscillations in sample L can still be seen at very high angles (c axis nearly perpendicular to H) and do not scale with the cosine of the angle is, however, in contrast with results reported for Bi_2Se_3 [40, 113] and even Bi_2Te_3 [114] by other groups who conclude that the 2-D surface states should show behavior that only depends on the component of the field perpendicular to the a-b plane in these materials. An SdH signal that does not vanish when $\mathbf{H} \perp \mathbf{c}$ would seem to indicate that the Fermi surface is three dimensional, in direct contrast to the 2-D nature of the surface states. However, the sample being measured is a bulk sample ($\approx 25\mu$m), which has more than just two macroscopic surfaces that can transport current. Given the ellipsoidal nature of the bulk fermi surface of Bi_2Se_3 , one would expect a dirac cone to exist on the surfaces perpendicular to the ab-plane, with characteristics only slightly different from the surface states that exist in the ab plane. It is possible, given the experimental setup that the current travels along all

four surfaces.

Furthermore, recent theoretical work has shown that the response from a single surface state may not be entirely 2D and may exhibit changing characteristics with changing angle between the field and the surface [115]. The unusual QO in sample L could come from the surface states, but since they are the only set of oscillations in the sample and they appear at all angles, from this data alone the possibility cannot be ruled out that they are bulk.

Another pressure grown sample, named BS11Bpb but called sample T for this discussion, was measured at high fields at the European Magnetic Field Laboratory in Toulouse, FR. The data from sample T provides further information that indicates that the high field oscillations measured in sample L are actually from the surface. Fig. 3.8 shows the longitudinal MR of sample L, compared with that of sample T and another pressure grown sample (label: BS10Lp1) measured at CNAM, with slightly higher n is also shown, for comparison, called sample U. All data shown in Fig. 3.8 was measured below 5K with $\mathbf{H} \parallel \mathbf{c}$. Samples U and T have progressively lower carrier concentrations, both of which are higher than sample L which is assumed to be in the "bulk quantum limit" at relatively low fields ($\approx$ 5 T). The higher doped samples show something other than the purely linear behavior of sample L at lower fields, but once Sample T has reached the quantum limit, its magnetoresistance takes on a linear behavior as well, even parallel with that of sample L.

After a background subtraction, oscillations periodic in $1/B$ are compared shown in Fig. 3.9. The oscillations seen in sample U begin around 3 T and have a period of approximately 17 T, corresponding to $n = 4.0 \times 10^{17}$, which agrees with

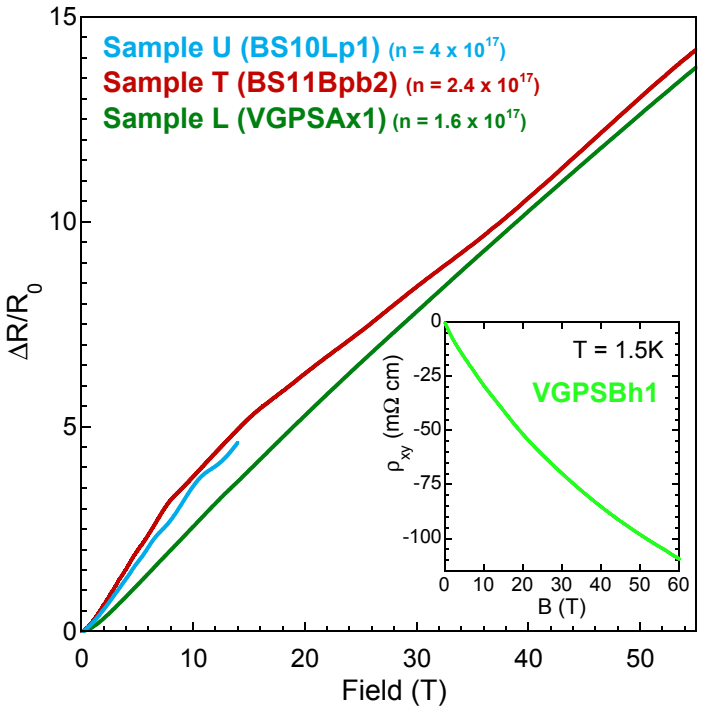

Figure 3.8: MR of samples of Bi_2Se_3 in fields up to 55 T with their estimated carrier concentrations listed. All samples show strongly linear MR down to roughly 5 T with no signs of saturation. The inset shows Hall effect data of a similar sample measured up to 58 T, showing nonlinear behavior.

Hall effect data and is therefore the expected bulk carrier concentration for that sample. With the lower doped sample T, oscillations also emerge at an expected field range with a frequency of approximately 12 T and grow in amplitude until 15 T. Such characteristics of these low field QO are typical of the bulk response of Bi_2Se_3 that has been previously reported.

Above 15 T the background MR changes slope slightly, and above 18 T more oscillations emerge. These high field QO are much smaller in amplitude and have a frequency ($\approx$ 70 T) that is very different from not only the low field QO, but also any higher harmonics. The possibility of Fractional Quantum Hall states from the bulk fermi surface can be ruled out because the prominent fractional states (1/3, 2/5, etc.) corresponding to the frequency of the low field oscillations do not match up with the minima of the higher field QO. The high field QO are also not due to vibrations or a mechanical artifact, since they remain unchanged over multiple measurements at the same temperature and can be seen at multiple temperatures up to 20K. The chief effect on oscillations from electrons in the bulk conduction band would normally be spin splitting, as addressed by Schoenberg [116], which would cause a corresponding split of the QO into multiple frequencies at higher field. Yet this frequency splitting is completely absent in the high field measurements. Instead, in sample T, one set of oscillations emerges and disappears, and only after the lower field oscillations are gone does the second set of oscillations emerge.

The temperature dependence of the oscillation amplitudes from QO in samples L, T, and U were analyzed using Eq. 2.15 and the fits are shown in Fig. 3.10. The low field oscillations in sample T ($\geq$ 0.06 T^{-1}) have an effective mass $m_* \approx 0.15$

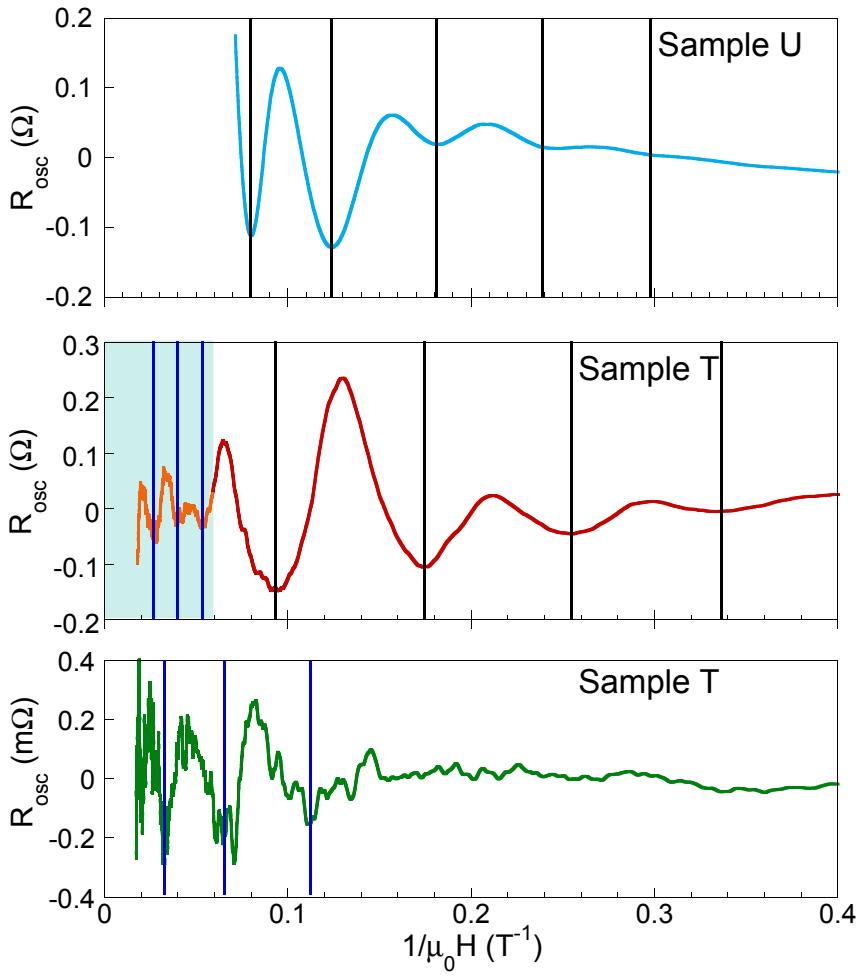

Figure 3.9: Plots of SdH oscillations resolved in the MR curved shown in Fig. 3.8. Sample U shows clear oscillations of a low frequency at low fields. Sample T also shows low frequency oscillations over a similar field range, but the low field oscillations end at 12 T and a different set of oscillations with a much higher frequency emerge above 16 T.

Table 3.1: parameters for the fits shown in Fig.s 3.10 and 3.11

Sample	F (T)	m_*	g_s	v_f (x 10^5)	γ
T-low	11.8	0.145	34	3.25	0
T-high	67.2	0.28 ± 0.04	28	3.25	π
L	24.5	0.24 ± 0.03	28	3.5	π
U	16.8	0.15 ± 0.005	36	3.0	0

m_e, which matches the behavior already ascribed to bulk states in Bi_2Se_3 [67]. The absolute amplitudes of the high field QO were more difficult to resolve in both samples. In both cases, however, a prediction of 0.15 as an effective mass is clearly too low, with the best fits placing m_* to be ≈ 0.24 and 0.27 m_e for samples L and T, respectively. The effective masses for all sets of oscillations are included in Table 3.1 This analysis confirms that the high and low field oscillations in sample T come from different origins, yet it is not direct evidence that the high field oscillations are from the surface states.

Assuming the effective masses given in Table 3.1, the best fits of the field dependence (using Eq. 2.14) give a Dingle temperature of ≈ 35 K for the high field QO and ≈ 7 K ± 0.4 K for the low fiels QO. This would correspond to a surface mobility of ≈ 350 cm^2/Vs and a bulk mobility of $\approx$ 2,000 cm^2/Vs.

Looking again at the oscillations in sample L, they seem to have more in common with the high field QO of sample T, than the bulk QO of sample U. The strong LMR and QO do not match the behavior reported in other samples with carrier concentration near 7.0x10^{17} which already appear at much lower fields [41]. Furthermore the effective mass of the QO is more like that of the high field QO in sample T, than typical bulk QO, like those measured in sample U.

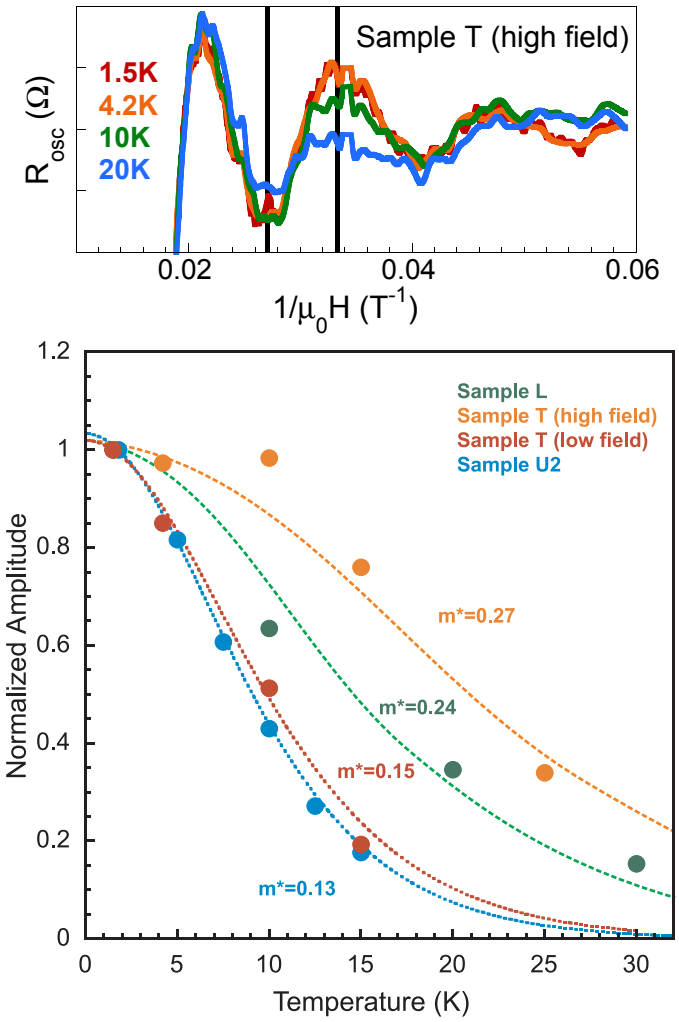

Figure 3.10: Plots showing the temperature dependence in SdH amplitudes. The top plot shows the high field QO in sample T at various temperatures as an example of how the amplitudes were analyzed. In this case, an extremum was chosen and the amplitude of each curve at that field value was taken and normalized to the lowest temperature amplitude. The bottom plot shows the fits to the temperature dependence using the standard Lifshitz-Kosevich formulism. The results of the fits shown in the bottom plot (solid lines) provide estimates of m_* for each of the samples, which are listed. The low field QO have effective masses that match the bulk conduction band of Bi_2Se_3 , however the high field QO have significantly higher values of m_*. It should be noted that the higher field value at which the high field QO were evaluated causes them to have a weaker temperature dependence than the low field QO, despite exhibiting a larger effective mass.

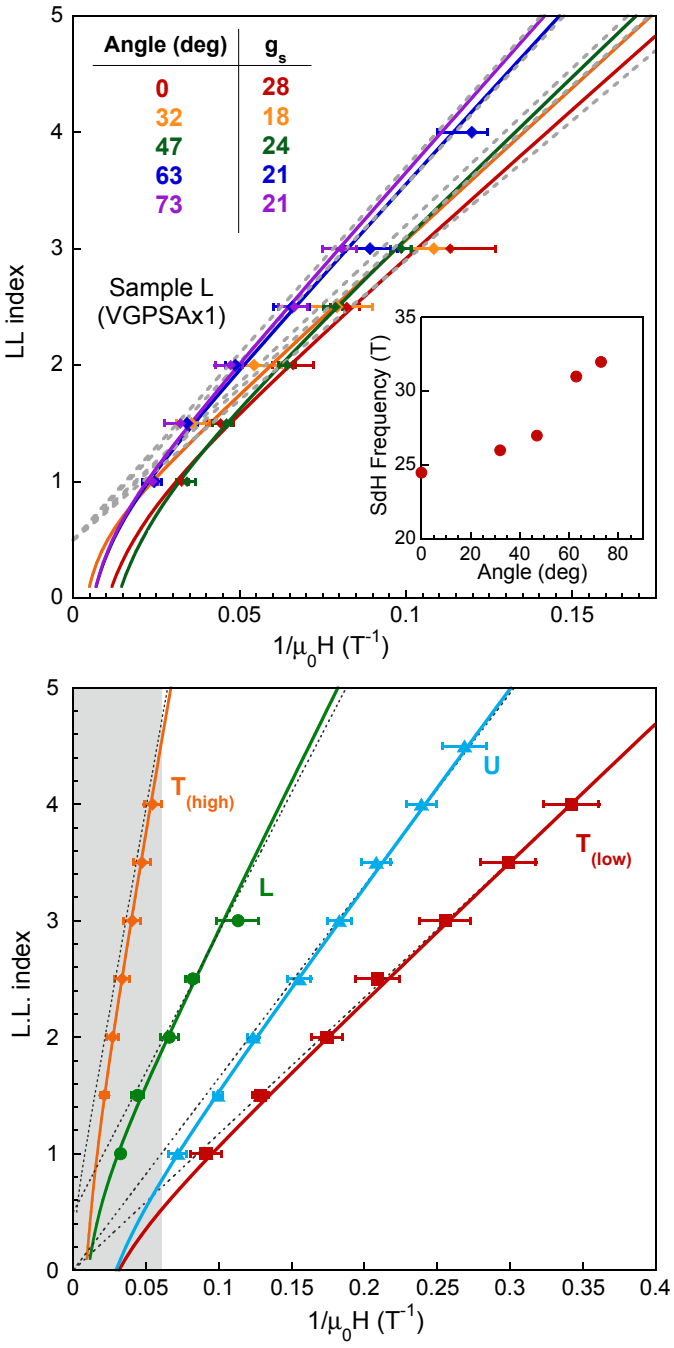

Figure 3.11: LL index plots of the QO shown in Fig. 3.9. The top plot compares the LL indices of the QO from samples L and U, as well as both sets of QO from sample T. The plots include linear fits (dotted lines) as well as fits taking into account phase shifting from SOC (solid lines). The fits estimate the Berry's phase for the low and high field QO to be zero and π, respectively. This characterizes the low field QO as coming from the bulk and the high field QO as coming from the surface.

Fig. 3.11 shows the results of an analysis of the LL index of all sets of QO in samples U and T, as well as the 0^o oscillations in sample L, with the parameters used listed in Table 3.1. The extrema of the high field QO in sample T were indexed separately from the low field QO and, in final analysis, the inherent Berry's phase of the states was determined using the LL bending model. As can be seen in Fig. 3.11, the fits match the data remarkably well.

The low field oscillations in samples U and T have an intrinsic γ of zero and the high field oscillations in sample T as well as the those measured at every orientation in sample L have an intrinsic γ of π. Furthermore, as can be seen in both Fig. 3.11 and Table 3.1, only the Zeeman coupling g_s and the SdH frequency change with respect to the angle in sample L. Given the slight anisotropy of the Fermi surface of Bi_2Se_3 , as well as the directional nature of g_s, these changes are not unexpected. As for the parameters from 0^o measurements compared across samples, the SdH frequency and m_* are expected to change depending on the location of E_F, given that the curvature of the Bi_2Se_3 conduction band changes as one moves away from the gamma point, thus making them sample dependent. Zeeman coupling (g_s), however, should remain sample independent, which it indeed does in the calculations, despite it being allowed to vary in the model. The overall success of modelling the high field oscillations seen in samples T and L provides a compelling case that they are a signature of the surface states in Bi_2Se_3.

Figure 3.12 shows the estimate E_F of both the bulk and surface bands for samples L, T, and U, calculated using Eq. 2.12. The discrepancy in Fermi energy between the surface and the bulk can be attributed to band bending, a common

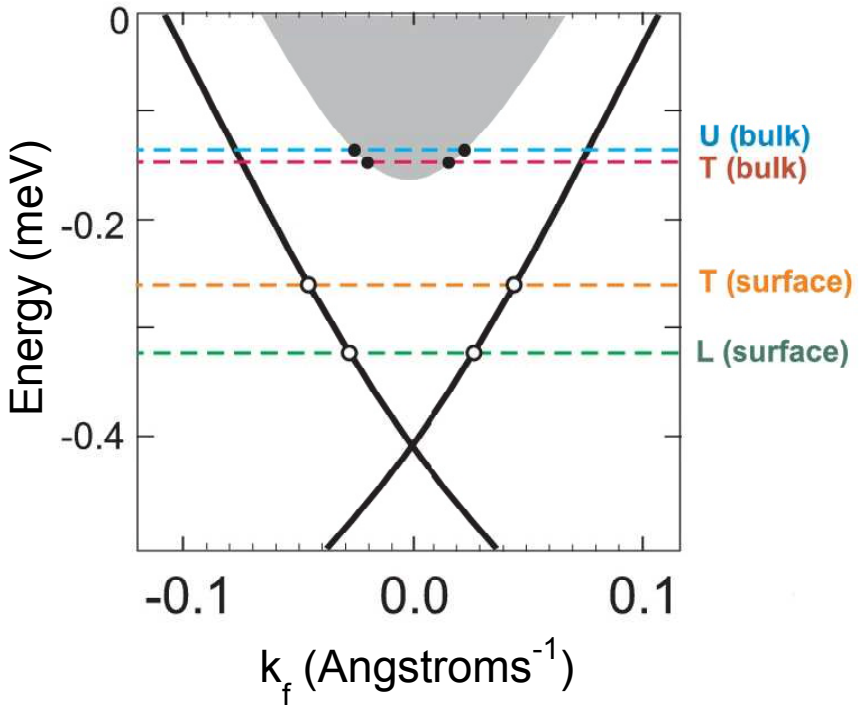

Figure 3.12: A Band Diagram of (taken from ARPES data [22] the energy gap in Bi_2Se_3 , with the SS crossing the gap. The calculated placement of E_f, based on QO frequencies, for samples L, T, and U, with the assumed origin labeled for each E_f. The bulk E_f, when detected in samples, is still pinned to the bottom of the conduction band, while the surface E_f seems to be pushed down into the gap.

occurrence in semimetals, which is in accordance with previously reported findings for Bi_2Se_3 [117] and will be discussed further in the next section. The placement of the Fermi energy in these samples, considering their generally conductive behavior illustrates how the bulk carriers can be almost completely depeleted throughout the material, yet still have a large effect on the overall resistive behavior of the material.

The fact that the modelling produces equally accurate fits for the bulk states,

shifting γ by π to account for the Berry's phase, is initially puzzling. However, upon closer consideration, the theory modeling the SdH index begins with the behavior of an ideal Dirac band, and applies changes to γ due to band curvature and magnetic coupling, eventually arriving at conventional parabolic behavior. In this instance of a nonideal dirac band that is very near the bulk band, the most prominent difference between the two bands is the influence of the Berry's phase on the value of γ. Thus it is not unreasonable that the theory describing the field dependence of quantum oscillations of the surface states would also be accurate in describing the field dependence of oscillations from the bulk states, accounting for the accepted difference in Berry's phase (surface states have phase π and bulk states phase 0).

Furthermore, if the bulk bands are assumed to have typical behavior, a g-factor of this size should cause significant spin splitting of the bulk oscillations, however in our data such splitting is conspicuously absent. This problem was also addressed by our collaborators [118], who found the Zeeman energy to be a multiple (two) of the cyclotron energy, which would cause the effects of the spin splitting not to be seen in QO measurements. Given that the spin splitting could be present without it being directly detected, another explanation for the high field QO in sample T becomes apparent. A similar spin splitting effect due to the strong magnetic field, called Rashba splitting, usually only affects states at the surface of materials, but it has been measured recently in a bulk system [58]. Much like the Rashba split QWS shown in Fig. 1.8 (the orange band in the figure), the bulk conduction band could be similarly split, resulting in inner and outer Rashba split Fermi surfaces. In that case, the low field QO would be from the inner Rashba split surface, and the

higher field QO would be from the outer Rashba split surface. Such behavior of a low field QO that gets pushed into the quantum limit, followed by a second set of QO emerging at a much higher field range is exactly what was observed in another system [58]

Investigating the electrical transport properties of undoped Bi_2Se_3 yields possible signatures from the surface states, even though the transport seems to still be dominated by the bulk. Characterization of the strong LMR in low n samples strongly indicates that it is a manifestation of the 2D surface. The results from measuring the magnetoresistance in samples up to higher magnetic fields reveals the emergence of quantum oscillations not before seen in undoped Bi_2Se_3. A comparison of the two sets of oscillations in the same samples reveals that they come from different origins, which upon further analysis can be attributed to the bulk and topologically distinct surface states. Finally, the theoretical model has been shown to reliably estimate the size of the Zeeman coupling parameter, which can be used in the future to analyze the topological nature of oscillations measured in other candidate TI materials.

Chapter 4: Achieving Nonmetallic Samples: Characterization and Analysis of Unusual Properties

The combined growth techniques of excess Se flux and high pressure growth conditions (details of which are given in sections 2.1.1 and2.1.1.1) were successful in producing samples of undoped Bi_2Se_3 that showed an overall increase in resistivity with decreasing temperature. While such behavior does not fit the exact definition of insulating behavior, as mentioned in section 2.2.1, it is far from the typical metallic behavior commonly reported in bulk samples of undoped Bi_2Se_3.

This section presents measurements performed on three samples that show such nonmetallic behavior. While the resistive behaviors of the three samples ranges quite a bit and is nowhere near truly insulating behavior, they are far from the metallic behavior typically reported in bulk samples of Bi_2Se_3 and are, to date, the only known pure bulk samples to show such strong nonmetallic behavior. Furthermore, the samples show other unusual behavior in Hall effect and MR data, indicative of multiple carrier types. A nonlinear Hall curve clearly identifies two carrier types and allows for the identification of separate bulk and surface state contributions to the conductivity, with the coexistence of positive and negative carriers providing unequivocal proof of TI surface states from transport data alone.

Data on one low-n, semimetallic, and one metallic sample are also shown for comparison. The metallic sample shows two clear SdH oscillation frequencies. The properties of the various samples are compared and the origin of signatures from multiple carrier types is discussed. The evidence points to strong upward band bending at the surface of the samples, pushing E_F to the Dirac point in the middle of the energy gap at the surface, while it remains pinned to the bottom of the conduction band in the bulk. Supporting evidence of this picture is presented, as well as details of extreme surface sensitivity of the samples[1], which prove to be major hindrances for future experimentation.

4.1 Insulating Behavior

The resistivity temperature dependence $\rho(T)$ shown in Fig. 4.1 illustrates the range of non-metallic behavior of three samples of pressure-grown Bi_2Se_3 crystals. Two additional samples, VGPSA2 and BS13A4, are included for comparison. BS13A4, referred to as sample H for brevity in this discussion, shows metallic behavior typical of most samples of Bi_2Se_3 in the literature, while sample VGPSA3, referred to as sample V, shows semi-metallic behavior identical to the lowest carrier concentration samples reported to date [24, 41]. These two samples are an excellent example of the effect growth conditions have on the sample's carrier concentration, with sample V being grown in excess Se in the modified Bridgeman furnace and sample H being grown with the standard flux growth technique from a stoichiometric ratio. Unlike samples V and H, the non-metallic crystals (BS12Ap1,

[1] similar to that presented in the previous section

BS12Dp1, and BS11Fp1, referred to as samples A, D, and F respectively) exhibit an overall increase in resistivity with decreasing temperature. Furthermore, the most insulating-like samples exhibit a room temperature resistivity value far greater than the comparison samples or previous measurements of both pure and chemically substituted samples of Bi_2Se_3 [34, 40, 41], indicating that the insulating behavior originates mainly from a decrease in overall carrier density (as opposed to a strong increase in scattering rate). The presence of a distinct minimum in resistivity near 30 K in all samples follows the concentration-independent trend reported previously [24, 41], and is consistent with a phonon-dependent scattering feature [119] that only changes with lattice density such as induced by external pressure, which readily pushes the minimum up in temperature [46].

Electrical transport measurements were performed on all samples multiple times over a period of months and significant changes in the temperature dependence between measurements were seen, even after only two days for some samples. Such rapid change is a major sign of the volatility of the chemical potential in undoped Bi_2Se_3. Little ($\leq 10\%$) thermal cycling was seen in sample F during measurements, and none in all other samples. Later measurements taken on the nonmetallic samples a few months after the data shown in the main body of the paper did not show any of the non-metallic behavior in any of the samples, exhibiting instead the typical metallic behavior seen in undoped Bi_2Se_3 . The changes in behavior shown in Fig. 4.1 alone illustrate how rapidly the characteristics of this material can change between measurements. While significant changes in sample quality due to exposure to air have been seen [55, 120], this is evidence combined with the data presented in the

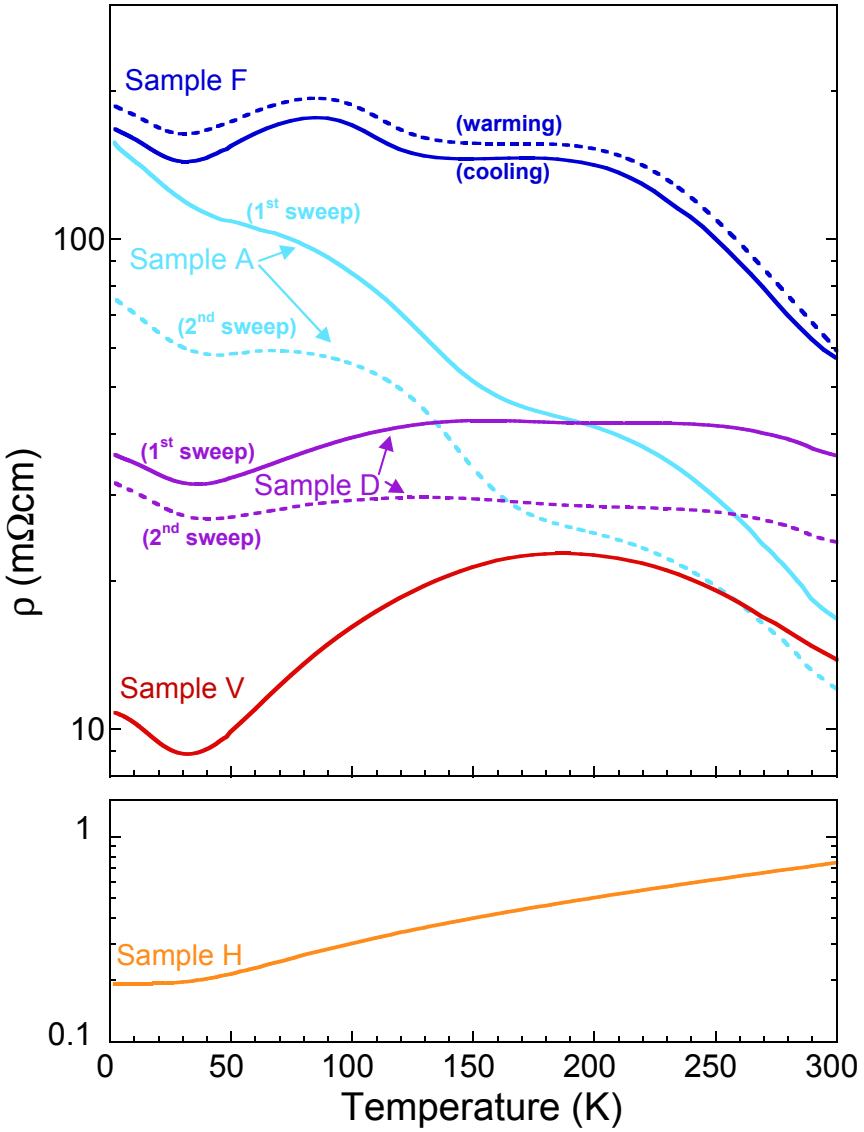

Figure 4.1: Electrical resistivity of stoichiometric Bi_2Se_3 crystals with varying carrier concentrations. Samples A, F, and D all show an overall increase in ρ between 300 K and 2 K. Samples V and H, shown for comparison, have semimetallic and metallic behavior. Dotted curves are of data taken on the same sample at later times.

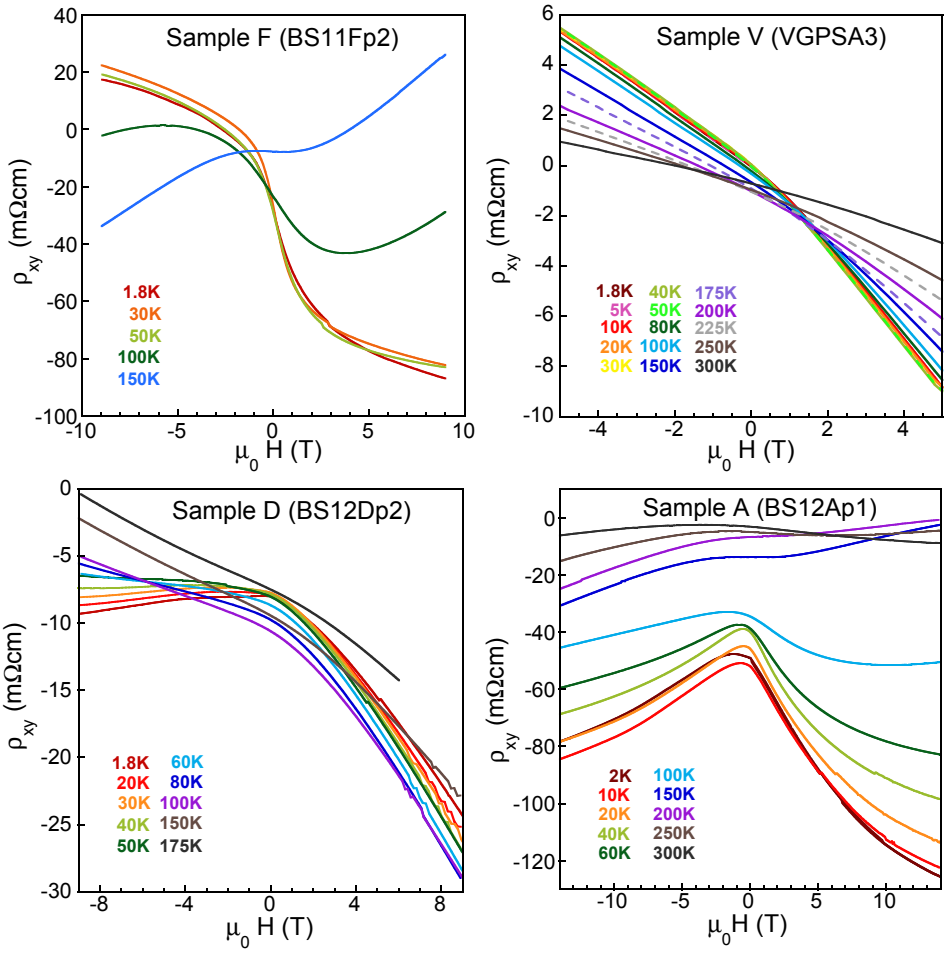

Figure 4.2: Hall resistance vs magnetic field shown for samples A, F, D, and V. Each plot shows all curves taken at different temperatures. The change from negative slope to positive slope can be seen in samples A and F.

previous section show that even storage at room temperatures in vaccuum is not enough to prevent significant changes in sample properties.

4.2 Unusual Hall Effect Behavior

Hall resistance was measured at multiple temperatures in all samples. The Hall resistance vs field data (shown in Fig. 4.2) shows significant nonlinear behavior in the same samples that have non-metallic temperature dependence.

The data was antisymmetrized, to isolate the ρ_{xy} component. Even after antisymmetrization, shown in Fig. 4.3, samples A and F, which have pronounced non-metallic behavior in $\rho(T)$, exhibit much more significant curvature in $\rho_{xy}(H)$ and even a hole-like response as temperature is raised. Sample V, a low-carrier density sample that exhibits semi-metallic behavior (shown in Fig. 4.1) displays a small but pronounced curvature in $\rho_{xy}(H)$ indicative of the presence of more than one type of charge carrier. The curvature of sample V, and sample D as well, is away from the x-axis not towards it, which is counter to the behavior one would expect from a system with holes and electrons. Such strong curvature in the Hall effect, as well as a change in the slope from positive to negative is quite unexpected, especially in light of the well-characterized, simple single-band structure of Bi_2Se_3 [22].

The two-carrier Drude model introduced in section 2.2.1.2 was used to fit the data[121].

$$\rho_{xy} = \frac{{\sigma_h}^2 R_h - {\sigma_e}^2 R_e - {\sigma_h}^2 {\sigma_e}^2 R_h R_e (R_h - R_e) H^2}{(\sigma_h + \sigma_e)^2 + {\sigma_h}^2 {\sigma_e}^2 (R_h - R_e)^2 H^2} H \tag{4.1}$$

With σ and R being the conductivities and Hall coefficients of the contributing carrier types - holes and electrons. Given the nearly isotropic, single band nature

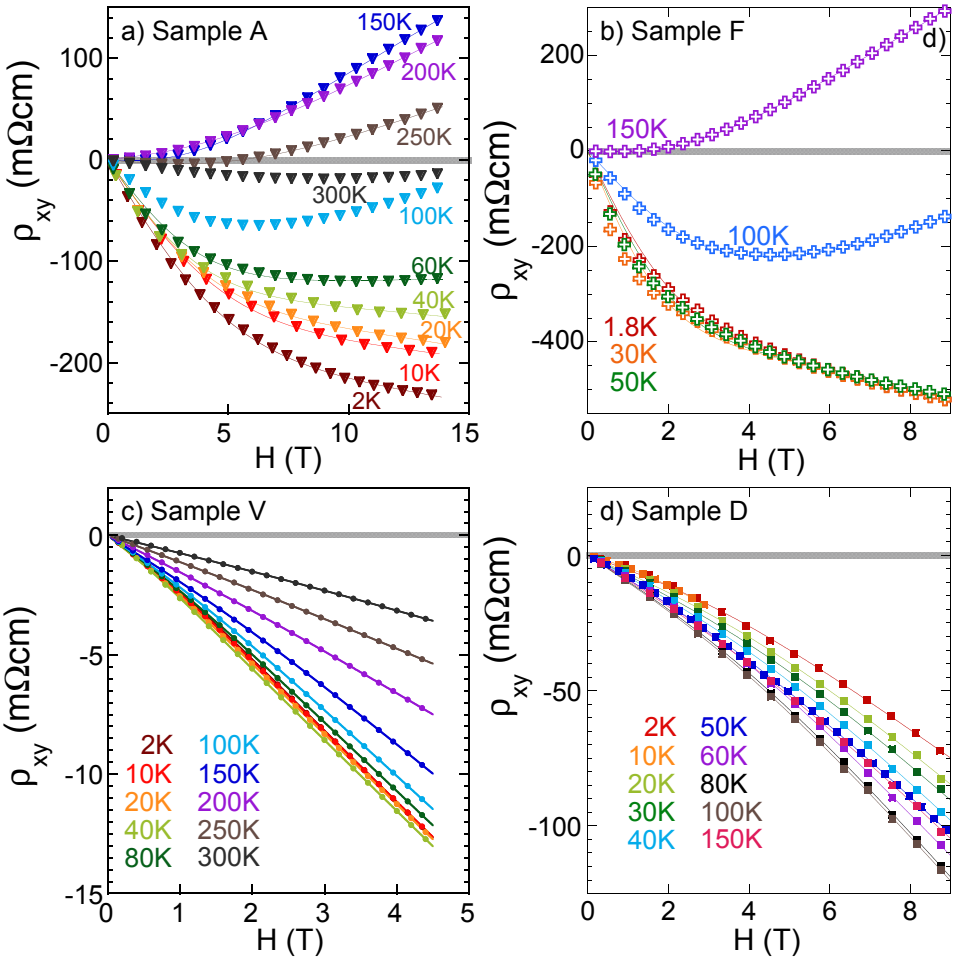

Figure 4.3: Plots of antisymmetrized Hall resistivity of the samples shown in Fig. 4.2 with fits (using the Drude 2 carrier model) included (solid lines). Samples V and D show almost no nonlinear behavior, more commonly seen in Bi_2Se_3 samples. Conversely, samples A and F show the strongest nonlinear behavior, with the Hall coefficient (slope) changing from more negative to less negative with increasing field, and becoming positive at higher temperatures.

of the Fermi surface of Bi_2Se_3 , the following approximations were applied to the model: $R_i = 1/\eta_i e$, $\mu_i = \sigma_i R_i$ with index i being electrons or holes, and η, μ being the carrier concentrations and mobilities, respectively. Using these conversions, an expression of the Drude model is obtained that depends directly on the carrier concentrations and mobilities of the two types of carriers:

$$\rho_{xy} = \frac{{\mu_h}^2 p - {\mu_e}^2 n - {\mu_h}^2 {\mu_e}^2 (p-n) H^2}{(p\mu_h + n\mu_e)^2 + {\mu_h}^2 {\mu_e}^2 (p-n)^2 H^2} \frac{H}{e} \tag{4.2}$$

With n and p being the electron and hole carrier concentrations and e being the electron charge. The details mathematical method used to obtain the values of n, p, μ_e, and μ_h from the curve fits is explained in Appendix A.

An adjusted model assuming two carriers of the same sign (electron-like) was used for samples V and D and two with different sign (one electron- and one hole-like) carriers for sample A, and F. Fits of $\rho_{xy}(H)$ to this model, shown as the solid lines in Fig. 4.4, are in good agreement with the data, especially at higher fields and temperatures. Together with self-consistent fits to low-field longitudinal magnetoresistance, when possible (see section 4.3), a best match was reached for the four physical parameters for the non-metallic samples.

The extracted mobility μ and carrier concentration n values for each carrier type are shown in Figs. 4.4 for comparison. The high mobilities of the minor bands in all samples are what account for their signatures in the Hall curves. The fact that the mobilities of the lower carrier bands are as large as 8,000 cm^2/Vs is in line with the theoretical assumption that topologically protected surface conduction

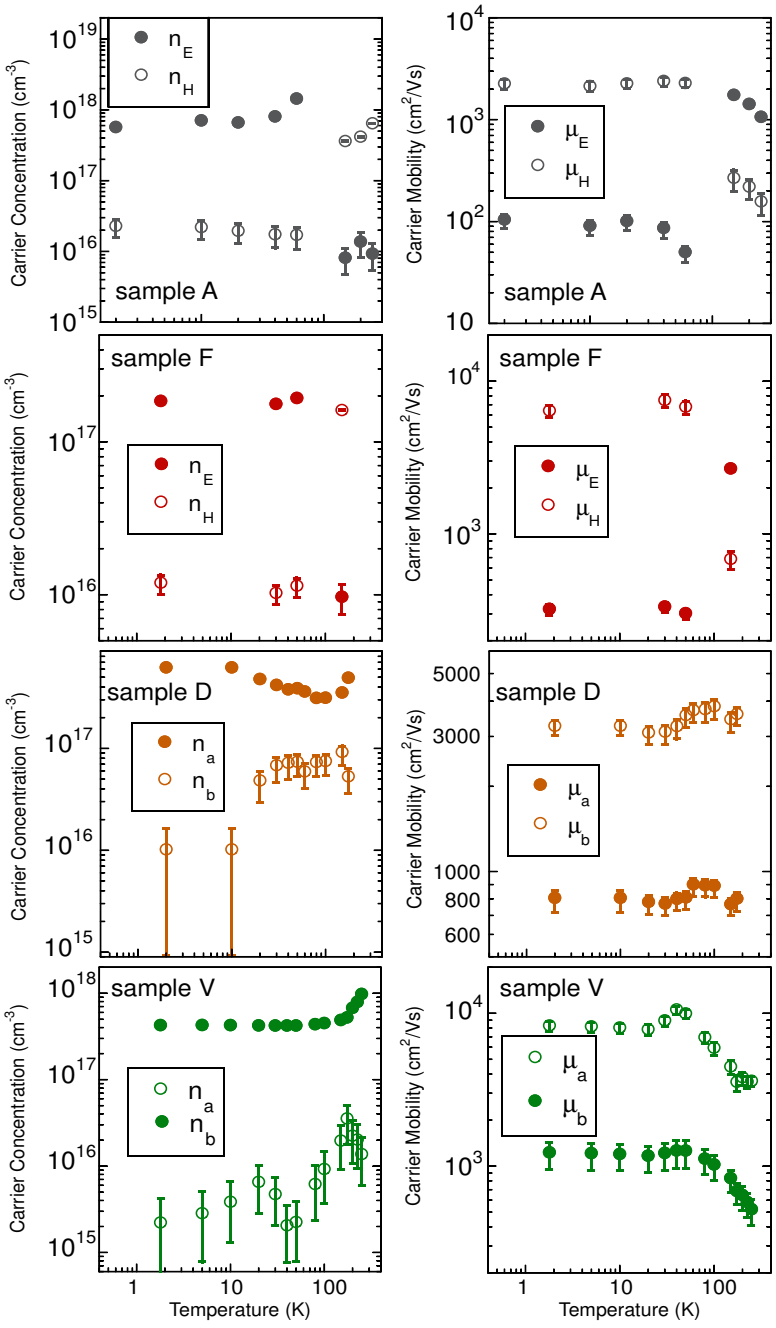

Figure 4.4: Plots of carrier concentration (left) and mobility (right) of charge carriers, plotted on a log-log scale, in samples A, F, D, and V, calculated from fits to the curves shown in Fig. 4.3. While the dominant conduction band concentrations are comparable in all samples (low to mid 10^{17}), the lesser electron concentration in sample V is much lower than that of sample D or the corresponding hole concentrations of samples A and F. The mobilities of the carriers also differs significantly among the samples. The hole mobilities are higher and the electron mobilities lower in sample A than the two electron bands in Sample V, for example.

suffers less from scattering, but yet is very surprising given the extensive efforts to increase mobilities of surface carriers observed in MBE-grown thin-films with atomically sharp epitaxial interfaces [62, 122, 123] as well as the mobilities obtained from the high field QO discussed in section 3.3. Thus, the achievement of more insulating-like behavior in undoped Bi_2Se_3 is not a simple matter of lowering the electron concentration below a certain point, but also lowering the mobility of the bulk electrons.

This idea is further supported by the relative contribution of the minor band to the overall conductivity in each sample. The approximations used in the Drude model, mentioned in Section A.1, were also used to find the conductivities of both carrier types in all of the samples. In the two most insulating samples (A and F), the minor carrier band provides roughly half of the conductivity, whereas in the more semi-metallic samples (D and V) the minor band contributes only a few percent to the overall conduction. Given the consistently high mobilities of the minor bands, the shift away from conduction through it makes sense that the shift away from conduction through the majority band is brought about by lowering its mobility. Exact values of the conductivities of each band, as well as the fractions of total conductivity from the minor bands are listed in Table 4.2, at the end of Section 4.3.

Even more striking is the clear evidence of two carrier types and, moreover, evidence for two carriers with opposite signs in samples A and F. P-type samples of Bi_2Se_3 have been previously reported [24], but the recent extensive set of measurements [22, 50, 56, 57, 117, 124–127] studying the electronic structure of Bi_2Se_3 have verified that its band structure is simplistic and includes only one bulk conduc-

tion and valence band together with Dirac surface states that cross the insulating gap. To reconcile this apparent discrepancy, the most likely origin of the two carrier types is from bulk- and surface-derived bands. For two electron-like carriers (as for sample V), contributions from bulk and surface bands are understandable but one must also consider other causes, such as spin-split bulk bands [56, 57] and trapped quantum well states due to downward band bending at the surface of the crystal [52, 55, 128]. However, the observation of hole-like carriers uniquely rules out such situations and allows for only one explanation: upward band bending.

While the direction of the band bending at the surface of Bi_2Se_3 is almost universally reported to be downward, such studies have been performed either on thin film samples or samples with significantly higher carrier concentrations than the nonmetallic samples being discussed here. Contrastingly, a study done on low carrier concentration samples observes upward band bending [117]. A plausible explanation for this is that the presence of excess selenium in the growth process induces upward band bending at the surface, most likely due to interactions with elemental selenium at the surface, which competes with the effects of adsorbtion and surface relaxation that cause increased downward band bending over time. Assuming upward band bending, with E_F located at the bottom of the bulk conduction band and crossing the Dirac cone at the surface, the band bending in the non-metallic samples is then strong enough that the Fermi level at the surface lies below the Dirac point, producing hole-like behavior in the surface states indicative of ambipolar transport that has previously only been achieved via gating techniques.

Using the estimated carrier concentrations, the Fermi momenta k_F was calcu-

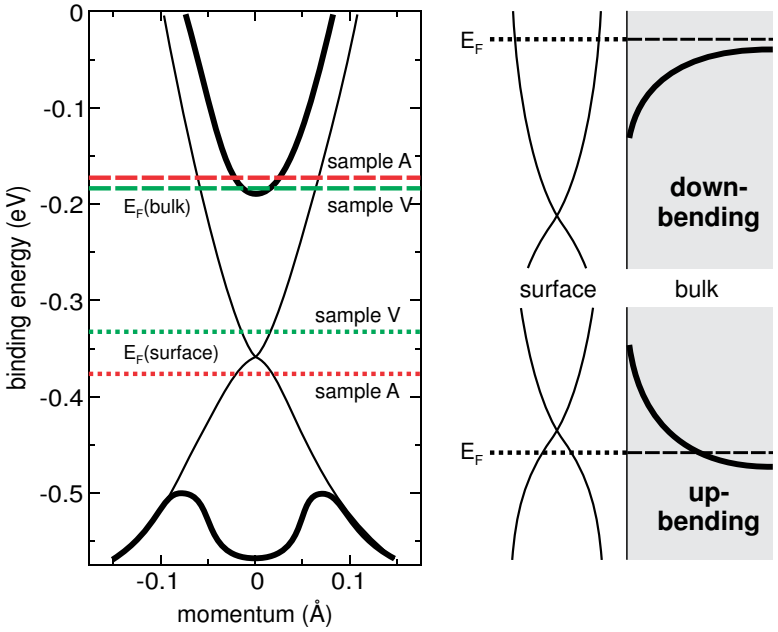

Figure 4.5: A band structure plot showing the locations of bulk and surface E_F in samples A and V, based on calculations from the Hall data. The band structure was taken from ARPES data [55]. The large difference between bulk and surface E_F indicates significant band bending at the surface of the samples, likely due to a much higher concentration of Se near the surface.

lated for each sample using Eq. 2.12. The 3D equation was used in this instance because all carrier concentrations calculated using the Drude model are expressed in cm^{-3}. The resultant diagram showing the placement of Fermi energies with respect to the conduction and valence bands is shown in Fig. 4.5. Any geometric conversions of the concentrations attributed to the surface states would introduce unnecessary uncertainty. Given the orientation of the samples, the k_F of the surface states would be at its maximum value, and therefore the accuracy of the estimates of k_F would not be compromised. The band structure diagram for Bi_2Se_3 – based on ARPES data by Bianchi et. al. [55] – was used to estimate the location of E_F for the surface and bulk states for each sample, given our calculated k_F values and estimated carrier sign.

As expected, the bulk E_Fs for all samples lie at the bottom of the conduction band. From this and previous studies [24, 41] it seems that the bulk E_F remains pinned to either the conduction or valence band and cannot be pushed into the gap for bulk samples by growth techniques alone. The surface E_F for the samples are distributed over a wider range. The nonmetallic samples have E_F values within the range of the Dirac point where charge puddling exists [30], which could act to pin the surface E_F there. The distances between surface and bulk E_F values, shown in Fig. 4.5 indicate band bending of up to 190 meV, with the stronger band bending occuring in the more insulating samples.

The close proximity of the surface E_F for the samples could explain the unusual temperature dependence. Charge puddling in the sample would invariably mean that some sections of the sample surface would be electron-like and others hole-

like and the mobilities of the dominant carriers would depend highly on the local conditions. Therefore, as the samples are cooled down, the relative dominance of the two different types of regions could easily change, manifesting itself in the oft-changing temperature dependence seen.

The specific values of carrier concentrations and mobilities, however striking, are still dependent on the Hall data alone. Other types of experimental data confirming these values would significantly support both the theory of the origin of the behavior in the samples and the validity of the mathematical method[2] used to analyse it.

4.3 Magnetoresistance and QO

In addition to Hall effect data, MR data was taken on the samples. Low-temperature MR measurements, shown in Fig. 4.6 do not show any QO in the non-metallic samples at 2 K, which is usually an indication that the bulk carriers are at a low enough concentration to be in the quantum limit at moderate fields. QO were, however, observed in the MR of samples V and H.

The longitudinal magnetoresistance (MR) of nearly all samples follows the strong, quasi-linear MR seen in previously reported low doped samples [41]. While the magnitude of the MR seems to have no correlation with carrier concentration or insulating behavior, Sample A stands out from the others due to its cusp-like behavior at low fields, and its non-linear behavior at high fields, which is modelled

[2]To our knowledge, this particular mathematical method for fitting the Drude model is not commonly used in the field.

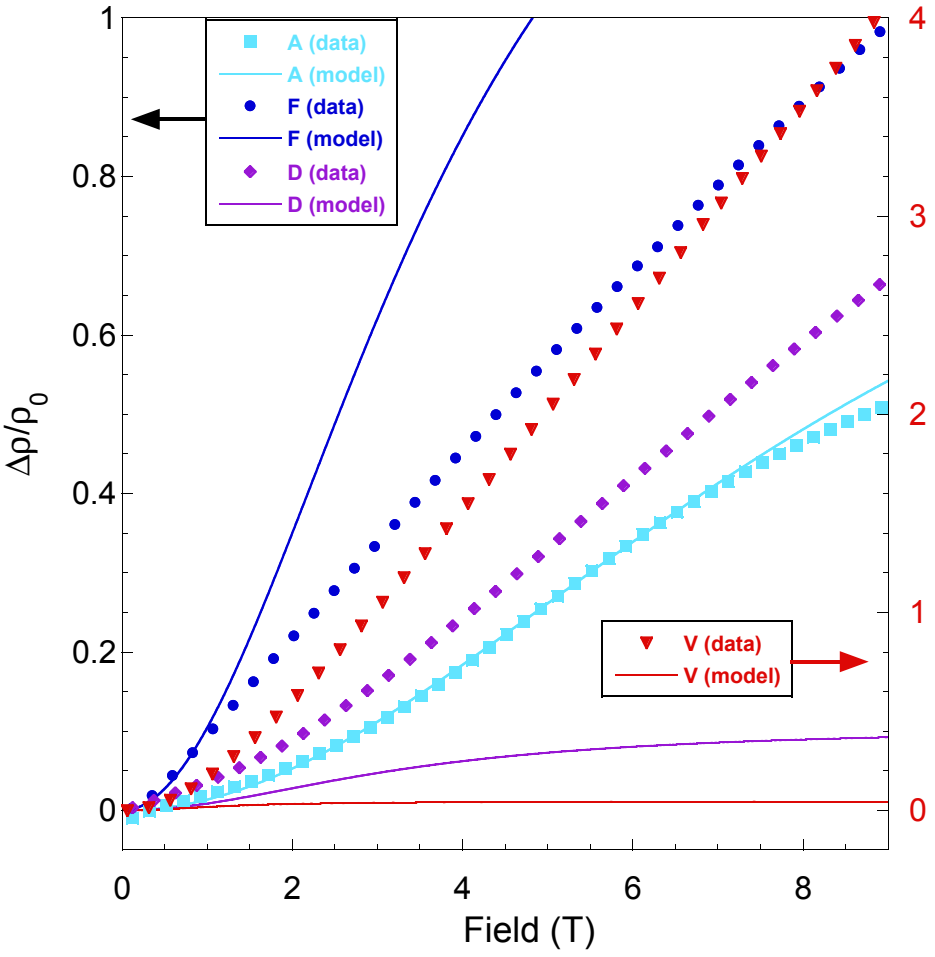

Figure 4.6: Symmetrized MR of the four samples discussed in the previous section (A, F, D, and V), with fits using the Drude 2 carrier model included as solid lines. The MR of sample V is so strong that it is plotted on a different y-axis (shown, in red, on the right). The semi-metallic samples show strongly linear, nonsaturating MR, which does not match the Drude model at all and is commonly seen in low n samples of Bi_2Se_3 . The MR of the non-metallic samples, contrastingly, show the beginning of saturating behavior, and the Drude model fits them over all (sample A) or part (sample F) of the field range. The concentrations and mobilities calculated by the fit for sample A match up well with the values given by fits to the sample's Hall data.

exceptionally well by Eq. 2.16. The extremely low electron mobility of sample A, shown in Fig. 4.4, could account for the lack of oscillations in its magnetoresistance, which should be observable in the field range used, given a carrier concentration $n = 4.3 \times 10^{17}$ cm^3. The low field behavior of sample A resembles the weak antilocalization cusps previously reported in thin films of Bi_2Se_3 [129]. Fits to the expected WAL behavior, however, fail to correctly describe the behavior, as they give values of α that are far too high.

The analysis of the SdH oscillations observable in higher carrier density samples allows for an independent check of the analysis described in Appendix A. Samples V and H both exhibit SdH oscillations (shown in Fig.s 4.7 and 4.8) as expected for moderately doped samples [41], but the latter sample exhibits a rare case of two oscillatory components as clearly seen in the beating modulation presented in Fig. 4.8.

For the QO in sample V, shifting of the lowest Landau levels, due to spin orbit coupling [42] causes a change in the oscillation frequency at the highest fields, as seen in Fig. 4.7b). Early discrepancies between the single frequency model and the data were resolved when adjusting for this LL-shifting (using Eq. 2.18) and modeling of the oscillatory signal (using Eq. 2.16), shown as the solid red line in Fig. 4.7, can accurately fit the data with only one signal. The parameters obtained from the SdH modelling are listed in Table 4.1 for direct comparison with the same parameters obtained from the Drude modelling of the Hall resistivity.

The FFT peak for the QO in sample V was measured to be approximately 18 T, which corresponds to $n \approx 4.3 \times 10^{17}$ cm^{-3}, matching n_b given by the Drude

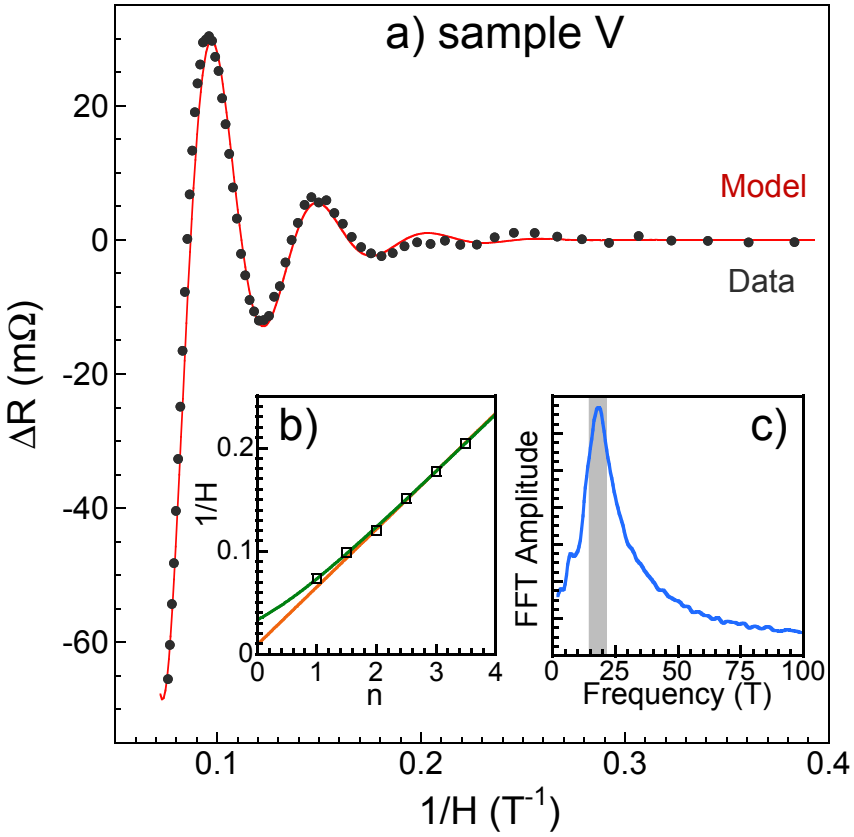

Figure 4.7: Quantum oscillations, plotted vs inverse field, measured in ρ_{xx} of sample V. The solid red line is a fit to the oscillations using a single frequency model, taking SOC phase shifting — shown in the left inset — into account. The right inset shows the Fourier Transform of the oscillations, with a single resonance peak indicating the low-frequency plotted in the main figure. The value of n corresponding to the SdH frequency matches the value given by the Drude model for the dominant conduction band, confirming the validity of the model.

model, The Dingle temperature given by the model fit corresponds to $\mu \approx 900$ cm^2/Vs, which is close to μ_b of the Drude model. Such close agreement between the SdH oscillations and one band of the two carrier model is strong evidence that the analysis technique is accurate, given that the carrier concentration of the other band is already in the quantum limit at low fields.

Despite having a much higher carrier concentration, Sample H is also unique in that it shows QO of two distinct fequencies, shown as the blue markers in the top plot of Fig. 4.8 with the same type of SdH modelling shown as the solid red line. The presence of two oscillatory signals, close in frequency, is easily discernable by the beating node at roughly 0.167 T^{-1}. Futhermore, sample H also shows a small but discernable curvature in its Hall signal, the same type as samples D and V.

The FFT of the sample H oscillations, shown as the insert in Fig. 4.8 confirms two oscillation frequencies of 85 T and 95 T, corresponding to 3D carrier densities of 4.4×10^{18} cm-2 and 5.3×10^{18} cm-2, respectively. This compares perfectly with the concentrations extracted from Drude modelling of Hall data shown in the bottom plot of Fig. 4.8. LL phase shifting was neglected in the case of sample H, because the LL were high enough to make the SOC effects insignificant. The full set of parameters obtained from both models are also listed in Table 4.1.

The analyses of both samples V and H show the expected behavior that the carriers at the surface have a higher mobility than those of the bulk. Surprisingly, sample H shows a higher contribution to the conductivity from the (assumed) surface band than sample V, 16% compared to only 3%. While the surface band mobility calculated for sample H from the Dingle temperature is much lower than that given

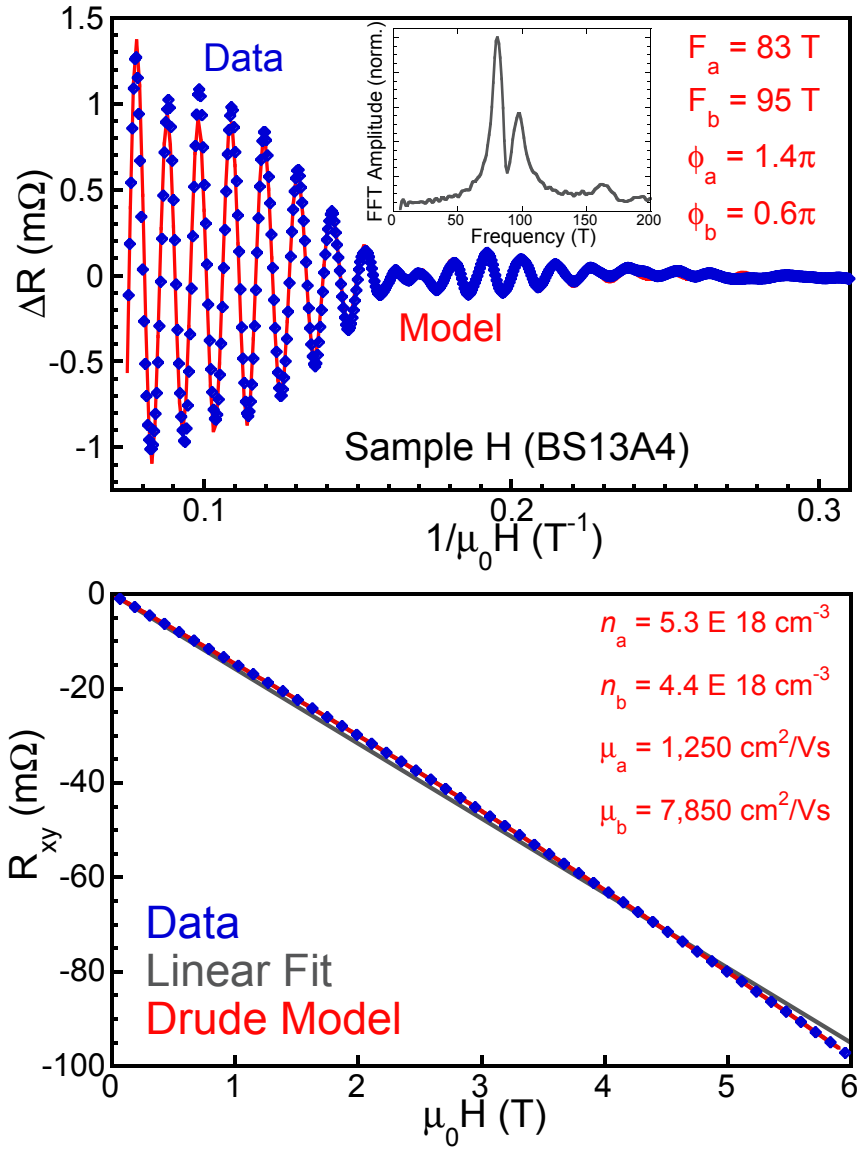

Figure 4.8: a) plots the SdH oscillations vs inverse field measured in a high n sample at 1.8 K. A model of the oscillations (blue) is shown with the data (red). b) plots the Hall resistivity vs field measured in the same sample at the same time as the data shown in the top graph. The model (green) is shown with the data (red).

Table 4.1: Physical Parameters extracted from Hall and SdH data on a high carrier concentration sample of Bi_2Se_3

	Sample H_a	Sample H_b	Sample V
Drude n ($\times 10^{18}$cm^{-3})	4.375	5.3	0.427
Drude μ (cm^2/Vs)	7,850	1,250	1,230
SdH n ($\times 10^{18}$cm^{-3})	4.4	5.3	0.424
SdH μ (cm^2/Vs)	2,660	1,970	1,130
SdH ϕ (rad.)	1.24π	0	0.534π

by the Drude analysis, the mobilities for the bulk band are relatively close in value for both samples H and V. Large discrepancies in estimates of μ between Hall and QO data are not unusual in materials characterization, because in addition to the two sources of damping discussed in section 2.2.1.3, there are other effects that can dampen the QO in a material, which can not be easily modelled.

The close agreement of carrier concentrations, as well as the general agreement of mobilities of our two carrier model with the standard analysis method for the SdH oscillations measured in the same sample further confirms the model's validity. More surprising, Berry's phases calculated by the SdH model for the two oscillatory components that are offset by nearly π from one another, suggesting that the component with a non-trivial Berry's phase is a TI surface state. This is extraordinary, considering that quantum oscillations of surface states in Bi_2Se_3 have so far only been observed in very high (pulsed) magnetic fields, such as the measurements discussed in the previous section and measurements done on doped samples [40], both cases exhibiting greatly reduced carrier mobilities. In our case, the mobility is much enhanced for the component with non-trivial Berry's phase, approaching a value of 7,850 cm^2/Vs that is remarkably similar to the surface carrier

values for sample V above.

The significant enhancements in measured mobilities of TI surface states in stoichiometric Bi_2Se_3 are surprising in comparison to prior extensive work on this material, but perhaps not unfounded given the unique material preparation technique that yields a band bending direction opposite to that commonly observed.

This upward band bending is, however, short lived. The samples that exhibited the non-metallic behavior discussed in this section, in addition to showing the change in $R(T)$ behavior shown in Fig. 4.1, also showed a complete return to metallic behavior, when measured at least two weeks later, being stored the entire time at room temperature in vacuum. Even in the case of sample H, significant changes were seen in the QO measured in the sample after one, two, and seven days stored in air, showing the QO frequencies shifting and one frequency disappearing altogether. The suppression of resistivity values, in particular in the most insulating-like samples that exhibit hole-type behavior, is consistent with a significant downward shift over time in the energy bands at the surface, in agreement with previous studies of the electronic structure evolution at the surface of Bi_2Se_3 [50, 130]. Furthermore, the model of Se buildup at the surface of samples causing upward band bending is supported by findings that the carrier concentrations in samples increase with mechanical exfoliation [30, 120].

Table 4.2: Bulk and surface resistivities extracted from Hall data at or below 2 K on samples of Bi_2Se_3

Sample	Surface σ ($1/\Omega$cm)	Bulk σ ($1/\Omega$cm)	Surf. Contribution (%)
BS11Fp2 (F)	12.32	9.576	56
BS12Ap1 (A)	8.304	9.596	46
BS12Dp2 (D)	5.341	80.55	6
VGPSA3 (V)	2.959	84.01	3
BS13A4 (H)	1,061	5,525	16

4.4 Analysis of Stoichiometry

SEM measurements were performed on all samples, after all transport measurements were done, to determine sample quality. The measurements showed no sign of multiple phases, twinning, or any other large scale defects. Only signatures of Bi and Se were observed. For the lowest carrier concentration samples, the ratios were closest to the expected stoichiometric ratios for Bi_2Se_3, with higher carrier concentrations showing a small deficiency in Se, up to nearly 3%[3], which increased with increased metallic behavior. Fig. 4.9 shows an example SEM image of the surface of one of the nonmetallic samples. The silver paint contacts are clearly visible on the sample and the the areas in between are mostly smooth, showing small lines that may be line defects.

Overall, while true insulating bulk behavior in stoichiometric Bi_2Se_3 remains difficult to achieve, our observations of greatly enhanced mobilities and ambipolar transport without atomically perfect thin films or fabricated gate structures suggests that engineering of electronic band bending near the surface of crystals via

[3]Just at the edge of the minimum margin of error for the SEM.

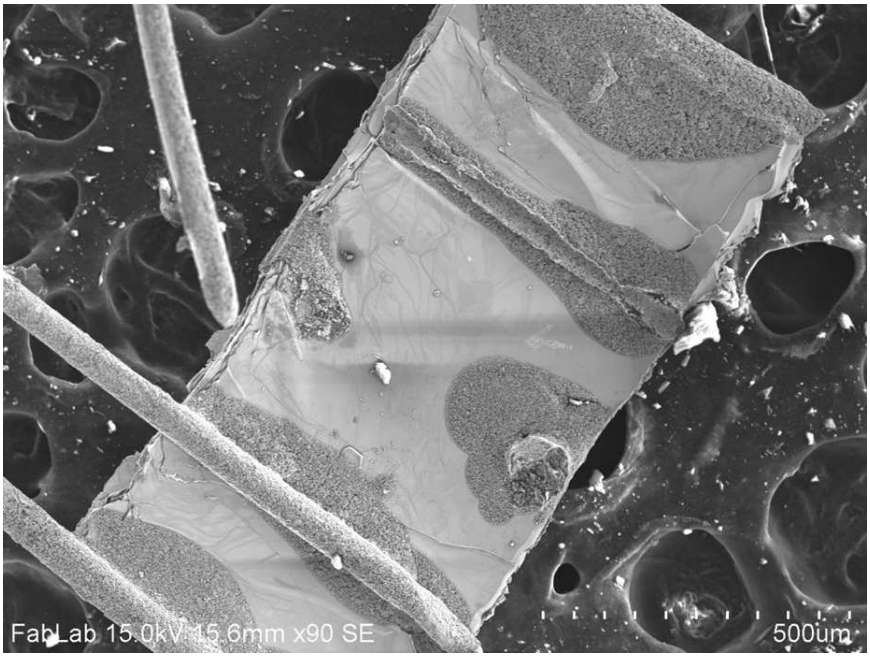

Figure 4.9: SEM image of sample A, after measurements were taken. The rough areas are the silver paint contacts still on the sample. The area between the silver contacts is smooth and blemish free. EDX analysis of multiple spots on the sample confirmed stoichiometric amounts of Bi and Se, with no impurity elements in detectable quantities.

Table 4.3

Sample	Element	Series	Atomic Number	Atomic C (atomic %)	Error (%)
A (BS12Ap1)	Bi	83	M-series	41.93	1.6
	Se	34	L-series	57.15	1.0
	Ag	47	L-series	0.74	0.1
F (BS11Fp2)	Bi	83	M-series	39.83	1.9
	Se	34	L-series	60.17	1.6
D (BS12Dp2)	Bi	83	M-series	40.51	1.6
	Se	34	L-series	59.49	1.3
V (VGPSA3)	Bi	83	M-series	41.66	1.7
	Se	34	L-series	58.34	1.3

new techniques for materials synthesis and preparation promises a new route to optimizing use of the simplest three-dimensional topological insulator.

Chapter 5: Work of Collaborators and Conclusions

Another fruitful result of the efforts to produce low n, semi- and nonmetallic samples of Bi_2Se_3 is that a significant amount of high quality material was produced, which could be given to collaborators to conduct experiments that are not currently possible at CNAM.

DoHun Kim was able to exfoliate semimetallic samples down to thicknesses of only a few QL and use liquid ion gating techniques to push the E_F in the resulting samples through the dirac point, showing ambipolar transport [30] and an intrinsic electron-phonon contribution to the resistivity [131]. Another important result from those investigations was the determination of charge puddling around the Dirac point at the surface, which as metioned before is a likely factor in pinning the surface E_F within the bulk bandgap, in the case of the nonmetallic samples. Furthermore, the thinning of the samples from bulk thicknesses (approx. 100 μm) down to thicknesses used for gating (approx. 10 nm) caused an increase in bulk carrier concentration with each iteration of exfoliation, confirming the very sensitive nature of the chemical potential, as well as supporting the theory of Se accumulation at the surface of the bulk samples grown using the methods discussed.

Thermal transport measurements done by collaborators in Paris showed strong

quantum oscillations in the Nernst effect[118]. The oscillations were analysed and used to investigate further the conspicuous absence of Rashba splitting of the topologically trivial SS. They were able to posit that the chemical potential shifts dramatically with increasing field, causing a resonance at the QO frequency, instead of a splitting into two distinct frequencies.

ARPES measurements performed on both undoped samples of Bi_2Se_3 produced through this work and samples of $Bi_{2-x}Ho_xSe_3$ [132] yielded a wealth of information. The group led by Andrea Damascelli was able to characterize the spin texture of the surface states coupled to QLs deeper into the material [80, 125], as well as characterize the strength of Rashba splitting on the trivial surface states of Bi_2Se_3 [57].

Collaborators in Australia have also worked on capping the surface of Bi_2Se_3 samples [61, 62] to prevent the well known chemical reaction at the surface that occurs when samples are exposed to air and other reactive gasses [49, 50].

Optical measurements looking at Kerr rotation have also been performed [133] as a continuation of previously published work [41]. The Kerr measurements show that the response comes from more than a single bulk band, with the additional signal having a large spectral weight and very light effective mass, which most likely comes from the surface of the sample. Still, the measurements were unable to determine the topological nature of this second band. The measurements of Bi_2Se_3 under pressure, mentioned in section 1.1.3 were also performed at the CNAM in cooperation with Jason Jeffries of Lawrence Livermore National Laboratory [47].

In conclusion, undoped Bi_2Se_3 was produced using the combined techniques

of adding excess elemental Se as a flux and growing the materials in high pressures yielded samples of consistently high quality and low carrier concentration. Many samples produced using these methods showed semimetallic behavior and a few even showed nonmetallic, nearly insulating behavior.

With lowering carrier concentration, the emergence of unusual magnetoresistive behavior was noticed and subsequently investigated. The investigations revealed that the unusually large LMR seen in nearly all low n samples measured is 2D in nature and very sensitive to exposure to air. This behavior is in high contrast to the bulk properties of the samples, determined from the characteristics of QO measured, which proved to be 3D in nature and unresponsive to air exposure over extended periods of time. Another interesting contrast discovered was that storage in vacuum has an effect of reversing the changes in LMR seen from air exposure, while significantly degrading and changing the bulk QO. This is interpreted as a sign that Se remains volatile in bulk Bi_2Se_3 at room temperatures and vacuum conditions. It is therefore recommended that samples of Bi_2Se_3 not be stored in vacuum at room temperatures. Storage should instead be in an inert environment at atmospheric pressures and room temperatures, or at liquid N temperatures.

Future studies are planned for investigating how rapidly the LMR properties change due to air exposure by preparing samples in a completely inert atmosphere, thus controlling initial exposure to less than two minutes. The possible relationship between LMR strength and sample carrier concentration and/or mobility will also be investigated, by measuring and comparing such properties of samples over as wide a range of carrier concentrations as possible.

Of the samples that showed nonmetallic behavior, they also exhibited other unusual magnetoresistive behavior, including in some cases transverse magnetoresistance that unequivocally showed signs of both positive and negative carriers participating in the conduction. Analysis of the unusual transverse MR (Hall effect data) using the Drude 2 carrier model (which involved the application of a mathematical technique possibly heretofore unapplied to the model) revealed that the dominant carrier band, attributed to the bulk, never went below $\approx 5 \times 10^{16}$ and that the signature of a high mobility conduction band, attributed to the surface states, was only made more visible when the mobility of the bulk band was significantly lowered.

The validity of the Drude analysis was checked in multiple ways. The a corresponding equation from the Drude model was used to fit the longitudinal MR and obtain values for n_a, n_b, μ_a, and μ_b for the sample showing the most insulating-like behavior, which were exceedingly similar to the values obtained from the transverse MR fits. The other samples showed longitudinal MR that did not fit the Drude model, but the semimetallic sample and metallic samples, shown for comparison to the nonmetallic samples, exhibited SdH oscillations with properties that matched the n_a, n_b, μ_a, and μ_b values obtained by the Drude fits to transverse MR for those samples, fully confirming the validity of the model.

The unique evidence of hole-like carriers in the two most insulating-like samples is explained by extreme upward band bending at the surface of the samples. While while band bending in this direction is opposite to the band bending commonly found in Bi_2Se_3, there is precident in the literature of upward band bending in low n bulk samples [117]. The likelihood of such strong band bending into the

bulk energy gap is increased when taking into account that the calculated values of surface n fall close enough to the Dirac point to be within the charge puddling regime found by our collaborators [30], which likely functions as a pinning mechanism for E_F, just as defects in the bulk pin the bulk E_F to the bottom of the conduction band. Further study of the strongly nonmetallic behavior is, however, quite difficult, as the extreme changes in surface E_F over time shown in the other studies discussed in the work also plague the nonmetallic samples, and strong downward band bending was observed over time, bringing the measured bulk n up to the range of mid 10^{17} cm^{-3} and erasing any signature of the surface states.

In addition to improving the sample properties of Bi_2Se_3, there is promising work being done on other candidate TI materials. The results of studies performed on SmB_6 that show, through thickness and surface gating dependence studies, the existence of robust surface states uncoupled from the bulk are included in Appendix A. The studies were also able to directly determine the carrier concentration and mobility of the surface states, a first for SmB_6.

The main lessons that can be learned from this work are twofold: first that while samples of undoped Bi_2Se_3 that show nonmetallic behavior can be produced, it is primarily achieved through lowering the mobility of the bulk states; and second that sensitivity of the chemical potential at the surface is extremely high due to surface relaxation and chemical reaction/adsorbtion that desirable sample properties are difficult to maintain over time. Current and future work with collaborators at finding a way to cap the surface of Bi_2Se_3 samples and stop rapid and unpredictable changes in the surface environment takes on even more importance in light of the

findings of this work.

Chapter A: Mathematical Methods

This Appendix will cover the mathematical methods developed for some of the analysis techniques used in this work. They are separated into this appendix, because their details do not directly pertain to the concepts of physics discussed in the main body.

This appendix is separated into two main sections: the first dealing with the analysis of the Drude two-carrier model of Hall effect data, and second dealing with the background subtraction used for isolating QO.

A.1 Drude Model

As stated in section 2.2.1.2, the equation used to model the Hall effect is

$$\rho_{xy} = \frac{{\sigma_1}^2 R_{H,1} - {\sigma_2}^2 R_{H,2} - {\sigma_1}^2{\sigma_2}^2 R_{H,1}R_{H,2}(R_{H,1} - R_{H,2})H^2}{(\sigma_1 + \sigma_2)^2 + {\sigma_1}^2{\sigma_2}^2(R_{H,1} - R_{H,2})^2H^2}H \qquad \text{(A.1)}$$

With σ and R being the conductivities and Hall coefficients of the contributing carrier types - holes and electrons. Given the nearly isotropic, single band nature of the Fermi surface of Bi_2Se_3 , the following approximations can be applied to the model: $R_i = 1/\eta_i e$, $\mu_i = \sigma_i R_i$ with index i denoting electrons or holes, and

η and μ being the carrier concentrations and mobilities, respectively. Using these conversions, one arrives at an expression of the Drude model that depends directly on the carrier concentrations and mobilities of the two types of carriers:

$$\rho_{xy} = \frac{{\mu_h}^2 p - {\mu_e}^2 n - {\mu_h}^2 {\mu_e}^2 (p-n) H^2}{(p\mu_h + n\mu_e)^2 + {\mu_h}^2 {\mu_e}^2 (p-n)^2 H^2} \frac{H}{e} \tag{A.2}$$

with n and p being the electron and hole carrier concentrations and e being the electron charge. This gives a five dimensional parameter space for any curve fitting program to explore. Fitting each curve to the model directly produced insufficient and unreliable fits. Providing additional assumptions, such as fixing the concentration or mobility of one carrier type would help provide a more stable fit, however this introduces nontrivial assumptions about the system.

Another analytical method allows a further reduction of the parameter space. Equation 4.2 is of the general form $y = (ax + bx^3)/(c + dx^2)$ which can be re-expressed as a 3rd order polynomial. The polynomial can be solved by the linear algebra technique of singular value decomposition (SVD). The eigenvectors of the SVD are 4 component vectors; the components corresponding to values of a, b, c, and d. The eigenvector with the eigenvalue closest to zero contains the values of the coefficients that create the closest possible fit to the data that the Drude model can produce.

While this method provides accurate values of a, b, c, and d, it does not necessarily mean that the physical parameters of carrier concentrations mobilities are obtainable from the fit. However, in this case, conversions can be made between

the polynomial coefficients and n, p, μ_h and μ_e. These conversions are expressed by the following equations:

$$\mu_e = \frac{\sqrt{dS} - aS\sqrt{e} + \sqrt{(\sqrt{dS} - aS\sqrt{e})^2 + 4cS\sqrt{\frac{bSe}{d}}}}{2\sqrt{ct}} \tag{A.3a}$$

$$\mu_h = \frac{\sqrt{\frac{bSe}{d}}}{\mu_e} \tag{A.3b}$$

$$n = \frac{\sqrt{\frac{cS}{e}}\mu_e - \sqrt{\frac{dS}{e}}}{{\mu_e}^2 + \sqrt{\frac{b^2Se}{d}}} \tag{A.3c}$$

$$p = n + \frac{d}{be} \tag{A.3d}$$

It is important to note that the vector containing a, b, c, and d can be modified by a scalar without affecting the accuracy of the fit. Thus, it is not necessarily the individual values of a,b,c, and d but rather the relationships among the parameters that are accurate. This means that for the fits, there a scalar, S, that functions as the free parameter. Changing S, will change the resulting calculations of n, p, μ_e, and μ_h. Fig. A.1 shows how the physical parameters in both models change as S is changed

While the individual parameters n, p, μ_e, and μ_h can be modified by the scalar without changing the curve fit, the combination of of $\|p-n\|$ is, in fact, independent of the scalar S. Rearranging Eq. A.3d shows this. In other words, the difference in carrier concentrations can be pulled directly from the fit to the data, a result that can be quite useful by itself.

As can be seen in Fig. A.1, for most of the range of S, the carrier concen-

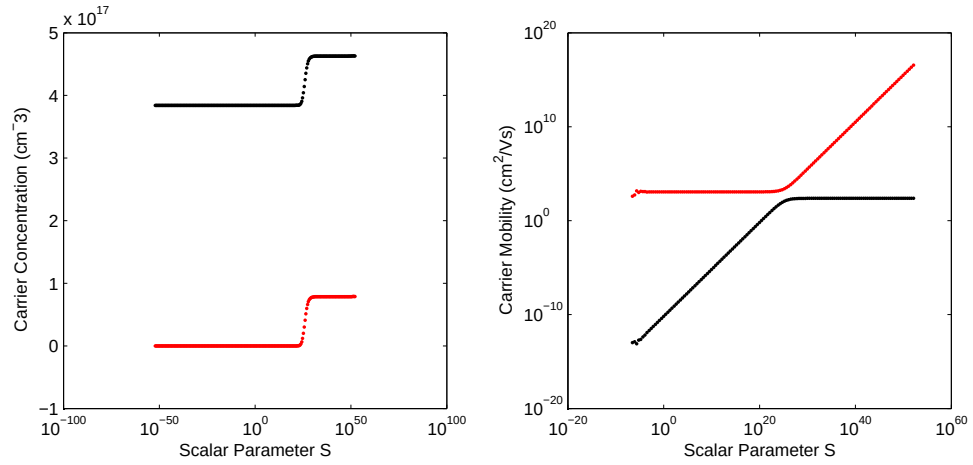

(a)

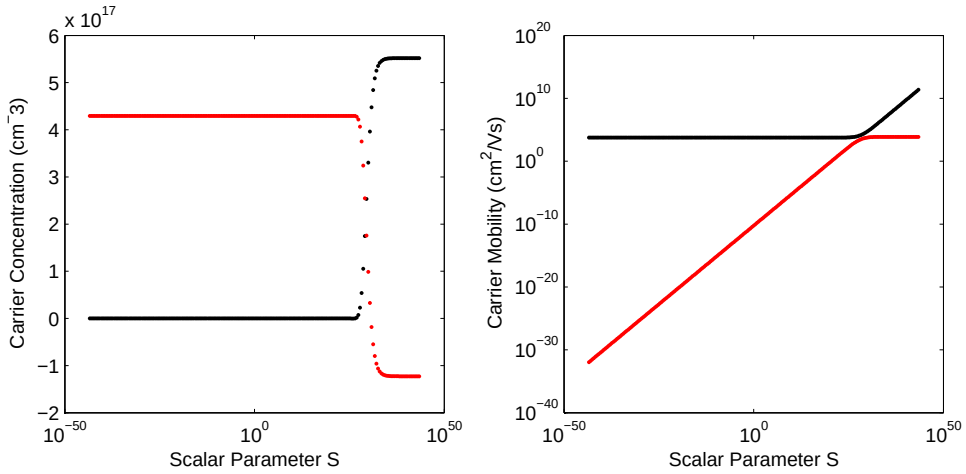

(b)

Figure A.1: Plots of carrier concentration (left) and mobility (right) vs the scalar S used in the SVD analysis of the Drude model. The top two plots show results from the model that assumes carriers of opposite sign and the bottom two plots assume carriers of the same sign. A scalar independent value is the difference (top) or sum (bottom) in carrier concentrations, therefore the two concentrations are coupled. The region of of interest in the parameter space of S is when the the lower n carrier type becomes large enough to significantly affect the dominant carrier type. The mobilities show a corresponding change in behavior at that range of S values as well.

trations are virtually unchanged. Within some range, however, the lower carrier concentration becomes large enough to affect the larger carrier concentration, since the sum or difference of the carrier concentrations is independent of S. It is within this same range, that the mobilities show a change in their S dependence. Below

the region of change, the mobility of the lesser conduction band remains unchanged, while the mobility of the dominant band decreases with decreasing S. Above the region of change, the mobilities switch their behavior. Therefore it is this region of change that is of interest for obtaining the four physical parameters from the Drude 2 carrier model.

The parameter space of S was explored and a region within these limits was found where all four parameters had reasonable values expected for Bi_2Se_3. In some cases, the results of fits to the $\Delta\rho_{xx}/\rho_0$ were used to choose a value of S. The same value of S was used when calculating physical parameters for all data on each sample, but the value of S was allowed to differ from sample to sample.

For analysis of samples where carriers of the same sign were assumed, Eq. A.2 was adjusted to reflect carriers of the same sign. The same procedure of SVD and subsequent conversion was successful for the adjusted model and the adjusted model was more accurate in fitting the data from samples D, V, and H than the original model had been for these samples. For the adjusted model, the scalar independent parameter was also changed to be the sum of carrier concentrations, instead of the difference.

A.2 Background Subtraction for QO

In analyzing QO, it is vital to correctly isolate the oscillatory component of the MR. All non-oscillatory MR is considered to be "background", for the purposes of QO analysis and correctly identifying and removing this background is a skill

in and of itself to be developed. Improper background subtractions can cause a smearing of the FFT, which could obscure peaks from actual oscillations. An improper background could also mimic oscillations, thereby removing them when the "background" is removed[1], or it could unknowingly introduce oscillations that are not actually there in the data. This section summarizes the general methods used in estimating the background MR for the purpose of isolating the QO measured in samples.

All samples showed a clear quadratic behavior below fields of 2 T that was very different from the higher field behavior, therefore MR background was only analyzed on data taken at fields $\geq$ 2 T in most cases. For this higher field portion, the data was interpolated to achieve regular intervals between data points. The number of interpolation points ranged up to 10 times the number of data points recorded, but was never fewer — except in the case of the data taken at pulsed field facilities Fewer interpolation points were needed in the Toulouse high field data, because each pulse produced nearly 20,000 data points, which is far more than needed for analysis and becomes taxing on the data analysis programs used. Furthermore, the raw data taken in Toulouse was of the oscillating signal measured directly, and the sets of data are averages over multiple periods and therefore inherently interpolated in the first place.

Next, the first derivative (w.r.t. magnetic field) was taken, to obtain a clearer picture of the oscillatory component. This is because of the large linear component in most samples measured, which becomes a constant value in the first derivative

[1] A case of throwing the baby out with the bathwater, as a folksy southerner might say.

and can then easily be distinguished from an oscillatory component, which remains unchanged (aside from a phase shift). Similarly, a squared MR becomes linear in the 1st derivative, also making it easier to separate from an oscillatory component. The resulting first derivative was then smoothed, using an adjacent average algorithm, with a smoothing window of $\leq 2\%$ of the total number of interpolated points in most cases. The smoothed curve was then fit to a polynomial, over the field range where the oscillations were most apparent. The oscillations being isolated often had a small number of extrema, and therefore polynomials of only the fourth degree or lower were used at this step. Usually a squared or cubic function was used. Then the resulting background subtracted first derivative was re-integrated. After this, any remaining obvious background was fit again to a low degree polynomial. Sometimes this was done in an "inverse-field basis"[2] and sometimes in a regular basis, whichever produced a better fit to the background while preserving the apparent oscillations.

To make absolutely sure that the background was accurate, the resulting oscillatory component was then subtracted from the first set of interpolated data (interpolated directly from the raw data). This resulting "background" was then checked for remnants of oscillations. If none were found, then the background was fit with a high order polynomial (to most closely follow the behavior of the background). It is the resulting polynomial fit that was used as a background subtraction from first set of interpolated data.

This background subtraction process was refined over many iterations and

[2]The term basis refers to the x-axis of the resulting graph of the data. By inverse-field basis, it is meant that the data was graphed vs inverse field and re-interpolated, to give an even distribution of points in inverse field, before having a background fit done.

provides, in the opinion of the author, the best overall method for elminating the non-oscillatory component of MR, for a wide range of oscillation frequencies, all the way below 10 T.

Chapter B: Measurements on SmB_6

As mentioned in section 1.1.3, there has been considerable effort devoted to finding new materials with distinct topologies that have Dirac states at their surfaces. Recent theoretical work has proposed that the intermediate valence compound SmB_6 may be a member of a newly classified family of strong topological insulators [71, 72, 134]. Called topological Kondo insulators, these systems differ from the conventional family of TIs [10, 135] like Bi_2Se_3 because the bulk insulating band gap arises due to electronic correlations and opens at the Fermi energy. These materials are extremely interesting because of the potential for interplay between the topological states and other correlated electronic states, as well as the possibility to aleviate issues with chemical potential shifts due to intrinsic bulk doping [41, 114].

This appendix presents resistance measurements probing the nature of surface conduction in bulk SmB_6samples, using variations of bulk crystal geometry and surface ionic liquid gating techniques to, respectively, tune the bulk and surface conductance contributions. In both cases, $R(T)$ is well described by a low-temperature, temperature-independent surface contribution in parallel with a thermally activated bulk contribution, with a crossover temperature that depends on the relative values of each conductance component. Gate-tuned measurements using a Corbino con-

tact geometry were conducted by collaborator Dr. Dohun Kim and indicate a very large surface carrier density that can be dramatically changed by application of bias voltage. Our results strongly support the model of an insulating bulk with metallic surface states, as previously probed by other techniques [73–75], and characterize the tunability, mobility and carrier density of surface charge carriers, in good agreement with other spectroscopic techniques. Our study not only confirms the ability to tune the relative surface and bulk conductance contributions, but also paves the way for unique gate-controlled device construction on single-crystal samples of SmB_6.

SmB_6, one of the first known Kondo insulator materials, has been of interest for many decades due to a long debate about the nature of its insulating state [68, 136]. It is now well known to harbor a *d-f* hybridization gap that opens at low temperatures and has been well characterized by several experimental techniques to lie in the range of ∼10–20 meV [69, 70, 73, 77, 78, 82, 137–141]. The electrical resistance $R(T)$ of SmB_6 exhibits a thermally activated behavior at intermediate temperatures below room temperature, before saturating at an approximately temperature-independent value below a few degrees Kelvin [73–75, 136, 138, 142–146]. This robust property has recently been considered a key signature of topologically protected surface states [72, 74], prompting many experimental efforts designed to probe the nature of the conducting states in this material [73, 77–84, 140]. Most recently, strong evidence confirming the topologically protected nature of these states has been mounting [83, 85, 147].

Single crystals were grown using polycrystalline SmB_6as the reactant and Al as the flux in a ratio of 1:200. Starting materials were placed in an alumina crucible

and sealed in a quartz ampoule under partial Ar pressure. Ampoules were heated to 1250°C and maintained at that temperature for 120 hours, then cooled at -2°C/hr to 900°C, followed by faster cooling. Crystals were etched out of the flux using HCl, yielding mostly cubic-shaped crystals ranging in size from $\sim (0.2)^3$ mm^3 to $\sim (1.2)^3$ mm^3. Single-crystal x-ray diffraction at 200 K using a Bruker APEX-II CCD system with a graphite monochromator and a MoKα source yields excellent refinement of crystallographic parameters, with lattice constants 4.13308(8) Å for the Pm-3m cubic structure and goodness of fit convergence at $R_1 = 0.62\%$. All samples were sanded and polished prior to contact placement. Sample thickness was controlled by means of sanding and measured using an optical microscope, with uncertainties dominated by magnification resolution. Thickness-dependent electrical resistivity measurements were performed using the standard AC technique, with four-wire geometry gold contact wires attached with silver conducting paint. Gating experiments were performed using a four-wire Corbino contact geometry pattern metalized with Au (200nm)/Ti (10nm) using thermal evaporation. After mounting on an insulating substrate, samples were covered with ionic liquid N,N-diethyl-N-methyl-N-(2-methoxyethyl)ammonium bis(trifluoromethylsulphonyl)imide (DEME-TFSI, Kanto Corporation) and an adjacent Au pad was used as a gate electrode. Ionic liquid application was performed inside a glove box and the sample was then transferred to the measurement cryostat within 5 minutes to minimize electrochemical reaction of DEME-TFSI with the ambient atmosphere. After each temperature sweep, gate voltage modulation was done by warming the sample to 230 K in-situ and changing gate voltage.

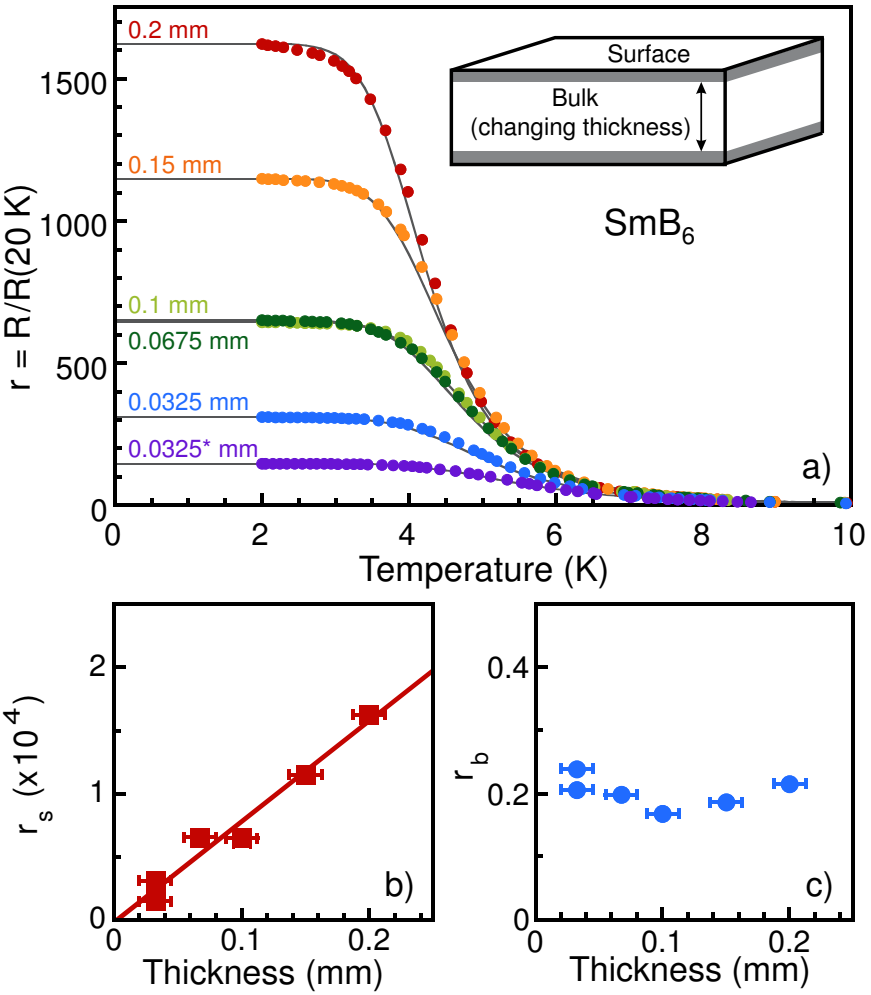

Figure B.1: a) Electrical resistance of a single crystal of SmB_6 as a function of sample thickness, normalized to its value at 20 K. The solid lines represent fits to the data using a two-channel conductance model [Eq. (1)], with fit parameters including the surface (panel b) and bulk (panel c) resistance ratio components $r_s \equiv R_s/R(20\text{ K})$ and $r_b \equiv R_b/R(20\text{ K})$, respectively, of the total conductance. [(*) Note geometry of sample for each 0.0325 mm thickness data set is slightly different due to loss of sample fraction.]

Fig. B.1a) presents the temperature dependence of the longitudinal resistance of a single crystal as a function of thickness variation, with measurements taken subsequent to each thickness adjustment. To eliminate uncertainty in the geometric factor arising from varying contact geometry, we plot the resistance ratio $r \equiv R/R(20\text{ K})$, or $R(T)$ normalized to the resistance value at 20 K (approximately the temperature at which the Kondo gap is fully open). The resistance curves exhibit similar qualitative behavior to each other and to those reported in the literature [75, 137, 142, 148] over the entire temperature range up to 300 K, with 2 K resistivity values ranging between 0.5–2.9 Ωcm.

The crossover from high-temperature, thermally activated behavior to a low-temperature plateau in $R(T)$ has been interpreted as a transition from bulk state-dominated conduction to surface state-dominated conduction [74, 75, 148]. This picture is consistent with the thickness dependence of resistance presented in Fig. B.1a), which exhibits a clear separation of $r(T)$ curves from a single trace at higher temperatures to distinct plateau values for each thickness at low temperatures. In other words, the relative bulk-to-surface ratio of conductance shrinks with decreasing thickness, as expected due to the reduction of overall bulk conductance.

A simple parallel conductance model is used to extract the relative contributions, with total conductance described by $G = G_s + G_b$, where $G_s = 1/R_s$ is the surface contribution (assumed temperature-independent) and $G_b = 1/R_b$ is the bulk contribution, assumed to be activated in temperature due to a bulk energy gap Δ. Therefore $G_b = W \cdot t/(\rho_b L) e^{-\Delta/k_B T}$ with sample length L, width W, and thickness t; bulk resistivity ρ_b in the high-temperature limit; and Boltzmann constant k_B. Thus,

for the dimensionless and geometry-independent [1] resistance ratio,

$$r(T)^{-1} = r_s^{-1} + [r_b e^{-\Delta/k_B T}]^{-1}, \tag{B.1}$$

where $r_s \equiv R_s/R(20\text{ K})$ and $r_b \equiv R_b/R(20\text{ K})$ are the dimensionless, normalized surface and bulk resistance ratios, respectively.

Fits to this model using r_s, r_b and Δ as free parameters are shown as solid lines in Fig. B.1a). For all thicknesses, we obtain a thickness-independent energy gap of $\Delta = 3.3 \pm 0.2$ meV, consistent with other transport measurements [75, 136, 138, 142, 145]. The values of r_s and r_b are presented in Figs. B.1b) and c), respectively, showing a clear contrast in their relationship with thickness; r_s exhibits a clear linear trend with thickness, while r_b is independent of thickness. Understood in the context of their normalized nature, the linear relation of $r_s(t)$ translates to a linearly decreasing relative contribution of surface conductance compared to bulk conductance with increasing sample thickness. Conversely, the extrapolated value of $r_s(0) = 0 \pm 0.00001$ at the zero-thickness limit translates to zero electrical conductance through the bulk, as expected in the bulk-surface model at low temperatures.

Previous experiments with electrochemical gating of Bi_2Se_3 thin films have shown great success in shifting the Fermi energy from well within the bulk conducting band into the bulk gap, allowing the isolated Dirac surface states to be probed directly [30, 149, 150]. Gating is, however, usually only effective at shifting the chemical potential of thin films or two dimensional systems, not bulk materials,

[1] We neglect a small dependence of surface conductance on changing surface area due to reduction in cross section perimeter.

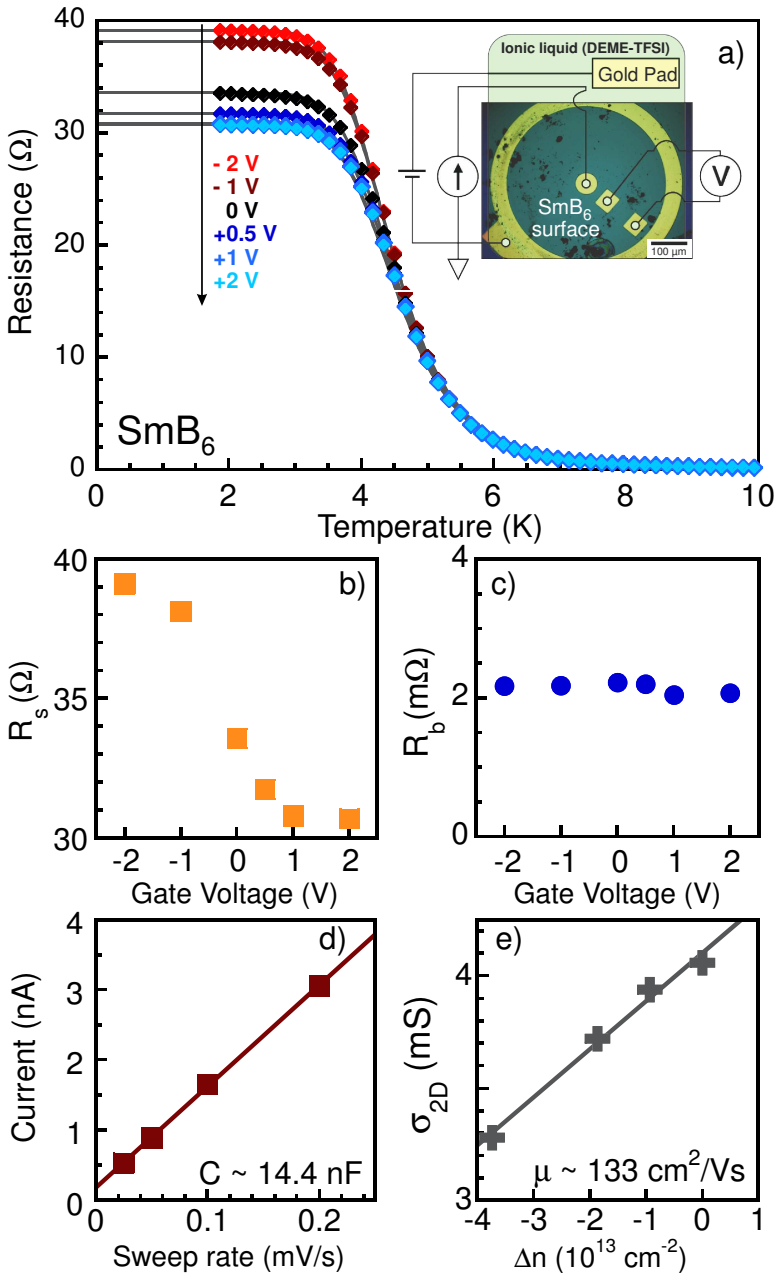

Figure B.2: a) Electrical resistance of SmB_6 sample as a function of ionic liquid gate voltage, measured with a Corbino disk lead geometry placed on the surface of a single crystal, as shown in the inset diagram (superimposed on sample photo, with green shaded area representing the area covered by the ionic liquid gate structure). Solid lines are fits to the two-channel conductance model [Eq. (2)]. Panels b) and c) present the surface and bulk resistance contributions, respectively, extracted from the two-channel fits as a function of gate voltage. Panel d) plots the transient current between the gate pad and ground as a function of gate voltage sweep rate, measured at 230 K. The solid line is a fit to a charging capacitor model with a capacitance of 14.4 nF. Panel e) shows the two-dimensional sheet conductivity as a function of the change in carrier concentration induced by gating. The solid line is a fit to a constant-mobility model with a mobility $\mu = 133$ cm^{2}V^{-1}s^{-1}.

as the gate electric field is confined to a thin region near the surface and heavily screened by bulk charge carriers. In the case of SmB_6, applying a gate voltage to the surface of a bulk crystal is a simple, yet clear test of the surface versus bulk contribution of charge carriers. If the transport is dominated by surface conduction [2], the Corbino geometry ensures that the electronic transport occurs only on the surface of a single side of the sample.

For the IL gating measurements, a four-probe Corbino geometry (see inset of Fig. 2) was patterned using e-beam lithography on a polished surface of SmB_6. Fig. B.2a) presents the $R(T)$ data for a single corbino device with various values of applied gate voltage V_g. Similar to the case of thickness variation (c.f. Fig. B.1), the variation of V_g has no effect on $R(T)$ at higher temperatures, as exhibited by the collapse of all data onto a single trace above ~ 5 K. However, at lower temperatures a clear voltage-dependent splitting of $R(T)$ occurs, suggesting an identical tuning of bulk-to-surface contributions to the measured conductance, now controlled by a gate-controlled shift of the surface state chemical potential.

The same two-conductivity model can be applied, with the exception that resistance ratios are no longer needed since no geometries are varying. We therefore fit $R(T)$ to the following form:

$$R(T)^{-1} = {R_s}^{-1} + [R_b e^{-\Delta/k_B T}]^{-1} \tag{B.2}$$

where R_s is the (constant) surface resistance and R_b the bulk resistance in the high

[2]The experiment is designed to show the difference between a quasi-two-dimensional (surface) state vs a fully bulk state, but cannot place an estimate on the exact thickness of the surface state.

temperature limit, and Δ is the gap energy as before.

Similar to the thickness case, we obtain a voltage-independent value of $\Delta = 3.78 \pm 0.01$ meV. Presented in Figs. B.2b) and c) are the results for R_s and R_b, respectively, as a function of V_g, showing that the variation of V_g has a dramatic effect on the surface resistance R_s, modulating it by over 25% through the accessible voltage range, while the bulk resistance R_b remains unaffected and relatively constant. The large change in saturation resistance with IL gating (Fig. B.2b) but negligible change in bulk resistivity (Fig. B.2c) confirms that the additional carriers injected by IL gating are confined to a region very near the surface. This tuning directly confirms the surface-born origin of low-temperature charge carriers in $SmB_6$and demonstrates the unique ability of controlling surface state conduction via device construction on the surface of a bulk cystal. In contrast, bulk doping [151, 152] is known to suppress the hybridization gap, thus reducing the bulk resistivity, whereas we see no change in our analysis of the bulk resisistivity with IL gate tuning. We can also rule out that the IL gating effect is due to changes in bulk doping in a layer near the surface, which would manifest as a change in activation energy and R_b, not seen in our experiment.

The Corbino gating experiment also provides information on the sign of charge carriers, their areal density and their mobility. As shown in Fig. B.2a), the variation of R_s with V_g is a decreasing function, consistent with the presence of dominant electron-like charge carriers at the surface. This may seem to be at odds with some measurements [74, 153] and consistent with others [75, 77, 79, 82, 136, 154], but it should be noted that traditional Hall effect experiments are no longer trivial

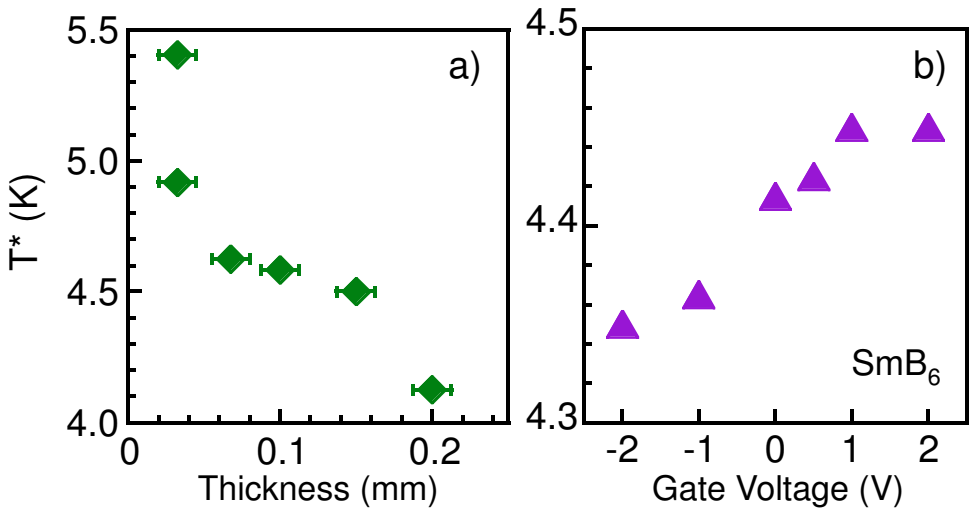

Figure B.3: a) Evolution of the crossover temperature T^* between bulk- and surface-dominated conductance, defined as the inflection point in resistance temperature dependence as a fuctino of (a) crystal thickness variation and (b) ionic liquid gate voltage tuning. The non-constant evolution of T^* is consistent with the two-channel conduction model (see text), showing the crossover depends solely on the relative bulk and surface contributions to the total electrical conduction.

in a situation with surface dominated transport, where conduction may be non-uniform. Recent angle-resolved photoemission measurements on SmB_6have observed two large and one small electron-like surface state bands, centered at the Γ and X points, respectively, in addition to the expected hole-like bulk bands [75, 77, 79, 82], suggesting a large difference in mobilities of each carrier type may be consistent with our observations.

Using a simple capacitor model to fit the transient gate current dependence on V_g sweep rate (Fig. B.2d)), allows the determination of the gate capacitance (14 nF), or specific capacitance $c_g = 3\ \mu\mathrm{F/cm}^2$, and hence the change in surface carrier density $\Delta n = c_g V_g/e$, where e is the elementary charge. The measured sheet conductivity σ_{2D} is approximately linear in the gate-induced change in Δn, as shown in Fig. B.2e), indicating a constant field-effect and a surface carrier mobility of 133 $\mathrm{cm}^2\mathrm{V}^{-1}\mathrm{s}^{-1}$ (based on the measured resistance and the distance between voltage probe contacts – see Fig. B.2 inset). Extrapolation of the linear relationship to $\sigma_{2D} = 0$ provides an estimate of $n \approx 2\times10^{14}$ cm^{-2} for the total carrier concentration. Using the unit cell area of (4.13 Å)^2 this is amounts to roughly one third of an electron per unit cell of the surface, which indicates the unlikelihood that the surface state arises due to impurities on the surface.

While the uncertainty of $\sim$ 30% for μ and n is large due to difficulties in estimating sample area and geometric factor for the Corbino geometry, the absolute carrier density is in excellent agreement with recent photoemission results [3]. The

[3]Recent angle-resolved photoemission experiments generally observe a small "α" band with Fermi surface area $0.020(2\pi/a)^2$ and two large "β" bands each with area $0.134(2\pi/a)^2$ [77, 79, 82]. With a unit cell of (4.13 Å)^2 and assuming each β band is electron-like and singly degenerate, this yields a total electron density of $\sim 1.7\times10^{14}$ cm^{-2}, which is very close to our estimate.

relatively low surface state mobility then appears to be a natural consequence of the very low Fermi velocity for the surface states.

Finally, in both thickness and gating variation experiments above, the crossover from bulk- to surface-dominated conductance with decreasing temperature is observed to change as a function of the control parameter, as expected due to the change in relative weighting of each contribution. Fig. B.3a) and b) present variation in this crossover temperature T^*, defined as the point of inflection of $R(T)$. The variation of T^* with that of both bulk (thickness) and surface (gating) contributions to conductance confirms the two-channel model and disproves the prevailing idea that there is a static transition temperature; rather, it is merely defined by the relative contributions from the two conduction channels.

In conclusion, we have demonstrated methods to tune both the bulk and surface contributions to the electrical conduction, thereby providing conclusive evidence for surface-dominated transport in SmB_6at low temperature. The evolution of transport with both sample thickness and surface gate tuning fits well to a two-channel conduction model involving a bulk, activated channel and a surface metallic channel. Furthermore, the measurement of gated surface conducting states using a Corbino lead geometry allows for the direct determination the electron-like sign of the surface charge carriers as well as the charge carrier density ($\sim 2 \times 10^{14}$ cm^{-2}) and mobility (~ 133 cm^{2}V^{-1}s^{-1}). The charge carrier sign and density are in good agreement with previous photoemission results for SmB_6. This study adds valuable information to our understanding of the proposed topological surface conduction in SmB_6 and provides promising use of gate-tuned devices structured on bulk crystal

samples for both fundamental and applied studies of these unique states.

Bibliography

[1] N. W. Ashcroft and N. D. Mermin, *Solid State Physics*. Thomson Learning Inc., 1976.

[2] P. C. I. GbR, "Pearson's online crystal structure dadabase," 2014.

[3] M. Tinkham, *Introduction to Superconductivity*. Dover Publications, 2nd ed., 1996.

[4] E. Bauer, G. Hilscher, H. Michor, C. Paul, E. W. Scheidt, A. Gribanov, Y. Seropegin, H. Noël, M. Sigrist, and P. Rogl, "Heavy fermion superconductivity and magnetic order in noncentrosymmetric cept$_3$Si," *Phys. Rev. Lett.*, vol. 92, p. 027003, Jan 2004.

[5] X.-L. Qi, "Topological insulators and superconductors," *Reviews of Modern Physics*, vol. 83, p. 1057, 2011.

[6] D. J. Thouless, M. Kohmoto, M. P. Nightingale, and M. den Nijs, "Quantized hall conductance in a two-dimensional periodic potential," *Phys. Rev. Lett.*, vol. 49, pp. 405–408, Aug 1982.

[7] J. E. Avron, R. Seiler, and B. Simon, "Homotopy and quantization in condensed matter physics," *Phys. Rev. Lett.*, vol. 51, pp. 51–53, Jul 1983.

[8] F. D. M. Haldane, "Model for a quantum hall effect without landau levels: Condensed-matter realization of the "parity anomaly"," *Phys. Rev. Lett.*, vol. 61, pp. 2015–2018, Oct 1988.

[9] M. Kohmmoto, "Topological invariant and the quantization of the hall conductance," *Annals of Physics*, vol. 160, pp. 343–354, 1985.

[10] C. L. Kane and E. J. Mele, "Z_2," *Phys. Rev. Lett.*, vol. 95, p. 146802, Sep 2005.

[11] C. L. Kane and E. J. Mele, "Quantum spin hall effect in graphene," *Phys. Rev. Lett.*, vol. 95, p. 226801, Nov 2005.

[12] L. Fu and C. L. Kane, "Topological insulators with inversion symmetry," *Phys. Rev. B*, vol. 76, p. 045302, Jul 2007.

[13] A. P. Schnyder, S. Ryu, A. Furusaki, and A. W. W. Ludwig, "Classification of topological insulators and superconductors in three spatial dimensions," *Phys. Rev. B*, vol. 78, p. 195125, Nov 2008.

[14] M. Z. Hasan and C. L. Kane, "Topological insulators," *Reviews of Modern Physics*, vol. 82, p. 3045, 2010.

[15] M. Wittenberg, "How to set up a band structure calculation," 1999.

[16] B. A. Bernevig, T. L. Hughes, and S.-C. Zhang, "Quantum spin hall effect and topological phase transition in hgte quantum wells," *Science*, vol. 314, no. 5806, pp. 1757–1761, 2006.

[17] L. Fu and C. L. Kane, "Superconducting proximity effect and majorana fermions at the surface of a topological insulator," *Physical Review Letters*, vol. 100, p. 096407, 2008.

[18] C. Nayak, S. H. Simon, A. Stern, M. Freedman, and S. Das Sarma, "Non-abelian anyons and topological quantum computation," *Rev. Mod. Phys.*, vol. 80, pp. 1083–1159, Sep 2008.

[19] D. Hsieh, D. Qian, L. Wray, Y. Xia, Y. Hor, R. Cava, and M. Hasan, "A topological dirac insulator in a quantum spin hall phase," *Nature*, vol. 452, p. 970, 2008.

[20] J. Moore, "Topological insulators: The next generation," *Nature Physics*, vol. 5, pp. 378–380, 2009.

[21] H. Zhang, C. X. Liu, X. L. Qi, X. Dai, Z. Fang, and S. C. Zhang, "Topological insulators in bi_2se_3, bi_2te_3, and sb_2te_3 with a single dirac cone on the surface," *Nature Physics*, vol. 5, p. 438, 2009.

[22] Y. Xia, D. Qian, D. Hsieh, L. Wray, A. Pal, H. Lin, A. Bansil, D. Grauer, Y. Hor, R. Cava, and M. Hasan, "Observation of a large-gap topological-insulator class with a single dirac cone on the surface," *Nature Physics*, vol. 5, pp. 398–402, 2009.

[23] Y. Chen, J. Analytis, J.-H. Chu, Z. Liu, S.-K. Mo, X. L. Qi, H. Zhang, D. Lu, X. Dai, Z. Fang, S. Zhang, I. Fisher, Z. Hussain, and Z.-X. Shen, "Experimental realization of a three-dimensional topological insulator bi_2te_3,," *Science*, vol. 325, p. 178, 2009.

[24] H. Khler and A. Fabricius, "Galvanomagnetic properties of bi_2se_3 with free carrier densities below 5×10^{17} cm^{-3}," *Physica Status Solidi B*, vol. 71, p. 487, 1975.

[25] S. Shigetomi, "Electrical properties of bi_2te_3," *Journal of the Physical Society of Japan*, vol. 11, pp. 915–919, 1956.

[26] Y. Kim, M. Brahlek, N. Bansal, E. Edrey, G. Kapilevich, K. Iida, M. Tanimura, Y. Horibe, S.-W. Cheong, and S. Oh, "Thickness-dependent bulk properties and weak antilocalization effect in topological insulator bi_2se_3," *Physical Review B*, vol. 84, p. 073109, 2011.

[27] J. Chen, H. Qin, F. Yang, J. Liu, T. Guan, F. Qu, G. Zhang, J. Shi, X. Xie, C. Yang, K. Wu, Y. Li, and L. Lu, "Gate-voltage control of chemical potential and weak antilocalization in bi_2se_3," *Physical Review Letters*, vol. 105, p. 176602, 2010.

[28] P. Cheng, C. Song, T. Zhang, Y. Zhang, Y. Wang, J.-F. Jia, J. Wang, Y. Wang, B.-F. Zhu, X. Chen, X. Ma, K. He, L. Wang, X. Dai, Z. Fang, X. Xie, X.-L. Qi, C.-X. Liu, S.-C. Zhang, and Q.-K. Xue, "Landau quantization of topological surface states in bi_2se_3," *Phys. Rev. Lett.*, vol. 105, p. 076801, Aug 2010.

[29] T. Hanaguri, K. Igarashi, M. Kawamura, H. Takagi, and T. Sasagawa, "Momentum-resolved landau-level spectroscopy of dirac surface state in bi_2se_3," *Phys. Rev. B*, vol. 82, p. 081305, Aug 2010.

[30] D. Kim, S. Cho, N. P. Butch, P. Syers, K. Kirshenbaum, S. Adam, J. Paglione, and M. S. Fuhrer, "Surface conduction of topological dirac electrons in bulk insulating bi_2se_3," *Nature Physics*, vol. 8, pp. 459–463, 2012.

[31] L. D. Alegria, M. D. Schroer, A. Chatterjee, G. R. Poirier, M. Pretko, S. K. Patel, and J. R. Petta, "Structural and electrical characterization of bi2se3 nanostructures grown by metalorganic chemical vapor deposition," *Nano Letters*, vol. 12, no. 9, pp. 4711–4714, 2012. PMID: 22827514.

[32] P. H. Le, K. H. Wu, C. W. Luo, and J. Leu, "Growth and characterization of topological insulator bi2se3 thin films on srtio3 using pulsed laser deposition," *Thin Solid Films*, vol. 534, no. 0, pp. 659 – 665, 2013.

[33] G. Zhang, H. Qin, J. Teng, J. Guo, Q. Guo, X. Dai, Z. Fang, and K. Wu, "Quintuple-layer epitaxy of thin films of topological insulator bi2se3," *Applied Physics Letters*, vol. 95, no. 5, pp. –, 2009.

[34] J. G. Checkelssky, Y. S. Hor, M.-H. Liu, D.-X. Qu, R. J. Cava, and N. P. Ong, "Quantum interference in macroscopic crystals of nonmetallic bi_2se_3," *Physical Review Letters*, vol. 103, p. 246601, 2009.

[35] Y. S. Hor, J. G. Checkelsky, D. Qu, N. P. Ong, and R. J. Cava, "Superconductivity and non-metallicity by doping the topological insulators bi_2se_3 and bi_2te_3," *Journal of Physics and Chemistry of Solids*, vol. 72, pp. 572–576, 2011.

[36] Y. L. Chen, J. H. Chu, J. G. Analytis, Z. K. Liu, K. igarashi, H. H. Duo, X. L. Qi, S. K. Mo, R. G. Moore, D. H. Lu, M. Hashimoto, T. Sasagawa, S. C. Zhang, I. R. Fisher, Z. Hussain, and Z. X. Shen, "Massive dirac fermion on the surface of a magnetically doped topological insulator," *Science*, vol. 329, p. 659, 2010.

[37] Y. S. Hor, A. Richardella, P. Roushan, Y. Xia, J. G. Checkelsky, A. Yazdani, M. Z. Hasan, N. P. Ong, and R. J. Cava, "P-type bi_2se_3 for topological insulator and low-temperature thermoelectric applications," *Physical Review B*, vol. 79, p. 195208, 2009.

[38] D. Hsieh, Y. Xia, D. Qian, L. Wray, J. Dil, F. Meier, J. Osterwalder, L. Patthey, J. Checkelsky, N. Ong, A. Fedorov, H. Lin, A. Bansil, D. Grauer, Y. Hor, R. Cava, and M. Hasan, "A tunable topological insulator in the spin helical dirac transport regime," *Nature*, vol. 460, p. 1101, 2009.

[39] T.-C. Hsiung, D.-Y. Chen, L. Zhao, Y.-H. Lin, C.-Y. Mou, T.-K. Lee, M.-K. Wu, and Y.-Y. Chen, "Enhanced surface mobility and quantum oscillations in topological insulator $bi_{1.5}sb_{0.5}te_{1.7}se_{1.3}$," *Applied Physics Letters*, vol. 103, p. 163111, 2013.

[40] J. Analytis, R. McDonald, S. Riggs, J.-H. Chu, G. Boebinger, and I. Fisher, "Two-dimensional dirac fermions in a topological insulator: transport in the quantum limit," *Nature Physics*, vol. 6, pp. 960–964, 2010.

[41] N. P. Butch, K. Kirshenbaum, P. Syers, A. B. Sushkov, G. S. Jenkins, H. D. Drew, and J. Paglione, "Search for topological surface conduction in ultrahigh mobility bi_2se_3 crystals," *Physical Review B*, vol. 81, p. 241301(R), 2010.

[42] A. Taskin, Z. Ren, S. Sasaki, K. Segawa, and Y. Ando, "Observation of dirac holes and electrons in a topological insulator," *Physical Review Letters*, vol. 107, p. 016801, 2011.

[43] Y. S. Hor, A. J. Williams, J. G. Checkelsky, P. Roushan, J. Seo, Q. Zu, H. W. Zandbergen, A. Yazdani, N. P. Ong, and R. J. Cava, "Superconductivity in $cu_xbi_2se_3$ and its implications for pairing in the undoped topological insulator," *Physical Review Letters*, vol. 104, p. 057001, 2010.

[44] M. Kriener, K. Segawa, Z. Ren, S. Sasaki, S. Wada, S. Kuwabata, and Y. Ando, "Electrochemical synthesis and superconducting phase diagram of $cu_xbi_2se_3$," *Phys. Rev. B*, vol. 84, p. 054513, Aug 2011.

[45] M. Kriener, K. Segawa, Z. Ren, S. Sasaki, and Y. Ando, "Bulk superconducting phase with a full energy gap in the doped topological insulator $cu_xbi_2se_3$," *Phys. Rev. Lett.*, vol. 106, p. 127004, Mar 2011.

[46] J. J. Hamlin, J. R. Jeffries, N. P. Butch, P. Syers, D. A. Zocco, S. T. Weir, Y. K. Vohra, J. Paglione, and M. B. Maple, "High pressure transport properties of the topological insulator bi_2se_3," *ArXiv e-prints*, Nov. 2011.

[47] K. Kirshenbaum, P. S. Syers, A. P. Hope, N. P. Butch, J. R. Jeffries, S. T. Weir, J. J. Hamlin, M. B. Maple, Y. K. Vohra, and J. Paglione, "Pressure-induced unconventional superconducting phase in the topological insulator bi_2se_3," *Phys. Rev. Lett.*, vol. 111, p. 087001, Aug 2013.

[48] M. Veldhorst, M. Snelder, M. Hoek, T. Gang, V. Guduru, X. Wang, U. Zeitler, W. van der Wiel, A. Golubov, H. Hilgenkamp, and A. Brinkman, "Josephson supercurrent through a topological insulator surface state," *Nature Materials*, vol. 11, pp. 417–421, 2012.

[49] H. M. Benia, C. Lin, K. Kern, and C. R. Ast, "Reactive chemical doping of the bi_2se_3 topological insulator," *Phys. Rev. Lett.*, vol. 107, p. 177602, Oct 2011.

[50] D. Kong, J. J. Cha, K. Lai, H. Peng, J. G. Analytis, S. Meister, Y. Chen, H.-J. Zhang, I. R. Fisher, Z.-X. Shen, and Y. Cui, "Rapid surface oxidation as a source of surface degradation factor for bi_2se_3," *ACS Nano*, vol. 5, pp. 4698–4703, 2011.

[51] H. Beidenkopf, P. Roushan, J. Seo, L. Gorman, I. Drozdov, Y. S. Hor, R. J. Cava, and A. Yazdani, "Spatial fluctuations of helical dirac fermions on the surface of topological insulators," *Nature Physics*, vol. 7, pp. 939–943, 2011.

[52] J. Duan, N. Tang, X. He, Y. Yan, S. Zhang, X. Qin, X. Wang, X. Yang, F. Xu, Y. Chen, W. Ge, and B. Shen, "Identification of helicity-dependent photocurrents from topological surface states in bi_2se_3 gated by ionic liquid," *Scientific Reports*, vol. 4, p. 4889, 2013.

[53] J. Suh, D. Fu, X. Liu, J. K. Furdyna, K. M. Yu, W. Walukiewicz, and J. Wu, "Fermi-level stabilization in the topological insulators bi_2se_3 and bi_2te_3: Origin of the surface electron gas," *Physical Review B*, vol. 89, p. 115307, 2014.

[54] C. E. ViolBarbosa, C. Shekhar, B. Yan, S. Ouardi, E. Ikenaga, G. H. Fecher, and C. Felser, "Direct observation of band bending in the topological insulator bi_2se_3," *Physical Review B*, vol. 88, p. 195128, 2013.

[55] M. Bianchi, D. Guan, S. Bao, J. Mi, B. Iversen, P. King, and P. Hofmann, "Coexistence of the topological state and a two-dimensional electron gas on the surface of bi_2se_3," *Nature Communications*, vol. 1, 2010.

[56] P. D. C. King, H. M. Bianchi, R. Ovsyannikov, C. Lupulescu, G. Landolt, B. Slomski, J. H. Dil, D. Guan, J. L. Mi, E. D. L. Rienks, J. Fink, A. Lindblad, S. Svensson, S. Bao, G. Balakrishnan, B. B. Iverson, J. Osterwalder, W. Eberhardt, F. Baumberger, and P. Hofmann, "Large tunable rashba spin splitting of a two-dimensional electron gas in bi_2se_3," *Physical Review Letters*, vol. 107, p. 096802, 2011.

[57] Z.-H. Zhu, G. Levy, B. Ludbrook, C. N. Veenstra, J. A. Rosen, R. Comin, D. Wong, P. Dosanjh, A. Ubaldini, P. Syers, N. P. Butch, J. Paglione, I. S. Elfimov, and A. Damascelli, "Rashba spin-splitting control at the surface of the topological insulator bi_2se_3," *Phys. Rev. Lett.*, vol. 107, p. 186405, Oct 2011.

[58] H. Murakawa, M. S. Bahramy, M. Tokunaga, Y. Kohama, C. Bell, Y. Kaneko, N. Nagaosa, H. Y. Hwang, and Y. Tokura, "Detection of berry's phase in a bulk rashba semiconductor," *Science*, vol. 342, pp. 1490–1493, 2013.

[59] M. R. Scholz, J. Sánchez-Barriga, D. Marchenko, A. Varykhalov, A. Volykhov, L. V. Yashina, and O. Rader, "Tolerance of topological surface states towards magnetic moments: Fe on bi_2se_3," *Phys. Rev. Lett.*, vol. 108, p. 256810, Jun 2012.

[60] T. Valla, Z.-H. Pan, D. Gardner, Y. S. Lee, and S. Chu, "Photoemission spectroscopy of magnetic and nonmagnetic impurities on the surface of the bi_2se_3 topological insulator," *Phys. Rev. Lett.*, vol. 108, p. 117601, Mar 2012.

[61] M. T. Edmonds, J. T. Hellerstedt, A. Tadich, A. Schenk, K. M. ODonnell, J. Tosado, N. P. Butch, P. Syers, J. Paglione, and M. S. Fuhrer, "Stability and surface reconstruction of topological insulator bi2se3 on exposure to atmosphere," *The Journal of Physical Chemistry C*, vol. 118, no. 35, pp. 20413–20419, 2014.

[62] M. T. Edmonds, J. T. Hellerstedt, A. Tadich, A. Schenk, K. M. O'donnell, J. Tosado, N. P. Butch, P. Syers, J. Paglione, and M. S. Fuhrer, "Air-stable electron depletion of bi_2se_3 using molybdenum trioxide into the topological regime," *ACS Nano*, vol. 8, pp. 6400–6406, 2014.

[63] H. Lin, L. Wray, Y. Xia, S. Xu, S. Jia, R. Cava, A. Bansil, and M. Hasan, "Half-heusler ternary compounds as new multifunctional experimental platforms for topological quantum phenomena," *Nature Materials*, vol. 9, p. 546, 2010.

[64] S. Chadov, X. Qi, J. Kbler, G. H. Fecher, C. Felser, and S. C. Zhang, "Tunable multifunctional topological insulators in ternary heusler compounds," *Nature Materials*, vol. 9, pp. 541–545, 2010.

[65] W. Feng, D. Xiao, Y. Zhang, and Y. Yao, "Half-heusler topological insulators: A first-principles study with the tran-blaha modified becke-johnson density functional," *Phys. Rev. B*, vol. 82, p. 235121, Dec 2010.

[66] C. Liu, Y. Lee, T. Kondo, E. D. Mun, M. Caudle, B. N. Harmon, S. L. Bud'ko, P. C. Canfield, and A. Kaminski, "Metallic surface electronic state in half-heusler compounds $r$ptbi (r= lu, dy, gd)," *Phys. Rev. B*, vol. 83, p. 205133, May 2011.

[67] N. P. Butch, P. Syers, K. Kirshenbaum, A. P. Hope, and J. Paglione, "Superconductivity in the topological semimetal yptbi," *Phys. Rev. B*, vol. 84, p. 220504, Dec 2011.

[68] J. W. Allen, R. M. Martin, B. Batlogg, and P. Wachter, "Mixed valent smb6 and gold?sms: Metals or insulators?," *J. Appl. Phys.*, vol. 49, no. 3, pp. 2078–2083, 1978.

[69] B. Gorshunov, N. Sluchanko, A. Volkov, M. Dressel, G. Knebel, A. Loidl, and S. Kunii, "Low-energy electrodynamics of smb_6," *Phys. Rev. B*, vol. 59, p. 1808, 1999.

[70] K. Flachbart, K. Gloos, E. Konovalova, Y. Paderno, M. Reiffers, P. Samuely, and P. Švec, "Energy gap of intermediate-valent smb_6 studied by point-contact spectroscopy," *Phys. Rev. B*, vol. 64, p. 085104, Aug 2001.

[71] M. Dzero, K. Sun, P. Coleman, and V. Galitski, "Theory of topological kondo insulators," *Phys. Rev. B*, vol. 85, p. 045130, 2012.

[72] M. Dzero, K. Sun, V. Galitski, and P. Coleman, "Topological kondo insulators," *Physical Review Letters*, vol. 104, p. 106408, 2010.

[73] X. Zhang, N. P. Butch, P. Syers, S. Ziemak, R. L. Greene, and J. Paglione, "Hybridization, inter-ion correlation, and surface states in the kondo insulator smb_6," *Phys. Rev. X*, vol. 3, p. 011011, 2013.

[74] D. J. Kim, S. Thomas, T. Grant, J. Botimer, Z. Fisk, and J. Xia, "Surface hall effect and nonlocal transport in smb_6: Evidence for surface conduction," *Scientific Reports*, vol. 3, p. 150, 2013.

[75] S. Wolgast, C. Kurdak, K. Sun, J. W. Allen, D. J. Kim, and Z. Fisk, "Low-temperature surface conduction in the kondo insulator smb_6," *Phys. Rev. B*, vol. 88, p. 180405, 2013.

[76] P. Syers, D. Kim, M. S. Fuhrer, and J. Paglione, "Tuning bulk and surface conduction in topological kondo insulator smb_6," 2014.

[77] M. Neupane, N. Alidoust, S. Y. Xu, T. Kondo, Y. Ishida, D. J. Kim, C. Liu, I. Belopolski, Y. J. Jo, T. R. Chang, H. T. Jeng, T. Durakiewicz, L. Balicas, H. Lin, A. Bansil, S. Shin, Z. Fisk, and M. Z. Hasan, "Suface electronic structure of the topological kondo-insulator candidate correlated electron systems smb_6," *Nature Comm.*, vol. 4, p. 2991, 2013.

[78] E. Frantzeskakis, N. de Jong, B. Zwartsenberg, Y. K. Huang, Y. Pan, X. Zhang, J. X. Zhang, F. X. Zhang, L. H. Bao, O. Tegus, A. Varykhalov, A. de Visser, and M. S. Golden, "Kondo hybridization and the origin of metallic states at the (001) surface of smb_6," *Phys. Rev. X*, vol. 3, p. 041024, 2013.

[79] J. Jiang, A. Li, T. Zhang, Z. Sun, F. Chen, Z. R. Ye, M. Xu, Q. Q. Ge, S. Y. Tan, X. H. Niu, M. Xia, B. P. Xie, Y. F. Li, X. H. Chen, H. H. Wen, and D. L. Feng, "Observation of possible topological in-gap suface states in the kondo insulator smb_6 by photoemission," *Nature Comm.*, vol. 4, p. 3010, 2013.

[80] Z. H. Zhu, A. Nicolau, G. Levy, N. P. Butch, P. Syers, X. F. Wang, J. Paglione, G. A. Sawartzky, I. S. Elfimov, and A. Damascelli, "Polarity-driven surface metallicity in smb_6," *Phys. Rev. Lett.*, vol. 111, p. 216402, 2013.

[81] J. D. Denlinger, J. W. Allen, J. S. Kang, and K. Sun, "Temperature dependence of linked gap and surface state evolution in the mixed valent topological insulator smb_6,"

[82] N. Xu, X. Shi, P. K. Biswas, C. E. Matt, R. S. Dhaka, Y. Huang, N. C. Plumb, M. Radović, J. H. Dil, E. Pomjakushina, K. Conder, A. Amato, Z. Salman, D. M. Paul, J. Mesot, H. Ding, and M. Shi, "Surface and bulk electronic structure of the strongly correlated system smb_6 and implications for a topological kondo insulator," *Phys. Rev. B*, vol. 88, p. 121102, Sep 2013.

[83] G. Li, Z. Xiang, F. Yu, T. Asaba, B. Lawson, P. Cai, C. Tinsman, A. Berkley, S. Wolgast, Y. S. Eo, D.-J. Kim, C. Kurdak, J. W. Allen, K. Sun, X. H. Chen, Y. Y. Wang, Z. Fisk, and L. Li, "Quantum oscillations in kondo insulator smb6,"

[84] S. Suga, K. Sakamoto, T. Okuda, K. Miyamoto, K. Kuroda, A. Sekiyama, J. Yamaguchi, H. Fujiwara, A. Irizawa, T. Ito, S. Kimura, T. Balashov, W. Wulfhekel, S. Yeo, F. Iga, and S. Imada, "Spin-polarized angle-resolved photoelectron spectroscopy of the so-predicted kondo topological insulator smb_6," *J. Phys. Soc. Japan*, vol. 83, p. 038001, 2014.

[85] Y. Nakajima, P. S. Syers, X. Wang, R. Wang, and J. Paglione, "One-dimensional edge state transport in a topological Kondo insulator," *ArXiv e-prints*, Dec. 2013.

[86] K. Schubert, K. Anderko, M. Kluge, H. Beeskow, M. Ilschner, and E. D

[87] P. P. Konorov, "Electrical properties of bismuth chalcogens 2: Electrical properties of bismuth selenide," *Soviet Physics - Technical Physics*, vol. 1, pp. 1365–1370, 1956.

[88] G. N. Gordiakova, G. V. Kokosh, and S. S. Sinani, "Investigation of thermoelectric properties of solid solutions bi_2te_3-bi_2se_3," *Soviet Physics - Technical Physics*, vol. 3, pp. 1–14, 1958.

[89] E. Mooser and W. B. Pearson, "The crystal structure and properties of the group vb to viib elements and of compounds formed between them," *Journal of Physics and Chemistry of Solids*, vol. 7, pp. 65–77, 1958.

[90] S. K. Mishra, S. Satpathy, and O. Jepsen, "Electronic structure and thermoelectric properties of bismuth telluride and busmuth selenide," *Journal of Physics: Condensed Matter*, vol. 9, pp. 461–470, 1997.

[91] J. Waters, D. Crouch, J. Raftery, and P. O'Brien, "Deposition of bismuth chalcogenide thin films using novel single-source precursors by metal-organic chemical vapor deposition," *CHEMISTRY OF MATERIALS*, vol. 16, pp. 3289–3298, AUG 24 2004.

[92] B. Sankapal, R. Mane, and C. Lokhande, "Preparation and characterization of Bi2Se3 thin films deposited by successive ionic layer adsorption and reaction (SILAR) method," *MATERIALS CHEMISTRY AND PHYSICS*, vol. 63, pp. 230–234, MAR 15 2000.

[93] D. Wang, D. Yu, M. Mo, X. Liu, and Y. Qian, "Preparation and characterization of wire-like sb2se3 and flake-like bi2se3 nanocrystals," *Journal of Crystal Growth*, vol. 253, no. 14, pp. 445 – 451, 2003.

[94] J. Wiese and L. Mulawer, "LATTICE CONSTANTS OF BI2TE3-BI2SE3 SOLID SOLUTION ALLOYS," *JOURNAL OF PHYSICS AND CHEMISTRY OF SOLIDS*, vol. 15, no. 1-2, pp. 13–16, 1960.

[95] J. HORAK, Z. STARY, P. LOSTAK, and J. PANCIR, "ANTI-SITE DEFECTS IN N-BI2SE3 CRYSTALS," *JOURNAL OF PHYSICS AND CHEMISTRY OF SOLIDS*, vol. 51, no. 12, pp. 1353–1360, 1990.

[96] A. International, "Alloy phase diagram database," 2014.

[97] H. Tang, D. Liang, R. Qiu, and X. Gao, "Two-dimensional transport-induced linear magneto-resistance in topological insulator bi_2se_3," *ACS Nano*, vol. 5, p. 7510, 2011.

[98] B. Assaf, T. Cardinal, P. Wei, J. Moodera, and D. Heiman, "Linear magnetoresistance in topological insulator thin films: Quantum phase coherence at high temperatures," *Applied Physics Letters*, vol. 102, p. 012102, 2013.

[99] G. J. Snyder, R. Hiskes, S. DiCarolis, M. R. Beasley, and T. H. Geballe, "Intrinsic electrical transport and magnetic properties of $la_{0.67}ca_{0.33}mno_3$ and $la_{0.67}sr_{0.33}mno_3$ mocvd thin films and bulk material," *Phys. Rev. B*, vol. 53, pp. 14434–14444, Jun 1996.

[100] P. L. Kapitza, "The study of the specific resistance of bismuth crystals and its change in strong magnetic fields and some allied problems," *Proceedings of the Royal Society A*, vol. 119, pp. 358–443, 1928.

[101] P. L. Kapitza, "The change of electrical conductivity in strong magnetic fields. part i. experimental results," *Proceedings of the Royal Society A*, vol. 123, pp. 292–372, 1929.

[102] J. Chu, S. Riggs, M. Shapiro, J. Liu, C. Serero, D. Yi, M. Melissa, S. Suresha, C. Frontera, A. Vishwanath, X. Marti, I. Fisher, and R. Ramesh, "Linear magnetoresistance and time reversal symmetry breaking of pyrochlore iridates $bi_2ir_2o_7$,"

[103] R. Xu, A. Husmann, T. Rosenbaum, M.-L. Saboungi, J. Enderby, and P. Littlewood, "Large magnetoresistance in non-magnetic silver chalcogenides," *Nature*, vol. 390, pp. 57–60, 1997.

[104] H. G. Johnson, S. P. Bennett, R. Barua, L. H. Lewis, and D. Heiman, "Universal properties of linear magnetoresistance in strongly disordered mnas-gaas composite semiconductors," *Physical Review B*, vol. 82, p. 085202, 2010.

[105] M. M. Parish and P. B. Littlewood, "Classical magnetotransport of inhomogeneous conductors," *Phys. Rev. B*, vol. 72, p. 094417, Sep 2005.

[106] M. M. Parish and P. B. Littlewood, "Non-saturating magnetoresistance in heavily disordered semiconductors," *Nature*, vol. 426, p. 162, 2003.

[107] N. Kozlova, N. Mori, O. Makarovsky, L. Eaves, Q. Zhuang, A. Krier, and A. Patane, "Linear magnetoresistance due to multiple-electron scattering by low-mobility islands in an inhomogeneous conductor," *Nature Communications*, vol. 3, p. 1097, 2012.

[108] A. A. Abrikosov, "Quantum linear magnetoresistance," *Europhysics Letters*, vol. 49, pp. 789–793, 2000.

[109] C. Wang and X. Lei, "Linear magnetoresistance on the topological surface," *Physical Review B*, vol. 86, p. 035442, 2012.

[110] K. S. Novosolev, A. K. Geim, S. V. Morozov, D. Jiang, M. I. Katsnelson, I. V. Grigorieva, S. V. Dubonos, and A. A. Firsov, "Two-dimensional gas of massless dirac fermions in graphene," *Nature*, vol. 438, pp. 197–200, 2005.

[111] A. A. Taskin and Y. Ando, "Berry phase of nonideal dirac fermions in topological insulators," *Phys. Rev. B*, vol. 84, p. 035301, Jul 2011.

[112] Y. Zhang, K. He, C.-Z. Chang, C.-L. Song, L.-L. Wang, X. Chen, J.-F. Jia, Z. Fang, X. Dai, W.-Y. Shan, S.-Q. Shen, Q. Niu, X.-L. Qi, S.-C. Zhang, X.-C. Ma, and Q.-K. Xue, "Crossover of the three-dimensional topological insulator bi_2se_3 to the two-dimensional limit," *Nature Physics*, vol. 6, pp. 584–588, 2010.

[113] Z. Ren, A. A. Taskin, S. Sasaki, K. Segawa, and Y. Ando, "Larg bulk resistivity and surface quantum oscillations in the topological insulator bi_2te_2se," *Physical Review B*, vol. 82, p. 241306(R), 2010.

[114] D.-X. Qu, Y. Hor, J. Xiong, R. Cava, and N. Ong, "Quantum oscillations and hall anomaly of surface states in the topological insulator bi_2te_3," *Science*, vol. 329, pp. 821–824, 2010.

[115] F. Zhang, C. L. Kane, and E. J. Mele, "Surface states of topological insulators," *Phys. Rev. B*, vol. 86, p. 081303, Aug 2012.

[116] D. Schoenberg, *Magnetic Oscillations in Metals*. Cambridge University Press, 1984.

[117] J. Analytis, J.-H. Chu, Y. Chen, F. Corredor, R. McDonald, Z. Shen, and I. Fisher, "Bulk fermi surface coexistence with dirac surface state in bi_2se_3," *Physical Review B*, vol. 81, p. 205407, 2010.

[118] B. Fauque, N. Butch, P. Syers, J. Paglione, S. Wiedmann, A. Collaudin, B. Grena, U. Zeitler, and K. Behnia, "Magnetothermoelectric properties of bi_2se_3," *Physical Review B*, vol. 87, p. 035133, 2013.

[119] M. Stordeur, K. K. Ketavong, A. Priemuth, H. Sobotta, and V. Riede, "Optical and electrical investigations of n-type bi_2se_3 single crystals," *Physica Status Solidi B*, vol. 169, p. 505, 1992.

[120] R. Aguilar, L. Wu, A. Stier, L. Bilbro, M. Brahlek, and N. A. N. Bansal, S. Oh, "Aging and reduced bulk conductance in thin films of the topological insulator bi_2se_3," *Journal of Applied Physics*, vol. 113, p. 153702, 2013.

[121] R. G. Chambers, "The two-band effect in conduction," *Proceedings of the Physical Society A*, vol. 65, pp. 903–910, 1952.

[122] H. D. Li, Z. Y. Wang, X. Kang, X. Guo, H. T. He, Z. Wang, J. N. Wang, T. L. Wong, N. Wang, and M. H. Xie, "The van der waals epitaxy of bi_2se_3 on the vicinal si(111) surface: an approach for preparing high-quality thin films of a topological insulator," *New Journal of Physics*, vol. 12, p. 103038, 2010.

[123] A. Richardella, D. M. Zhang, J. S. Lee, A. Koser, D. W. Rench, A. L. Yeats, B. B. Buckley, D. D. Awschalom, and N. Samarth, "Coherent heteroepitaxy of bi_2se_3 on gaas(111)b," *Applied Physics Letters*, vol. 97, p. 262104, 2010.

[124] C. Jozwiak, Y. L. Chen, A. V. Fedorov, J. G. Analytis, C. R. Rotundu, A. K. Schmid, J. D. Denlinger, Y.-D. Chuang, D.-H. Lee, I. R. Fisher, R. J. Birgenau, Z.-X. Shen, Z. Hussain, and A. Lanzara, "Widespread spin polarization effects in photoemission from topological insulators," *Physical Review B*, vol. 84, p. 165113, 2011.

[125] Z.-H. Zhu, C. Veenstra, G. Levy, A. Ubaldini, P. Syers, N. Butch, J. Paglione, M. Haverkort, I. Elfimov, and A. Damascelli, "Layer-by-layer entangled spin-orbital texture of the topological surface state in bi_2se_3," *Physical Review Letters*, vol. 110, p. 216401, 2013.

[126] Y. H. Wang, D. Hsieh, E. J. Sie, H. Steinberg, D. R. Gardner, Y. S. Lee, P. Jarillo-Herrero, and N. Gedik, "Measurement of intrinsic dirac fermion cooling on the surface of the topological insulator bi_2se_3 using time-resolved

and angle-resolved photoemission spectroscopy," *Phys. Rev. Lett.*, vol. 109, p. 127401, Sep 2012.

[127] L. A. Wray, S.-Y. Xu, Y. Xia, Y. S. Hor, D. Qian, A. V. Fedorov, H. Lin, A. Bansil, R. J. Cava, and M. Z. Hasan, "Observation of topological order in a superconducting doped topological insulator," *Nature Physics*, vol. 6, pp. 855–859, 2010.

[128] M. Bahramy, P. King, A. de la Torre, J. Chang, M. Shi, L. Patthey, G. Balakrishnan, P. Hofmann, R. Arita, and F. Baumberger, "Emergent quantum confinement at topological insulator surfaces," *Nature Communications*, vol. 3, p. 1159, 2012.

[129] M. Bianchi, R. Hatch, D. Guan, T. Planke, J. Mi, B. Iversen, and P. Hofmann, "The electronic structure of clean and adsorbate covered bi_2se_3: an angle-resolved photoemission study," *Semiconductor Science and Technology*, vol. 27, p. 124001, 2012.

[130] C. Mann, D. West, I. Miotkowski, Y. P. Chen, S. Zhang, and C.-K. Shih, "Mapping the 3d surface potential in bi_2se_3," *Nature Communications*, vol. 4, p. 2277, 2013.

[131] D. Kim, Q. Li, P. S. N. P. Butch, J. Paglione, S. Das-Sarma, and M. S. Fuhrer, "Intrinsic electron-phonon resistivity in bi_2se_3 in the topological regime," *Phys. Rev. Lett.*, vol. 109, p. 166801, 2012.

[132] H. Kwon, W. Ko, I. Jeon, H. W. Kim, Y. Oh, J. Ku, P. Syers, S.-J. Kahng, K. Park, J. Paglione, H. Suh, and S. W. Hwang, "Dirac gap opening of a ho-doped topological insulator," *pre-print*, 2014.

[133] G. Jenkins, A. Sushkov, D. Schmadel, N. Butch, P. Syers, J. Paglione, and H. Drew, "Terahertz kerr and reflectivity measurements on the topological insulator bi_2se_3," *Physical Review B*, vol. 82, p. 125120, 2010.

[134] V. Alexandrov, M. Dzero, and P. Coleman, "Cubic topological kondo insulators," *PHysical Review Letters*, vol. 111, p. 226403, 2013.

[135] L. Fu, C. L. Kane, and E. J. Mele, "Topological insulators in three dimensions," *Physical Review Letters*, vol. 98, p. 106803, 2007.

[136] J. W. Allen, B. Batlogg, and P. Wachter, "Large low-temperature hall effect and resistivity in mixed-valent smb_6," *Phys. Rev. B*, vol. 20, p. 4807, 1979.

[137] S. Gabani, K. Flachbart, V. Pavlik, M. Orendac, E. Konovalova, Y. Paderno, and J. Sebek, "Investigation of in-gap states in smb_6," *Czech. J. Phys.*, vol. 52, p. 279, 2002.

[138] N. E. Sluchanko, V. V. Glushkov, B. P. Gorshunov, S. V. Demishev, M. V. Kondrin, A. A. Pronin, A. A. Volkov, A. K. Savchenko, G. Grner, Y. Bruynseraede, V. V. Moshchalkov, and S. Kunii, "Intragap states in smb6," *Phys. Rev. B*, vol. 61, p. 9906, 2000.

[139] M. M. Yee, Y. He, A. Soumyanarayanan, D.-J. Kim, Z. Fisk, and J. E. Hoffman, "Imaging the Kondo Insulating Gap on SmB6," *ArXiv e-prints*, Aug. 2013.

[140] S. Rössler, T.-H. Jang, D.-J. Kim, L. H. Tjeng, Z. Fisk, F. Steglich, and S. Wirth, "Hybridization gap and fano resonance in smb_6," *Proc. Natl. Acad. Sci.*, vol. 111, p. 4798, 2014.

[141] W. Ruan, C. Ye, M. Guo, F. Chen, X. Chen, G.-M. Zhang, and Y. Wang, "Emergence of a coherent in-gap state in the smb_6 kondo insulator revealed by scanning tunneling spectroscopy," *Phys. Rev. Lett.*, vol. 112, p. 136401, Mar 2014.

[142] A. Menth, E. Buehler, , and T. H. Geballe, "Magnetic and semiconducting properties of smb6," *Physical Review Letters*, vol. 22, pp. 295–297, 1969.

[143] J. C. Nickerson, R. M. White, K. N. Lee, R. Bachmann, T. H. Geballe, and G. W. Hull, "Physical properties of smb_6," *Phys. Rev. B*, vol. 3, p. 2030, 1971.

[144] T. Caldwell, A. P. Reyes, W. G. Moulton, P. L. Kuhns, M. J. R. Hoch, P. Schlottmann, and Z. Fisk, "High field suppression of in-gap states in the kondo insulator smb_6," *Phys. Rev. B*, vol. 75, p. 075106, 2007.

[145] J. Beille, M. B. Maple, J. Wittig, Z. Fisk, and L. E. DeLong, "Suppression of the energy gap in smb_6 under pressure," *Phys. Rev. B*, vol. 28, pp. 7397–7400, Dec 1983.

[146] W. A. Phelan, S. M. Koohpayeh, P. Cottingham, J. W. Freeland, J. C. Leiner, C. L. Broholm, and T. M. McQueen, "Correlation between bulk thermodynamic measurements and the low-temperature-resistance plateau in smb_6," *Phys. Rev. X*, vol. 4, p. 031012, Jul 2014.

[147] N. Xu, P. K. Biswas, J. H. Dil, R. S. Dhaka, G. Landolt, S. Muff, C. E. Matt, X. Shi, N. C. Plumb, M. Radovi?, E. Pomjakushina, K. Conder, A. Amato, S. V. Borisenko, R. Yu, H.-M. Weng, Z. Fang, X. Dai, J. Mesot, H. Ding, and M. Shi, "Direct observation of the spin texture in smb6 as evidence of the topological kondo insulator," *Nature Comm.*, vol. 5, pp. –, 2014.

[148] A. Kebede, M. C. Aronson, C. M. Buford, P. C. Canfield, J. H. Cho, B. R. Coles, J. C. Cooley, J. Y. Coulter, Z. Fisk, G. D. Goettee, W. L. Hults, A. Lacerda, T. D. McLendon, P. Tiwari, and J. L. Smith, "Studies of the correlated electron system smb_6," *Physica B*, vol. 223, pp. 256–259, 1996.

[149] S. Cho, N. P. Butch, J. Paglione, and M. S. Fuhrer, "Insulating behavior in ultrathin bismuth selenide field effect transistors," *Nano Letters*, vol. 11, p. 1925, 2011.

[150] D. Kim, P. Syers, N. P. Butch, J. Paglione, and M. S. Fuhrer, "Coherent topological transport on the surface of bi2se3," *Nature Comm.*, vol. 4, no. 2040, pp. –, 2013.

[151] D. J. Kim, J. Xia, and Z. Fisk, "Topological surface state in the kondo insulator samarium hexaboride," *Nature Materials*, vol. 13, pp. 466–470, 2014.

[152] S. Yeo, K. Song, N. Hur, Z. Fisk, and P. Schlottmann, "Effects of eu doping on smb_6 single crystals," *Phys. Rev. B*, vol. 85, p. 115125, Mar 2012.

[153] N. E. Sluchanko, A. A. Volkov, V. V. Gluskov, B. P. Gorshunov, S. V. Demishev, M. V. Kondrin, A. A. Pronin, N. A. Samarin, Y. Bruynseraede, V. V. Moshchalkov, and S. Kunii, "Nature of the low-temperature anomalies in the physical properties of the intermediate-valent compound smb_6," *Journal of Experimental and Theoretical Physics*, vol. 88, pp. 533–537, 1999.

[154] J. C. Cooley, M. C. Aronson, Z. Fisk, and P. C. Canfield, "Smb_6: Kondo insulator or exotic metal?," *Phys. Rev. Lett.*, vol. 74, p. 1629, 1995.